Robust Vehicle State and Parameter Observation

Adaptive Filtering Concept with Enhanced Robustness by Usage of Markov
Chains

D I S S E R T A T I O N

zur Erlangung des akademischen Grades eines Doktors
der Ingenieurswissenschaften

vorgelegt von
Dipl.-Ing. Matthias Korte

eingereicht bei der Naturwissenschaftlich-Technischen Fakultät
der Universität Siegen
Siegen 2016

Gutachter:
1. Gutachter Universität Siegen: Prof. Dr. Hubert Roth
2. Gutachter Universität Erlangen: Prof. Dr. Roppenecker

Tag der mündlichen Prüfung: 06. Juni 2016

Acknowledgments

Abstract

The work presented here should fulfil the requirements for the granting of the degree of Doctor of Engineering at the University Siegen. It was completed within the EU funded project eFuture with the company Intedis. The goal of the project was to create an efficient and safe electric vehicle on the basis of a Tata eVista with help of a complete new architecture.

A novel robust vehicle observer was designed for an optimal support of the integrated driver assistance systems. The concept for the observer is based upon an extended Kalman Filter using a non-linear vehicle model and the Dugoff tire model.

Moreover, a parameter estimation and a plausibility check of the sensor signals were developed to increase the robustness of the observer. The estimation of the vehicle mass, the effective tire radii and the road adhesion were designed with an event-seeking characteristic in order to minimise the computational load. In the plausibility check delayed or faulty sensor signals are detected and corrected. Here the newly designed replacement of delayed or missing sensor signals by the concept of Markov Chains is pointed out. By this, the correctness of the output signals and the safety of the vehicle can be guaranteed for a defined time. Additionally, the evaluation of the stability limits and the driven distance of the vehicle are computed under the use of quantities that were calculated before. After the model based design the software was integrated on the hardware of the prototype. The functionality of this concept is given by results during dynamic test drives.

Zusammenfassung

Die hier vorgestellte Arbeit soll die Anforderungen zur Verleihung des Doktortitels an der Universität Siegen erfüllen. Sie wurde im Rahmen des EU geförderten Projekts eFuture bei der Firma Intedis in Würzburg abgeleistet, in welchem ein sicheres und effizientes Elektrofahrzeug auf Basis eines Tata eVista dank eines neuen Konzeptes aufgebaut wurde.

Ein neuartiger robuster Fahrzeugbeobachter wurde entwickelt um die integrierten Fahrerassistenzsysteme optimal zu unterstützen. Das Konzept des Beobachters basiert auf einem erweiterten Kalman Filter unter Verwendung eines nichtlinearen Fahrzeugmodells und des Dugoff Reifenmodells.

Zusätzlich wurde eine Parameterschätzung sowie ein Plausibilitätscheck der Sensorsignale integriert, um die Robustheit des Beobachters zu erhöhen. Die Parameterschätzung von Fahrzeugmasse, effektiven Reifenradien und Haftreibung wurde mit Hinblick auf die Berechnungslast ereignisbasierend aufgebaut. Im Plausibilitätscheck werden sowohl fehlerhafte oder verzögerte Signale detektiert als auch korrigiert. Hier ist das neu entworfene Ersetzen von verzögerten oder fehlenden Sensorsignalen auf Basis der Theorie der Markov Ketten hervorzuheben. So kann auch bei einem Sensorausfall die Korrektheit der Ausgangssignale für einen gewissen Zeitraum und dadurch auch die Sicherheit des Fahrzeugs unter Assistenzkontrolle garantiert werden. Die Evaluierung der Stabilitätsgrenzen für das Fahrzeug sowie die Berechnung der gefahrenen Strecke für das Kombiinstrument werden mit den zuvor ermittelten Größen durchgeführt. Nach der modellbasierten Entwicklung wurde die Software auf der Hardware des Prototypen integriert. Ergebnisse bei dynamischen Testfahrten zeigen die Funktionalität dieses Konzepts.

List of publications

1. *Improvement of EE Architecture Design using Functional Approach* (B. Chretien, F. Holzmann, D. Gruyer, S. Glaser, M. Korte and S. Mammar),
   In Proceedings of the **FISITA 2010 World Automotive Congress**, Budapest, Hungary, June, 2010.

2. *Torque Vectoring with a feedback and feed forward controller - applied to a through the road hybrid electric vehicle* (G. Kaiser, F. Holzmann, B. Chretien, M. Korte and H. Werner),
   In Proceedings of the **2011 IEEE Intelligent Vehicles Symposium** (IV), Baden-Baden, Germany, June, 2011.

3. *Development of an adaptive vehicle observer for an electric vehicle* (M. Korte, F. Holzmann, V. Scheuch and H. Roth),
   In Proceedings of the **European Electric Vehicle Congress** (EEVC), Brussels, Belgium, 2011.

4. *Two-Degree-of-Freedom LPV Control for a through-the-Road Hybrid Electric Vehicle via Torque Vectoring* (Q. Liu, G. Kaiser, S. Boonto, H. Werner, F. Holzmann, B. Chretien and M. Korte),
   In Proceedings of the **50$^{\text{th}}$ IEEE Conference on Decision and Control and European Control Conference** (CDC-ECC), Orlando, FL, USA, December 2011.

5. *Design of a robust plausibility check for an adaptive vehicle observer in an electric vehicle* (M. Korte, G. Kaiser, V. Scheuch, F. Holzmann and H. Roth)
   In Proceedings of the **16$^{\text{th}}$ Advanced Microsystems for Automotive Applications**(AMAA), Berlin, Germany, May 2012.

6. *Robust Vehicle Observer to Enhance Torque Vectoring in an EV* (M. Korte, F. Holzmann, G. Kaiser and H. Roth,),
   In Proceedings of the **5$^{\text{th}}$ Fachtagung: Steuerung und Regelung von Motoren und Fahrzeugen** (AUTOREG), Baden-Baden, Germany, June 2013.

7. *Design of a Robust Adaptive Vehicle Observer Towards Delayed and Missing Vehicle Dynamics Sensor Signals by Usage of Markov Chains* (M. Korte, G. Kaiser, F. Holzmann and H. Roth)
   In Proceedings of the **2013 American Control Conference** (ACC), Washington D.C., USA, June 2013.

8. *Torque Vectoring for an Electric Vehicle - Using an LPV Drive Controller and a Torque and Slip Limiter* (G. Kaiser, Q. Liu, C. Hoffmann, M. Korte and H. Werner),
   In Proceedings of the **51st IEEE Conference on Decision and Control**(CDC), Maui, Hawaii, USA, December 2012.

9. *Torque Vectoring for a Real, Electric Car – Implementing an LPV Controller* (G. Kaiser, M. Korte, Q. Liu, C. Hoffmann and H. Werner),
   In Proceedings of the **19th World Congress of the International Federation of Automatic Control**(IFAC), Cape Town, South Africa, August 2014.

Contents

Nomenclature

Acronyms

ABS	Anti-lock Braking System
ACC	Adaptive Cruise Control
ADAS	Advanced Driver Assistance Systems
AEB	Autonomous Emergency Braking
AMR	Anisotropic Magnetoresistance
ASIL	Automotive Safety Integrity Level
ASR	Anti-Slip Regulation
CAN	Controller Area Network
CC	Cruise Control
CoG	Centre of Gravity
CVSI	Characteristic Vehicle Stability Indicator
DEKF	Dual Extended Kalman Filter
DGPS	Differential Global Positioning System
DLC	Double Lane Change
DoF	Degree of Freedom
DU1	Decision Unit 1
DU2	Decision Unit 2
ECU	Electronic Control Unit
EKF	Extended Kalman Filter
ESC	Electronic Stability Control
EV	Electric Vehicle
GRV	Gaussian Random Variable
GUI	Graphical User Interface
HiL	Hardware in the Loop
HMI	Human Machine Interface
ICE	Internal Combustion Engine
LKAS	Lane Keeping Assistant System

LMI	Linear Matrix Inequality
LPV	Linear Parametric Varying
NHTSA	National Highway Traffic Safety Administration
NMSE	Normalised Mean Square Error
OBD	On-board diagnostics
OEM	Original Equipment Manufacturer
PDU	Power Distribution Unit
PID	Proportional-Integral-Derivative
RLS	Recursive Least Squares
RMSE	Root Mean Square Error
RS	Random Sequence
RTI	Real-Time Interface
SI	International System of Units
SKF	Standard Kalman-Filter
SOC	State of Charge
SOH	State of Health
STM	single track model
TCS	Traction Control System
TMETC	Tata Motors European Technical Centre
TorVec	Torque Vectoring
TSL	Torque Slip Limiter
UKF	Unscented Kalman-Filter
UT	Unscented Transformation
VDC	Vehicle Dynamics Control
VHU	Vehicle Head Unit
WIVW	Wuerzbuger Institute for traffic scientific

List of symbols

α	Tyre side slip angle
β	Side slip angle of the vehicle
χ	Probability for a state in Markov Chain
Δ	Kronecker delta function
δ	Steering angle

$\dot{\omega}$	Wheel angular acceleration
ϵ	Tyre radius change by deflation
Γ	Input coupling matrix for time-discrete systems
γ	Curvature
κ	Scaling parameter for the Gaussian distribution
λ	Longitudinal tyre slip
ω	Angular velocity
Φ	State transition matrix for time-discrete systems
ϕ	Rotation around the x-axis
ψ	Rotation around the z-axis.
σ	Maximum gradients of sensor signals
ρ	Gain vector
τ	Forgetting factor
Θ	Parameter vector
θ	Rotation around the y-axis.
ζ	Adjacent tendency value for Markov Chains computation

1 Introduction

In nowadays vehicle control systems are widely used to enhance the safety and comfort. Since 1995, when the first series of Vehicle Dynamics Control (VDC) systems was developed and staked in serial cars, the functionalities and importance in automotive engineering increased incessantly. Through augmented VDC in vehicles the number of traffic accidents could be reduced and thereby lives saved. Furthermore, the influence of software on the vehicle dynamics by direct access to the actuators was increased. In 1.1 the most common VDC and their influence on the vehicle dynamics that are equipped in newly produced serial cars are shown. Anti-lock Braking System (ABS), Traction Control System (TCS), Cruise Control (CC) and Adaptive Cruise Control (ACC) influence the longitudinal vehicle dynamics where Electronic Stability Control (ESC) and Lane Keeping Assistant System (LKAS) control the lateral dynamics of the vehicle. Additionally, the function Torque Vectoring (TorVec) that controls the longitudinal and lateral dynamics is listed.
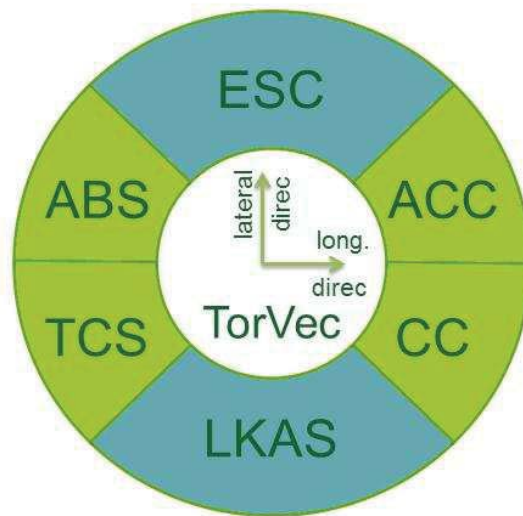
Figure 1.1: Varierty of VDC and their influence

An overview of the state of the art VDC functions and their functionality is given in [17]. By augmentation of VDC in vehicles, especially in electric vehicles, their Automotive Safety Integrity Level (ASIL) level becomes more critical and affords more sensors, more accuracy and more software functions [64]. Therefore, the ISO 26262 [35] specifies guidelines for necessary software safety mechanisms at the software architecture level.

By that time delay and missing measurements of vehicle dynamics sensors have received much attention in the last years since time delays and stoppage of signal flow exist in every electric vehicle architecture. In order to hit these requirements, to guarantee the needed accuracy of the sensors and to deal with sensor malfunctions a novel approach for a robust vehicle observer was developed.

In the eFuture project, which will be introduced in section 1.1, the function TorVec controls the torque of the two individual controllable electric machines in order to improve the performance, agility and safety of the vehicle. Besides the energy consumption can be minimized by the use of an optimal friction. In order to guarantee these aspects the function depends on reliable information. This will be provided by the vehicle observer and read as follows: vehicle velocity, side slip angle, yaw rate, acceleration and road-friction coefficients of the front wheels at any time.

Moreover, a new method based on Markov Chains for the handling of missing or delayed sensor signals was designed. These appearances often cause instability or performance degradation of the integrated VDC. The occurrence of communication delay [71], [72] and packet loss [68], [70] is as common as it is random. For example the VDC in an electric vehicle equipped with four individually assessable motors might bring the vehicle in an unstable state due to time delay or absence of important sensor signals. As the complexity and influence on vehicle dynamics of VDC will increase in the future [64] the issue of handling time delayed and missing vehicle dynamics sensor signals even gets more important. Consequently, this raises new requirements for vehicle safety demands. In order to come up with the defined correction mechanisms, a novel method for handling delayed and missing sensor signals to guarantee the vehicle and passenger safety will be presented. Additionally, the stability assessment computes the dynamic stability limits of the vehicle and the trip calculation outputs information about the covered distance. After an introduction to the the project eFuture, within this work was done, the used hardware is portrayed followed by the state of the art and the innovations that were created during that work. Afterwards the top level of the Vehicle Observer function will be presented. Thereafter, the objective and the organisation of work is outlined.

1.1 eFuture Project

The presented work was done within the project eFuture which is a research project funded by the European Community Seventh Framework programme (FP7/2007-2013) under grant agreement No. 258133. The project started in September 2010 with a duration of 3 years and 6 European partners from four different countries (see Fig. 1.2).

The main goals of this project were the development of a safe and efficient electric vehicle by hardware changes and a completely new functional architecture. This created platform should dynamically optimise its decision between performance and energy efficiency without compromising safety. As the optimization of each component is not sufficient an overall concept was mandatory to look at the interactions between the components. In

Figure 1.2: Partners of eFuture

the functional architecture, shown in Fig. 1.3, a layer model with the classical command and execution layer as the main axis for the driving has been chosen. The perception layer combines all environmental information via the driver and the exteroceptive sensors including navigation and eHorizon. In parallel, the energy layer accomplishes the control of the energy flows and the assignment of reserves for the domains driving, comfort and safety. This is a dynamical process depending on the driving situation and on driver requests. The assessment between Advanced Driver Assistance Systems (ADAS) and driver is performed by the Decision Unit 1 (DU1), thus defining the vehicle trajectory. Finally, on the execution layer, a safe actuator control is achieved by stabilising ADAS and the Decision Unit 2 (DU2) which chooses the appropriate actuator and the mode. This architecture allows an elegant implementation of standard and new functions and offers easy implementation and scalability for ADAS functions.

The basis vehicle was a Tata Indica eVista provided by the project partner Tata Motors European Technical Centre (TMETC). Details about the vehicle and the integrated hardware will be presented in 1.2.

Intedis as project leader was in charge of vehicle functions in the command and execution layer. Miljobil Grenland from Norway developed the high voltage battery, TMETC took care of the hardware integration and testing of the vehicle. Hella designed the integrated Vehicle Head Unit (VHU) and developed the software in the energy layer. IFSTTAR from France integrated the hardware and engineered software for the perception layer
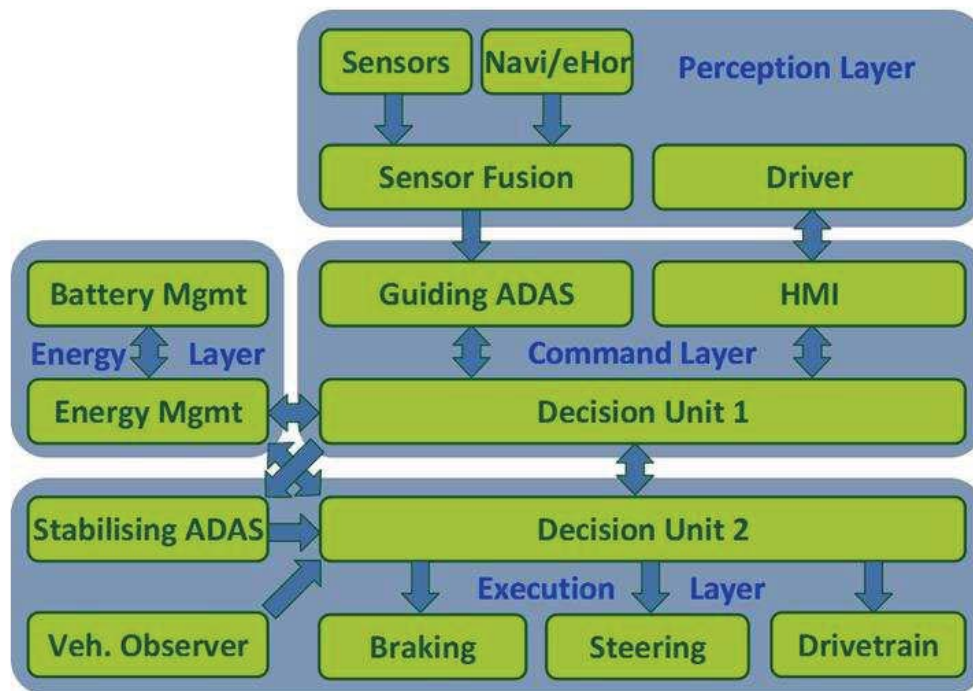
Figure 1.3: Functional Architecture

and the command layer. Their point of focus mainly laid on the integrated ADAS systems. The psychologists from the Wuerzbuger Institute for traffic scientific (WIVW) integrated additional screens and developed software for the Human Machine Interface (HMI).

1.2 Hardware Description

In order to get a better overview a short introduction to the hardware of the vehicle and especially the mounted sensors, which are source for the vehicle observer, shall be given. At the beginning most important components of the prototype are presented followed by the depiction of the characteristics of the three vehicle dynamic sensors.

1.2.1 Vehicle

The basis car for the eFuture project is a second generation Tata Indica Vista EV (see Fig. 1.4). The most relevant vehicle data are listed in Table 1.1 [63].

The single permanent magnet synchronous motor of the basis vehicle was replaced by two individually controllable permanent magnet synchronous AC electric machines on the front axle. Each of them has a peak torque of $750\,Nm$ and a continuous torque of $400\,Nm$ with a power consumption of $55\,kW$. The overall maximum system efficiency

Figure 1.4: Tata Indica Vista EV

Length	Width	Height	Accel.	Range	Charge Time	Weight
$3.795\,m$	$1.695\,m$	$1.550\,m$	$0-60\,kph:9s$	$165\,km$	$8\,h@220\,V$	$1250\,kg$

Table 1.1: Vehicle Dimensions

is at $95\,\%$. The speed range is limited to $2000\,rpm$ and the maximum voltage is $380\,V$. The electric machines, with $25\,kg$ weight each, are mounted within a frame at the centre of the engine bay together with the inverters, the Power Distribution Unit (PDU) and the high voltage battery charger. The motor torque transmission ratio is fixed to 1.

The battery of the prototype vehicle is designed and produced by the Norwegian project partner Miljobil. It is assembled with two strings of serially connected cells, where each row contains 180 cells. This Lithium Ion Super Polymer ($Li(NiCoMn)O_2$) battery is mounted on the rear bottom of the vehicle. The battery has a maximum capacity of $26,1kWh$ with an energy density of $103\,Wh/kg$. The duration of a fully charged battery is about 8 hours at 220 V. The discharge power is $44kW$ at a continuous discharge current of $200A$. The peak discharge current is restricted to $400A$. The nominal voltage is 220 V and the total weight of the package is 255 kg.

The integrated VHU, which was designed by Hella, contains four 32-bit micro-controllers Bolero MPC5607B (see Fig.1.5). It has five analogue inputs, eleven digital inputs, sensor and power outputs. For communication five different CAN channels are supported.

1.2.2 Sensors

In this section the equipped vehicle dynamic sensors will be explained in detail. The signals measured by these sensors are the source of the vehicle observer inputs and, thereby, the correct interpretation of all received signals is fundamental. For clarification the most important facts of the respective sensor, the exact placement and technical data for the yaw rate, steering angle and wheel speed sensor are described in detail. Where the wheel speed sensors are carry over parts of the basic prototype the remaining sensors were integrated supplementary.

Figure 1.5: Vehicle Head Unit

Yaw Rate Sensor

The implemented yaw rate sensor YRS 3 [25] from Bosch is a micro-mechanical acceleration sensor and is equipped with an additional Controller Area Network (CAN) interface (see Fig. 1.6). Besides the yaw rate of the vehicle it measures the longitudinal and lateral acceleration of the vehicle. This sensor replaced the existing sensor (DRS-MM 3.7k) that - in comparison to the new one - did not measure the longitudinal acceleration. The sensor is ideally mounted in the Centre of Gravity (CoG) of the vehicle. But as the exact CoG is difficult to determine and the number of suitable locations to fix the sensor in the vehicle is limited the original location directly behind the gear lever was chosen.

Figure 1.6: Yaw rate sensor YRS 3

This yaw rate sensor is part of the established group of vibrating gyrometers operating on the Coriolis principle. It consists of an inverse tuning fork with two mutually perpendicular linear vibration modes, drive circuit and evaluation circuit. A comb-like structure provides electrostatic drive and evaluation. The Coriolis acceleration is mea-

sured electro-statically by way of engaging electrodes. The measurement element is made up of two masses connected by way of a spring with the same resonance frequency for both vibration modes which is typically 15 kHz and, thus, outside the normal vehicle interference spectrum, making it resistant to disturbance acceleration.

The design of the acceleration module is comparable to that of the yaw sensor module and consists of a micro-mechanical measurement element and an electronic evaluation circuit. The spring-mass structure is moved in its sensitive axis by external acceleration and evaluated using differential capacitor in the form of a common structure.

The most relevant technical data for the vehicle observer of the rotation and linear acceleration sensor are listed in the table below:

Rotation sensor	
Measuring range	$\pm$ 160 $°/s$
Overrange limit	$\pm$ 1.000 $°/s$
Absolute resolution	0.1 $°/s$
Maximum offset	$\leq$ 3.5 $°/s$
Electrical noise	$\leq$ 0.2 $°/s$
Quantisation CAN	0.005 $°/s/digit$
Linear acceleration sensor	
Measuring range	$\pm$ 4.1 g
Overrange limit	$\pm$ 10 g
Absolute resolution	0.01 g
Maximum offset	$\leq$ 0.1 g
Electrical noise	$\leq$ 0.01 g
Quantisation CAN	0.0001274 $g/digit$

Table 1.2: Yaw rate sensor technical data

Steering Angle Sensor

For the measurement of the steering angle the Bosch steering-angle sensor [24] for angles between $-780°$ and $+780°$ was selected (see Fig. 1.7). Besides its integrated plausibility checks and special self-diagnosis functions, which makes it suitable for use in safety systems, the sensor has a CAN interface. In addition to the steering angle and the steering speed the sensor transmits several status signals. In detail there are the steering angle status, the checksum of all bytes of the CAN matrix and the message counter to identify lost messages between the reception of two messages. As the basic prototype was not equipped with a steering angle sensor the optimal location had to be figured out. Here, the position at the upper steering column nearby the steering wheel was chosen.

When mounted the steering column drives two measurement gears by way of a gear wheel for evaluation of the current steering angle. Magnets are incorporated into the measurement gears. Anisotropic Magnetoresistance (AMR) elements detect the angular position of the magnets as the resistance is a function of the magnetic field direction. The
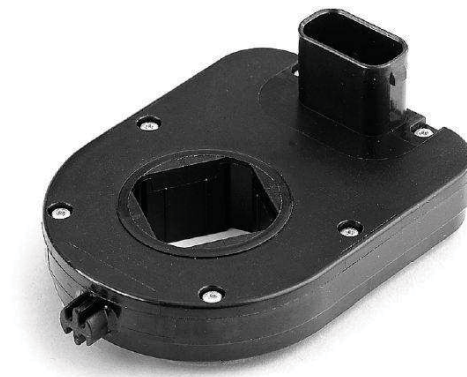
Figure 1.7: Bosch steering angle sensor

analogously measured values are supplied to the microprocessor via an A/D converter. The measurement gears have different numbers of teeth and their rotational position thus changes at different rates. The total steering angle can be calculated by combining the two current angles. After several turns of the steering wheel, the two measurement gears have returned to their original positions. This measurement principle can therefore be used to cover a measuring range of several turns of the steering wheel without the need for a revolution counter. The steering angle is given as an absolute value over the total angle range (turning range) of the steering column. A special feature of the sensor is the correct angle output immediately after switching on the ignition without moving the steering wheel (True Power On).The most relevant technical data to the vehicle observer of the rotation and linear acceleration sensor are listed in the table below:

Steering angle	
Measuring range	$\pm$ 780 $^\circ$
Absolute resolution	0.1 $^\circ$
Non-linearity	$\pm$ 2.5 $^\circ$
Steering speed	
Measuring range	$0 - 1016$ $^\circ/s$
Absolute resolution	$\pm$ 0.01 g

Table 1.3: Steering angle sensor technical data

Wheel Speed Sensors

The basic prototype is equipped with four DF11 sensors [26] from Bosch as angular wheel speed sensors (see Fig. 1.8). These are carry over parts from the integrated ABS and are thereby not affected by the hardware changes. They are mounted close to the wheel and, hence, they are exposed to heavy loads like temperature changes, vibrations, dirt and salt. Due to the location in the area of splashing water failures of the wheel

speed sensor during wet driving conditions are likely to happen. As the sensor is active it is connected to the $12\,V$ voltage source.

Figure 1.8: Bosch DF11 wheel speed sensor

The sensor supplies a signal with constant amplitude independent of the rotary speed and uses the Hall effect for the detection of the rotary speed signal. The application of this measurement principle permits speed measurement until almost standstill. In this way it is also possible to cover more difficult conditions of minimum velocity in, for instance, navigation system implementations. This sensor model does not detect the rotation direction of the wheels. The current signal is split into a $14\,mA$ and a $7\,mA$ level. Where the first level serves as information signal the $7\,mA$ signals attend as report information for the malfunction storage. For the signal transmission a two wire interface is used. The sensor is supplied by the low voltage on board electric system. In the VHU the received sensor current will be converted into a voltage signal through the measuring resistance. The analysis control will detect low or high signals by the amplitude of the voltage.

Since the wheel speed sensors are originally integrated for the ABS function and this data flow was not modified due to safety reason, the measured signals are received and processed by the ABS algorithms first. So the vehicle observer receives the preprocessed wheel speed sensor signals. These are the angular speed per minute and the status for each of the for wheels. The exact signal description is given in the following table:

Wheel speed		
Measuring range	$0 - 4095$	$1/pm$
Absolute resolution	1	$1/pm$

Table 1.4: Wheel speed sensor technical data
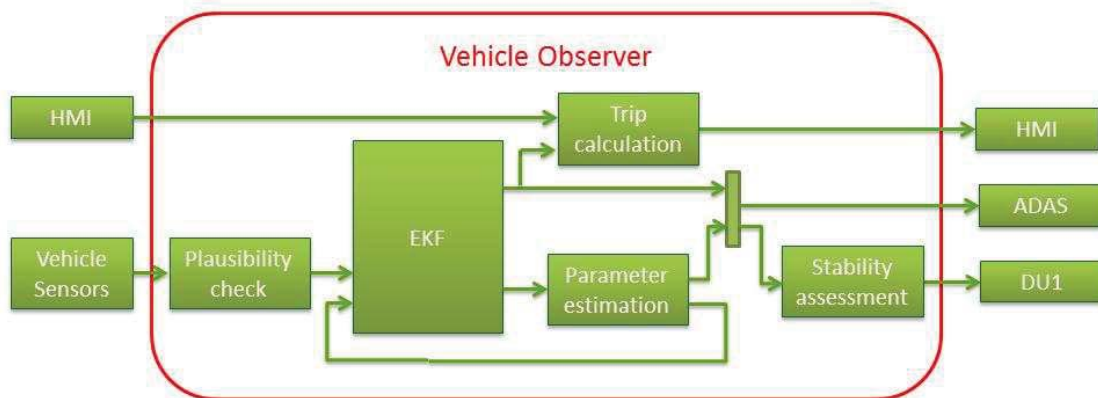
1.3 Function Description

Figure 1.9: Structure of the Vehicle Observer

The development of the function vehicle observer was done to enhance the performance of VDC functions since the reprocessing of the sensor signals provides more reliable information about the current vehicle states. In general, the vehicle observer gathers the available sensor signals which often are distorted due to imprecise sensors or electronic influences. The top level structure of the function with the main input sources and main receiving sinks is displayed in Fig. 1.9.

The algorithm first checks and, if possible, corrects the received sensor signals in the plausibility check subsystem. Based on an Extended Kalman Filter (EKF) concept the EKF subsystems lower the noise level of the measured vehicle states and calculate unmeasured vehicle states with the usage of a non-linear vehicle model and a Dugoff tyre model.

In the parameter estimation variable vehicle and environmental parameters are estimated. Here, a concept with low computational load was selected in order to make the complete algorithm runnable on the integrated hardware. By feedback of the estimated parameters to the EKF subsystems the equations of the vehicle model are updated which increases the accuracy of the complete function.

In the stability assessment subsystem the dynamic stability limits of the vehicle are computed and transmitted to the DU1 where these limits are considered and actuator requests are restricted to guarantee vehicle stability if necessary.

In the Trip Calculation subsystem the odometer and the tripmeter of the driven distance are computed and displayed in the HMI, here the instrument cluster. As the tripmeter can be reset by the driver at any time the event information of a pressed button in the HMI is considered.

A huge added value of this vehicle observer in an Electric Vehicle (EV) has the function Torque Vectoring which influences the lateral vehicle dynamics by torque distribution. By using the observed signals, which contain more information than measured by the

equipped sensors, this function is able to work more accurately and to improve vehicle safety and stability by enhancing the road contact. Also the energy consumption can be minimized by an optimal use of the maximum friction. Furthermore, the costs for the equipment of sensors are reduced because there is no need for expensive sensors like a side slip angle sensor.

1.4 State-of-the-art and Innovations

The presented work contains two innovative topics that together form the robust vehicle state and parameter observation. On the one hand the new design of a common vehicle state and parameter observation and on the other hand an innovative concept for the handling of delayed or missing sensor signals. Both novel approaches and the state of the art in the respective field of research are outlined in the next two subsections.

1.4.1 Vehicle state and parameter observation

Many technical approaches have been worked out in the area of vehicle state estimation. M. Best designed a concept with an EKF to realize the parallel estimation of vehicle states and parameters, but the change of road adhesion was not mentioned [12]. The use of extended Kalman-Bucy method in combination with Bayesian was presented by L. R. Ray in order to estimate vehicle states, tire forces and road friction coefficient. The main problem of this conception is the non-practicability in real-time due to the complexity of the algorithm [55]. D. Hu used the technique of a Dual Extended Kalman Filter (DEKF) to estimate the vehicle states and tire-road friction coefficient synchronously. This method improved the precision of the vehicle state estimation on adhesion-changing roads with standard sensors mounted on the vehicle [34]. Since this concept has still a high computational effort, the presented vehicle observer estimates the vehicle states with a single EKF. The calculation of variable and unknown parameters is realized through the usage of dynamical equations in driving situations when predefined values hold. Here, the parallel estimation of vehicle mass, effective tire radius and mobilized road friction is unique.

1.4.2 Handling of signal loss

Time delay and missing measurements of vehicle dynamics sensors have received much attention in the last years since time delays and stoppage of signal flow exist in every electric vehicle architecture (e.g. the architecture shown in Fig.1.10). Often these appearances are the cause for instability or performance degradation of the integrated VDC.
As stated before the occurrence of communication delay or packet loss of important vehicle dynamics signals might cause vehicle instability by inappropriate actuator requests from the VDC. By prospective increasing complexity and influence of VDC on the vehicle dynamics the issue of handling signal loss even becomes more important and raises new requirements for vehicle safety demands. The currently published ISO 26262 [35]
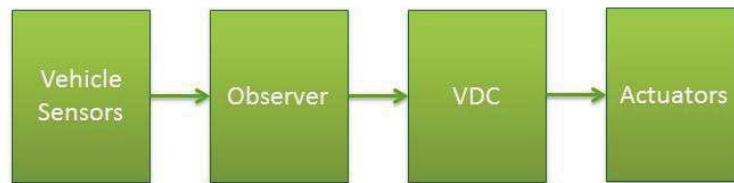
Figure 1.10: Vehicle dynamics architecture

specifies guidelines for necessary software safety mechanisms at the software architecture level. In order to fulfil the defined correction mechanisms a novel method for handling delayed and missing sensor signals to guarantee the vehicle and passenger safety was developed.

There were a lot of works dealing with the filtering problems for systems with missing measurements during the past years. Yang et al. [71] and Wang et al. [68] have summarized the research results about H_∞ filtering and control for various time-delayed systems with missing and delayed measurements for single sensors out of published literature on the respective topics. Moreover H_2 filtering [62] for multi-sensors in uncertain linear systems and H_∞ filtering concepts [45] for multi-sensors with classes of discrete-time stochastic non-linear systems have been developed. So far the research for robust Kalman filtering techniques focused on the classic Kalman Filter [41, 52] but not on EKF for the replacement of delayed and missing sensor signals. Up to now either signals were replaced by their last measured values [48], or the output is set to zero [33] or state estimates [30] are used as outputs to the VDC. Recently Kluge et al. [43] analysed the stochastic stability of EKF with intermittent observations. Unfortunately, there is no applicable concept for the replacement of missing and delayed signals that guarantees the correct execution of VDC.

In this work the use of Markov Chains is proposed to handle delayed and missing sensor signals in order to improve the vehicle state and parameter estimation which is the basic information for the commands of the VDC for the actuators. Here, the Markov Chain algorithm was selected since the concept does not make any assumptions about the system behaviour in the past and the complexity of the algorithm is still capable for online integration in the vehicle.

Similar to [60] and [61] the delays and missing measurements are modelled by Bernoulli distributed white sequences satisfying the known conditional probability distributions.

1.5 Objective and organisation of work

For the development of the robust vehicle state and parameter observer the model-based design method was chosen. By applying this method function verification is enabled from the beginning and obvious errors can be identified and corrected directly before

the software is integrated into the target hardware. Ideally, this should safe time by decreasing the number of debug steps that are necessary when the software is deployed on the hardware. In order to utilise the model-based design a comprehensive electric vehicle simulation model has been designed and calibrated with measurements of the real prototype. This model and the basic vehicle dynamics are introduced in chapter 2. The presentation of the joint approach for the vehicle state and parameter observation for an optimal support of VDC based on the sensor measurements is given in chapter 3. Here, the theory for the complete concept of a discrete vehicle observer is explained.

In chapter 4 the signal replacement during phases of sensor signal delay or absence with the use of Markov Chains is shown. This temporary signal replacement improves the robustness of the vehicle observer and, moreover, avoids VDC actuator requests that could led to vehicle instability.

Validation results of the complete concept are presented in two ways: On the one hand the normal performance with prototype test drives and on the other hand the malfunction performance with software in the loop tests. The most significant outcomes are merged in chapter 5.

Finally, the discussion of results and a conclusion are given in chapter 6.

2 Vehicle simulation model

This chapter describes the vehicle simulation model that was designed to validate the function itself and the complete system existing of driver, VDC, vehicle, environment and sensors (see Fig. 2.1). In general, simulation tools and models are widespread in industry and research fields of application and, thereby, the focus of every simulation model is different. A vehicle energy simulation, for instance, needs a fast execution time for long time simulations while there is no claim for high accuracy of the vehicle dynamics.
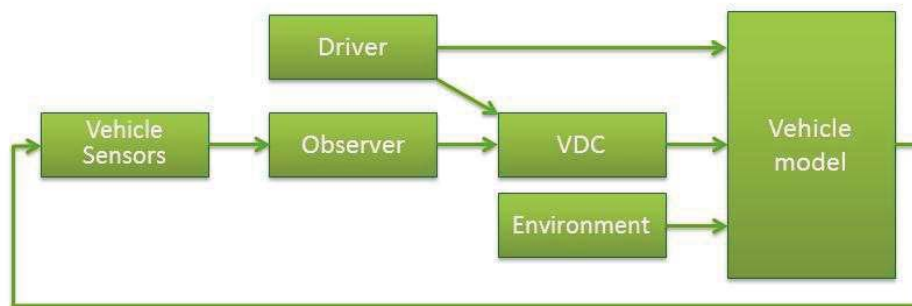

Figure 2.1: Top level vehicle model

The following vehicle simulation is supposed to predict the vehicle behaviour on internal inputs and external influences as close to reality as possible. Internal inputs include driver commands such as steering wheel angle and accelerator pedal position, whereas external influences include for example road friction or air drag. Since the highest accuracy for vehicle dynamics could be achieved by application of physical laws but also with more computational effort, finding compromise/balance between execution time and accuracy is highly significant.

A non-linear vehicle model for the vehicle dynamics and the most important components of an electric vehicle that were implemented are explained in the next section (2.1). These are the electric machines, the inverter, the high voltage battery, the hydraulic brakes, the tyres and the steering column of the vehicle. In order to get an electric vehicle simulation model that is as close as possible to the real prototype additional calibration work was necessary. Afterwards, the basic functionality of most common VDC is presented in 2.2. Finally, the driver model and the simulated test manoeuvres are introduced in section 2.3.

2.1 Vehicle model

In this section definitions and connections of the vehicle dynamics that are necessary to build the basis of a vehicle model will be presented. Subsequently the most important components of a vehicle in general and especially for an electric vehicle are introduced. Finally, the tuning of the vehicle model is explained.

2.1.1 Vehicle dynamics

Broadly speaking, the vehicle can be considered as single point with the given mass M at the CoG and a moment of inertia I. In the defined coordinate system (Fig. 2.2) the CoG moves along three dimensions. The positive x-axis is along the forward longitudinal direction of the vehicle, the positive y-axis points from the forward driving direction view to the left and the positive z-axis is to the top side of the vehicle. The vehicle can also rotate around these three axis. The rotation around the x-axis is specified as roll angle ϕ, the rotation around the y-axis is known as pitch angle θ and the rotation around the z-axis is determined as yaw angle ψ.
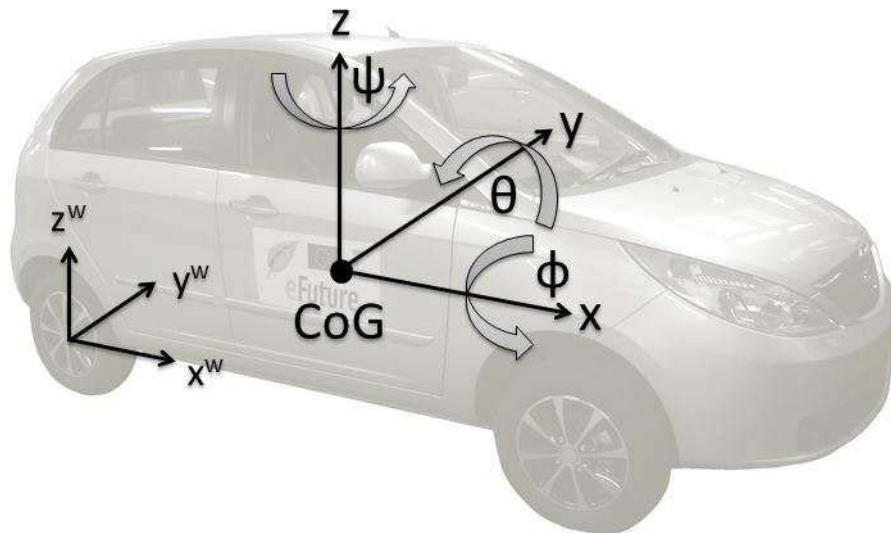
Figure 2.2: Coordination of the three dimensional vehicle

Opposed to the mentioned movement of the CoG the four contact points - front left (FL), front right (FR), rear left (RL) and rear right (RR) - of the vehicle to the road surface are fundamental. These are the only locations where the vehicle can transfer forces the environment and, by that, effect the vehicle motion. As this vehicle coordinate frame is not indicated at all the wheel coordinate frames are labelled with a superscripted ^{w} (see Fig. 2.2). The orientations of these frames are different from the vehicle frame if the wheels have a steering angle and the position of the wheel frames changes due to horizontal movement of the vehicle.

With the definition of coordinates for the vehicle body and the four wheels the vehicle motion is computed by usage of equations of motions from Newton and Euler [36].

$$M(a - v \times \omega) = F = F_{ext} + \sum_{i=1}^{4} (F_{wheel,i} + F_{susp,i}) \tag{2.1}$$

$$I(\alpha - \omega \times \omega) = M = M_{ext} + \sum_{i=1}^{4} (M_{wheel,i} + M_{susp,i}) \tag{2.2}$$

The forces generated by the wheels $F_{wheel,i}$ and by the suspension $F_{susp,i}$ move the CoG of the vehicle depending on the forces $F = [F_x, F_y, F_z]^T$ and the moments $M = [M_x, M_y, M_z]^T$. In addition, external forces F_{ext}, air drag and rolling resistance, influence the CoG motion as well. Here, both external functions are modelled by empirical functions which are dependent on the vehicle speed. For simplification the influence of external moments was neglected during this work. Suspension forces F_{susp} and moments M_{susp} are modelled by a spring-damper model where the tire dynamics are transmitted to the vehicle chassis under consideration of the road height. The subscripted character i stands for the wheels where $i = 1$ is for the front left, $i = 2$ for the front right, $i = 3$ for the rear left and $i = 4$ for the rear right tyre. The resulting moment M can be computed when the forces and geometric properties of the vehicle are known. With the use of the calculated moment M and the knowledge of the initial values the three dimensional acceleration $a = [a_x, a_y, a_z]^T$ and the three dimensional angular acceleration around the coordinate axes $\alpha = [\alpha_x, \alpha_y, \alpha_z]^T$ can be computed with the knowledge of the initial values of the velocity v_0 and the angular velocity ω_0. The velocity $v = [v_x, v_y, v_z]^T$ and the angular velocity $\omega = [\omega_x, \omega_y, \omega_z]^T$ are defined as integrals of the acceleration a and the angular acceleration α:

$$v = \int a \, dt + v_0 \tag{2.3}$$

$$\omega = \int \alpha \, dt + \omega_0 \tag{2.4}$$

For a model-based function development of the vehicle observer it is sufficient to have a realistic vehicle model and, therefore, to calculate the effects of vehicle dynamics (2.1 - 2.4). These equations describe the effects of the vehicle motion depending on the acting forces. Furthermore, the position of the vehicle in the global coordinate frame $p^g = [p_x^g, p_y^g, p_z^g]^T$ is required for functions like LKAS or ACC or, moreover, for the visualisation of the vehicle in its environment. To calculate the global vehicle position p^g, the velocity of the vehicle v has to be converted into a vehicle velocity in global coordinates v^g, with the transformation matrix T. Similarly, the global vehicle angle $\Phi^g = [\phi^g, \theta^g, \psi^g]^T$ is computed from the angular velocity of the vehicle ω^g which is represented in the global coordinate system.

Integrating the velocity v^g and the angular velocity ω^g, with respect to time, defines the

global position p^g and the angle Φ^g with

$$p^g = \int v^g \, dt + p_0^g \tag{2.5}$$

$$\Phi^g = \int \omega^g \, dt + \Phi_0^g, \tag{2.6}$$

where p_0^g defines the initial vehicle position and Φ_0^g the initial angle in the global vehicle coordinate system.

The transformation matrix T is defined as

$$T^g = \begin{bmatrix} 1 & 0 & 0, \\ 0 & \cos\phi^g & \sin\phi^g \\ 0 & \sin\phi^g & \cos\phi^g \end{bmatrix} \begin{bmatrix} \cos\theta^g & 0 & \sin\theta^g \\ 0 & 1 & 0 \\ \sin\theta^g & 0 & \cos\theta^g \end{bmatrix} \begin{bmatrix} \cos\psi^g & \sin\psi^g & 0 \\ \sin\psi^g & \cos\psi^g & 0 \\ 0 & 0 & 1 \end{bmatrix} \tag{2.7}$$

and converts the vehicle velocity v and the angular velocity ω into the same properties but in the global coordinate frame ^{g} with

$$\begin{aligned} v^g &= T^g v \\ \omega^g &= T^g \omega. \end{aligned} \tag{2.8}$$

For the transformation matrices T the superscript indicates the new coordinate system where the subscript defines the actual coordinate system. So T^g defines the transformation from the vehicle coordinate system to the global coordinate system.

The vehicle side slip angle, that describes the angle between the vehicle velocity vector and the longitudinal vehicle axle, is defined by:

$$\beta = \arctan\left(\frac{v_y}{v_x}\right). \tag{2.9}$$

The side slip angle is an important indicator of the vehicle stability.

2.1.2 Components

After the discussion of the theoretical basis of the vehicle motion for a simulation model the focus now lies on the generation of the resulting wheel forces and the components. These forces are mainly generated by the propulsion system. In a pure electric vehicle this propulsion system generally is composed of electric machines, hydraulic brakes and the centrifugal forces. In the following section, these components, their respective direct connected components and the used tyre model will be introduced. Firstly, the tyre model that is used is presented, afterwards the components of the electric propulsion chain are introduced. Subsequently, the model of the hydraulic brakes is shown and, finally, the model of the steering column is presented.

Tyre model

As the tyres are the only connection between the surface and the vehicle body the tyre model has a big influence on the vehicle movement. It generates the lateral and longitudinal forces from the vehicle body to the ground and vice versa. Moreover, the tyres act as springs and dampers for the vertical movement of the vehicle. Just like the number of different tyres, e.g. for winter or summer, the number of tyre models is large. So the selection of the appropriate one is very important. The highly non-linear character of the connection between the tyre and the road surface is problematic for the development of every model. This connection varies and can, until now, not be understood sufficiently. There are only few models which approximate the behaviour of the tyres. But most models show the force characteristic that is shown in Fig. 2.3.
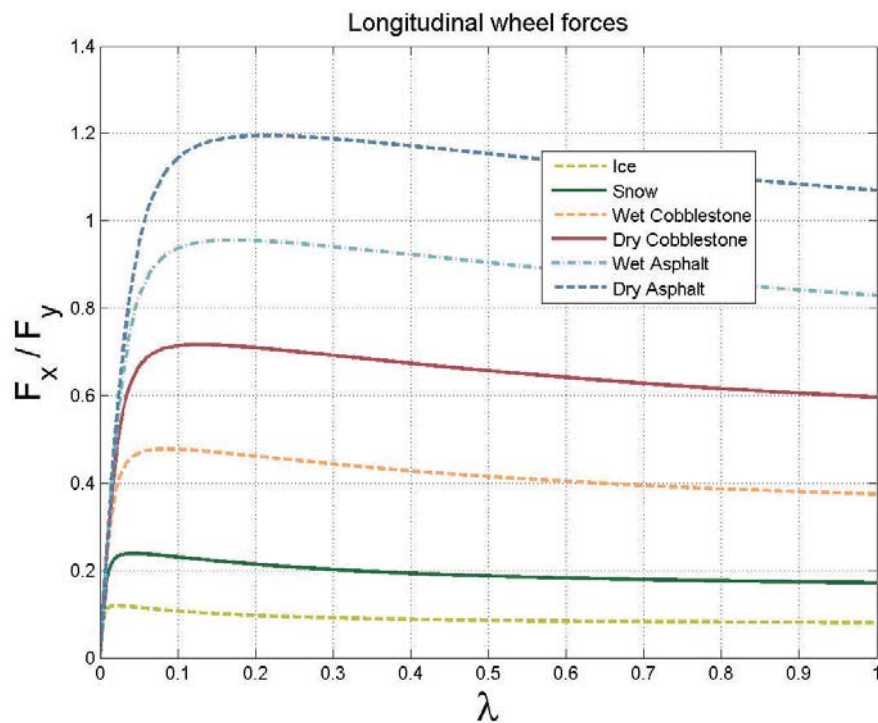

Figure 2.3: Wheel force generation over wheel slip

Most common and used tyre models are the extended Burckhardt model [42], the basic Dugoff model [54] and the Pacejka tyre model [51]. The Burckhardt and the Dugoff model are based on a physical concept and promise medium accuracy at low computational effort. In contrast, the Pacejka model is based on measured data and pledges high accuracy at medium computational load. The biggest advantage of the Pacejka model is its high scalability towards the aimed behaviour and, thereby, this model is used in the vehicle simulation model. As the model needs the longitudinal tyre slip λ and the wheel side slip angle α as inputs their definition is given before the Pacejka model is

explained.

Basically, the wheel angular acceleration $\dot{\omega}$ changes due to the applied torque changes according to:

$$
\begin{aligned}
\dot{\omega}_i &= \frac{1}{I_{w_i}} \left(T_i^{drive} - T_i^{brake} - F_x^{w_i} r_{eff_i} \right) \\
&= \frac{1}{I_{w_i}} \left(T_i^{drive} - T_i^{brake} - T_i^{fric} \right)
\end{aligned}
\tag{2.10}
$$

Here, I_{w_i} is the wheel moment of inertia, r_{eff_i} is the effective tyre radius and $F_x^{w_i}$ is the traction force. The free body diagram from side view of one wheel and the effective torques are shown in Fig. 2.4.
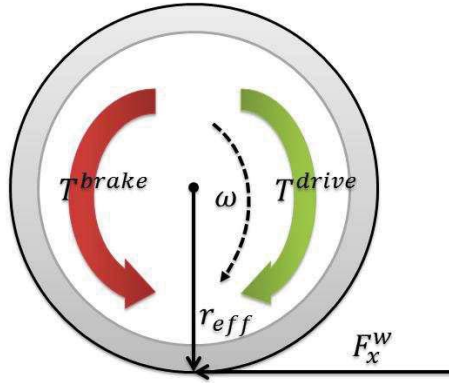

Figure 2.4: Wheel dynamics side view

The longitudinal force $F_x^{w_i}$ is computed based on the longitudinal tyre slip λ

$$
\lambda_i = \frac{\omega_i r_{eff_i} - v_x^{w_i}}{\max \left(|\omega_i r_{eff_i}|, |v_x^{w_i}| \right)},
\tag{2.11}
$$

where $v_x^{w_i}$ is the longitudinal velocity of the tyre centre in the tire coordinate system. Equation 2.11 is valid for all driving situations as there are traction, braking, reverse and forward driving and the range for λ is $[-1, 1]$. When computing the wheel side slip angle α

$$
\alpha_i = \arctan \left(\frac{v_y^{w_i}}{v_x^{w_i}} \right),
\tag{2.12}
$$

the lateral force $F_y^{w_i}$ and the restoring moment $M_z^{w_i}$ can be deduced with the use of the longitudinal $v_x^{w_i}$ and lateral $v_y^{w_i}$ velocity of the wheel. If these velocities are not known or available there is an alternative way to compute the longitudinal and side slip of the wheels instead. The velocity of any point of the vehicle can be calculated in detail when the longitudinal v_x and lateral v_y vehicle body velocity and the yaw rate r are known. Moreover, the signed longitudinal distance d_x from the point to the CoG and the signed

lateral distance d_y from the point to the CoG are necessary. The sign of these distances is defined within the coordinate system that is shown in Fig. 2.5.
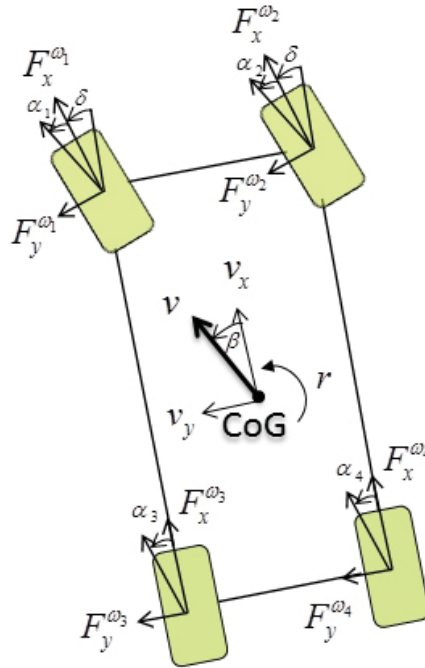

Figure 2.5: Definition of coordinate system

The velocity of the wheel is computed with:

$$
\begin{aligned}
v_x^{w_i} = v_{x_i} = (v_x - d_y r) \cdot \cos \delta_i + (v_y + d_x r) \cdot \sin \delta_i \\
v_y^{w_i} = v_{y_i} = (v_y + d_x r) \cdot \cos \delta_i - (v_x - d_y r) \cdot \sin \delta_i
\end{aligned}
\tag{2.13}
$$

As the steering angle of the wheel influences the wheel side slip angle α the formula is:

$$
\alpha_i = \delta_i - \arctan \left(\frac{v_{y_i}}{v_{x_i}} \right),
\tag{2.14}
$$

In most vehicle models it is assumed that the steering angle at the front axle is equal $\delta_1 = \delta_2$ and the steering angle at the rear axle is zero $\delta_3 = \delta_4 = 0$.

After the inputs of the Pacejka tyre model were introduced now the model itself will be presented. This model is named after its inventor Hans Peter Pacejka and is also known as the "Magic Formula" tyre model. As mentioned before it is empirical and requires a specific number of parameters determined from experimental measurements of tyre forces and moments. Here, 18 parameters are used to compute the longitudinal wheel

forces $F_x^{w_i}$, the lateral wheel forces $F_y^{w_i}$ and the restoring moments $M_z^{w_i}$ with

$$F_x^{w_i} = \left(D \cdot \sin\left(\arctan\left(B \cdot X_1 - E\left(B \cdot X_1 - \arctan\left(B \cdot X_1\right)\right)\right)\right)\right) + S_v \quad (2.15)$$
$$F_y^{w_i} = \left(D \cdot \sin\left(\arctan\left(B \cdot X_2 - E\left(B \cdot X_2 - \arctan\left(B \cdot X_2\right)\right)\right)\right)\right) + S_v \quad (2.16)$$
$$M_z^{w_i} = \left(D \cdot \sin\left(\arctan\left(B \cdot X_2 - E\left(B \cdot X_2 - \arctan\left(B \cdot X_2\right)\right)\right)\right)\right) + S_v \quad (2.17)$$
$$X_1 = \lambda + S_h \quad (2.18)$$
$$X_2 = \alpha + S_h, \quad (2.19)$$

where B, C, D and E are the tuning parameters and S_h and S_v are chassis-based parameters and vary for the calculations of forces and moments. The list of parameters is given in table 2.1.

Name	factor	$F_{x,front}$	$F_{y,front}$	$M_{z,front}$	$F_{x,rear}$	$F_{y,rear}$	$M_{z,rear}$
Stiffness factor	B	39.7	40.7	10	39.7	44.7	10
Shape factor	C	1.57	1.20	1.05	1.57	1.20	1.05
Peak factor	D	0.95	0.94	0	0.95	0.94	0
Curvature factor	E	0.96	0.88	-3	0.96	0.80	-3
Horizontal shift	S_h	0	0	0	0	0	0
Vertical shift	S_v	0	0	0	0	0	0

Table 2.1: Pacejka model parameters

Propulsion system

The electric architecture of the propulsion system is illustrated in Fig. 2.6. The battery provides electrical power, the PDU splits the DC energy to the two inverters which alter the energy to AC. Finally, the electric machines convert this electric energy to mechanical energy or vice versa. Due to the low functionality of the PDU the model of this component is not described further.

Battery model

The high voltage battery is the only energy source for the vehicle drive in a pure electric vehicle. The briefly presented model is designed as Li-Ion battery. The input is the current which is used by the electric load and the electric propulsion system. The outputs are the battery voltage which is supplied to the electric energy consumers, current limits for charging and discharging, State of Health (SOH) and State of Charge (SOC). Within battery efficiency, power losses and thermal influences are calculated to model the thermal and electrical dynamics of the battery. The model is composed mainly of lookup-tables that were developed based on real measurements.

High voltage battery

PDU

Left inverter

Right inverter

Left electric machine

Right electric machine

High Voltage AC Phase Wire
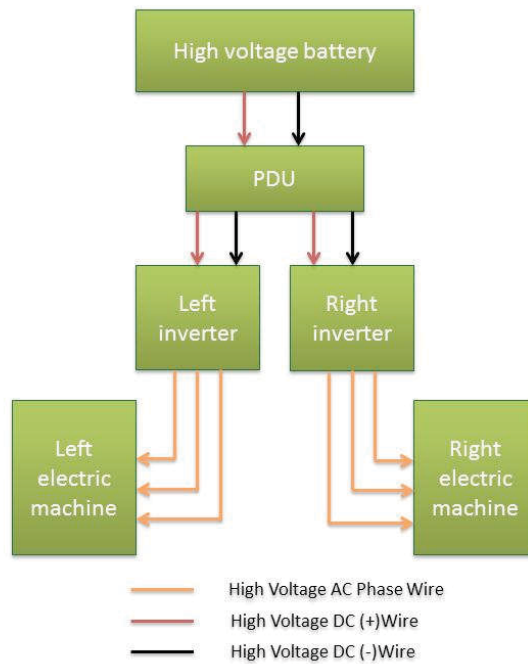High Voltage DC (+)Wire
High Voltage DC (-)Wire

Figure 2.6: Electrical architecture of the propulsion system

Inverter

As the inverters merely alternate the DC energy to an AC energy between the PDU and the electric machines but the model of the electric machines was designed to deal with DC energy there is no demand for a detailed inverter model in the simulation. So the inverter loss is taken into account only by implementation of a lookup-table that is based on values from the data sheet. In Fig. 2.7 this power loss is shown by the output current.

Electric Machines

The electric machine basically converts electrical energy to mechanical energy in order to accelerate the vehicle. Compared to a Internal Combustion Engine (ICE) the electric machine can recover energy additionally during vehicle deceleration by regeneration. By that, the overall efficiency of the electric machine performance is improved. The design of the electric machine, meaning the dimensioning and classification, defines the maximum torque and thereby the maximum vehicle acceleration which can be provided. In general, the machine torque T_m is depending on the angular velocity of the machine, so that the maximum torque decreases during higher angular velocities:

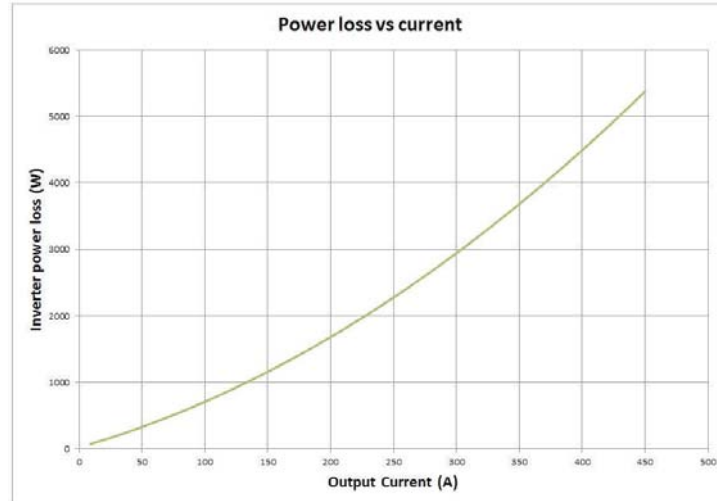$$T_m = \frac{P_m}{\omega}. \tag{2.20}$$

Figure 2.7: Inverter power loss

Fig. 2.8 shows the machine torque via the electric machine speed for different currents in the first quadrant. Most important is the solid black line that shows the maximum machine torque that can be applied. The electric machine has the same characteristic - high torque at low speed and low torque at high speed, in the other three quadrants. Moreover, the supplied voltage U, transmitted by the inverter, affects the energy losses since the current I has to be higher at lower supply voltage if the electric power P_e should remain constant according to:

$$P_e = U \cdot I. \tag{2.21}$$

Due to the higher current the power losses P_l increase as well with

$$P_l = R \cdot I^2. \tag{2.22}$$

Furthermore, the increased power losses would lead to a heated electric machine which would result in lower drive torque since the resulting mechanical power P_m is computed by

$$P_m = P_e - P_l. \tag{2.23}$$

The electric machine model was built as a physical system where the resulting torque is equal to the requested one in normal performance. The torque output might be limited by the maximum torque T_{max}, the power limit P_{max} or the torque slew rate limitation $\dot{T}_{max}$. Here, no limitations due to thermal, mechanical or communication reasons are considered since these effects are very complex and there is no need to include them in the model based design of the vehicle observer.
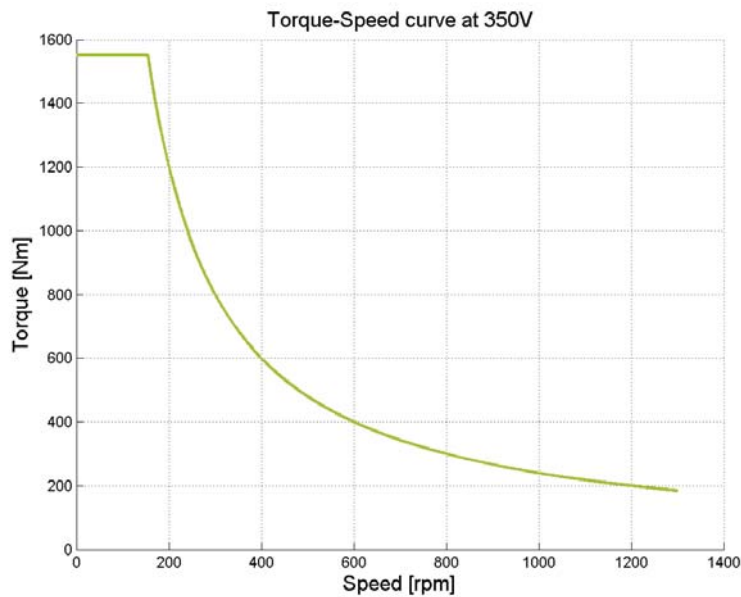
Figure 2.8: Machine torque over speed

Hydraulic Brakes

Hydraulic brakes generally convert mechanical energy to thermal energy which is then radiated off in the environment. So their performance is suboptimal in terms of efficiency. Additionally, the dynamic of the hydraulic brakes is by factor 10 slower than that of the electric machines. The accuracy of the control decreases. But as the electric machine torque is physically, as described in the previous section, and functionally limited, the maximum electrical deceleration without ESC is $-2m/s^2$. So there is still a need for the hydraulic brakes. To guarantee vehicle deceleration in any situation, e.g. during electric machine failure, the hydraulic brakes need to be implemented as well. By that redundancy was created which increases safety even more. The model of the hydraulic brakes apply a brake torque T_b to the tyre that is linear to the brake pedal position and signed to the wheel angular velocity ω.

Steering Column

The steering column model transmits the steering torque of the driver to the front wheels which results in a front wheel steering angle. The steering angle, in general, has a great influence on the vehicle dynamics and, thereby, the model is crucial to get a vehicle simulation model resembling the real prototype as much as possible. The inputs are the driver steering torque T_δ^{drvr}, the vehicle velocity v, the vehicle yaw rate r and the side slip angle of the vehicle β. The output is the resulting front wheel steering angle δ_f. The steering gear ratio R_s between the steering wheel and the front wheels is assumed to be constant. The steering aligning torque, that brings the steering angle back in the

neutral position, is computed by

$$T_\delta^{algn} = \frac{2 \cdot c_f \cdot \eta_t}{R_s} \cdot \left(-\beta - \frac{l_f \cdot r}{v} + 1 \right), \tag{2.24}$$

where c_f is the cornering stiffness of the front wheels, η_t is the effective tyre length contact and l_f is the longitudinal distance from CoG to the front axle. The steering angle of the front wheels changes according

$$\ddot{\delta}_f \cdot I_s = \left(-B_s \cdot \dot{\delta}_f + \frac{1}{R_s} \left(T_\delta^{drvr} - T_\delta^{algn} \right) \right), \tag{2.25}$$

with the steering system damping coefficient B_s and the inertial moment of the steering system I_s. Alternatively, the steering column model can receive the steering angle of the driver directly. In this case the input angle is divided by the steering gear ratio. In general the steering angle at the front wheels is limited to its physical maximum at $\delta_f^{max} = 0.3491\, rad$.

2.1.3 Model calibration

Up to now, the vehicle simulation model is able to describe the non-linear vehicle behaviour in its environment. But since deviations to the prototype behaviour, which might end up in time-consuming function parametrisation when integrating the code on the target hardware, are likely, there is calibration work to be carried out. Thus, the prototype was equipped with additional external sensors to log the most important vehicle dynamic states. Test drives for different driving manoeuvres - normal driving and high dynamic driving - were done. Afterwards, the recorded vehicle states were compared to the simulated vehicle states. Here, the inputs to the vehicle simulation model were the same as for the prototype. The environment was modelled as realistically as possible. The calibration work mainly is about tuning of vehicle parameters with great influence on the vehicle dynamics. These were partly measured and partly had to be tuned empirically until the deviation between measured and simulated vehicle states became acceptable. Where the vehicle mass, the moment of inertia and the tyre radius at standstill could be measured, other parameters, for instance the cornering stiffness of the tyres and damping coefficient of the steering column, had to be tuned heuristic.
The inputs to the model for this calibration work are the electric machine torques T_{eMach} and the steering wheel angle δ_{drvr}. From the huge amount of output signals from the simulation model the focus was directed to the vehicle states with the most informative value for the longitudinal and lateral vehicle dynamics. These are the longitudinal velocity v_x, the lateral velocity v_y and the yaw rate r. Subsequently, results for normal driving and high dynamic driving are shown.

Normal driving

During this scenario the driver steers and accelerates averagely without any sudden changes and thereby low specific rate of change. In Fig. 2.9 the steering angle and the

electric machine torques are shown. The torque difference between left and right electric machine is the result of TorVec which will be explained in the next section.
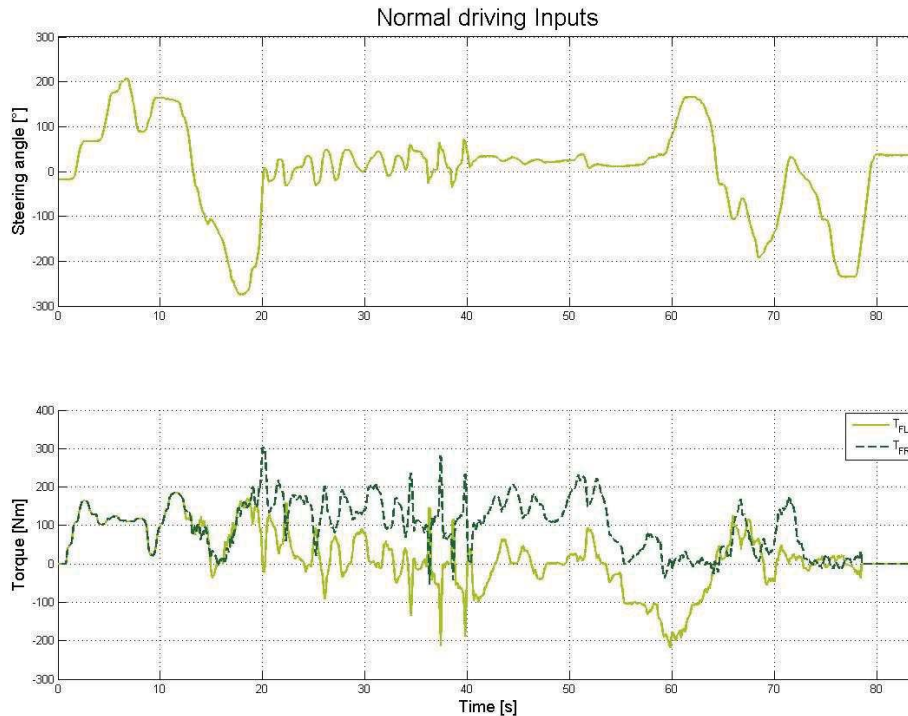

Figure 2.9: Model inputs at normal driving

In Fig. 2.10 the outputs of the simulation model and the measurements are displayed. Where the measured data are drawn with a solid line, the simulated data are displayed with a dashed line. From top to bottom the lateral velocity, the longitudinal velocity and the yaw rate are shown.

The simulated and measured lateral velocity of the vehicle have a certain deviation but the overall signal trend is almost identical. This deviation and the measured signal, which is noisy, are the result of the optical sensor [59] which was mounted on the outside right side of the car. So this deviation is not rated as critical.

The longitudinal velocity and the yaw rate of simulation and measurement are very similar. The light differences are negligible and result from the surface of the test track that is not perfectly plain. An adaptation of the road surface in the simulation model was not done since its low cost-benefit ratio.

The overall accuracy of the simulation model compared to the measurements of the prototype are sufficient for average driving manoeuvres.
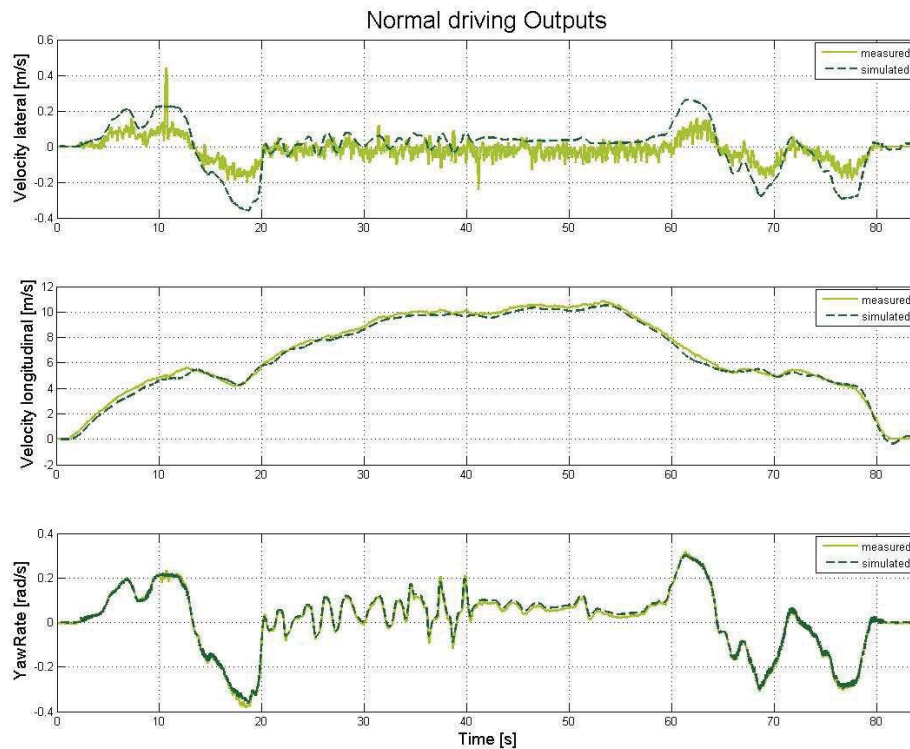
Figure 2.10: Model outputs at normal driving

High dynamic driving

For the high dynamic driving a Double Lane Change (DLC) manoeuvre was chosen which is described in detail in section 5.1.2. In general, this test is appropriate to push the vehicle to its lateral dynamical limits and, thereby, the vehicle performance is highly non-linear. Moreover, vertical dynamics with rolling and pitching effect the maximum tyre forces as well.

Fig. 2.11 shows the steering angle and the electric machine torques. From the beginning of the measurement the vehicle is accelerated to a desired velocity until $14\,s$. Then, the driver switches the gear to neutral to avoid effects resulting from the electric machines during steering. At $15\,s$ the vehicle reaches the test set-up and the driver tries to follow the given trajectory by a strong left-right-left steering. Like in the normal driving the different torques follow from TorVec to enhance the stability of the vehicle.

In comparison to the normal driving the torque and steering angle rates are much higher and, thereby, vehicle is moved to its stability limits.

In Fig. 2.12 the outputs of the measurements and the simulation model are displayed in the same order and with the same line types as before.

The lateral velocity of the simulation model and the measurements deviate in their
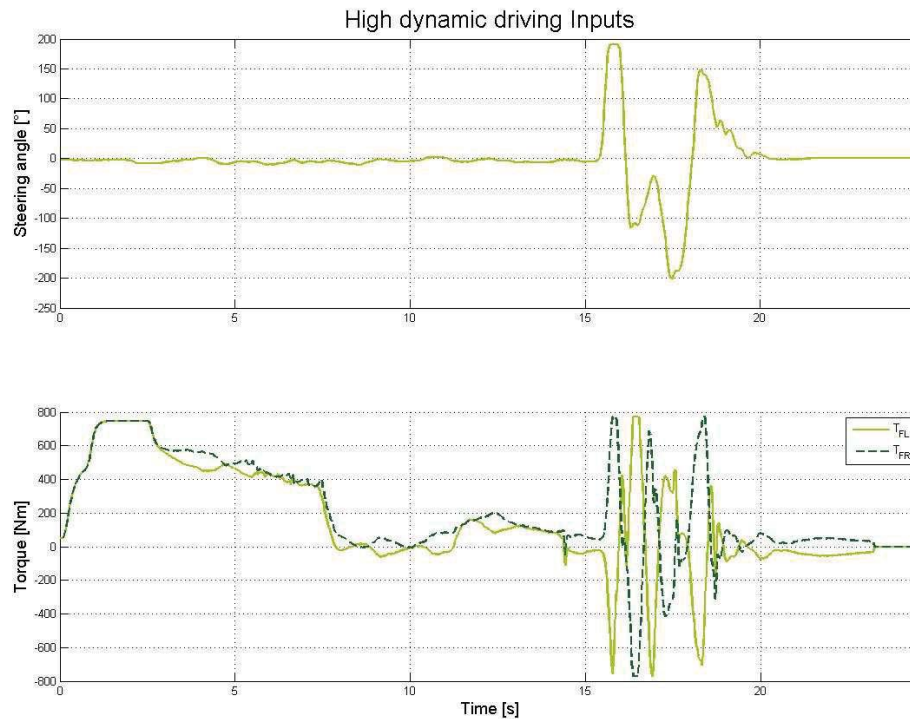
Figure 2.11: Model inputs at high dynamic driving

amplitude but the general trend is accord. Again, the sensor measurement method, the sensor calibration or the roll movement of the vehicle can be the root cause for that. Here, the sensor noise level is not that relevant due to the higher amplitudes of the signal during that scenario.

The longitudinal velocity of the simulation matches very well with the measurements. The slight deviations from $4\,s - 7\,s$ and $21\,s - 24\,s$ are based on the non-optimal road profile on the test track. Moreover, the non-linear behaviour of the external forces is not totally realistic in the simulation. The deviation during the steering movement between $16\,s$ and $19\,s$ is the result of vehicle body rolling which influences the measurements of the optical sensor.

A very accurate simulation of the yaw rate could be achieved with the vehicle simulation model. The light deviation in the amplitudes during the steering, $16\,s - 19\,s$, is negligible since unmeasurable environmental parameters cause them and the tyre model is not tuned for high dynamic scenarios exclusively.

In summary, the built and calibrated vehicle simulation model is able to give realistic data on the car behaviour compared to measurements from the prototype. In general, the calibration work has to find a trade-off between the longitudinal and the lateral vehicle dynamics. Additionally, these parameters should cover as many driving situations as
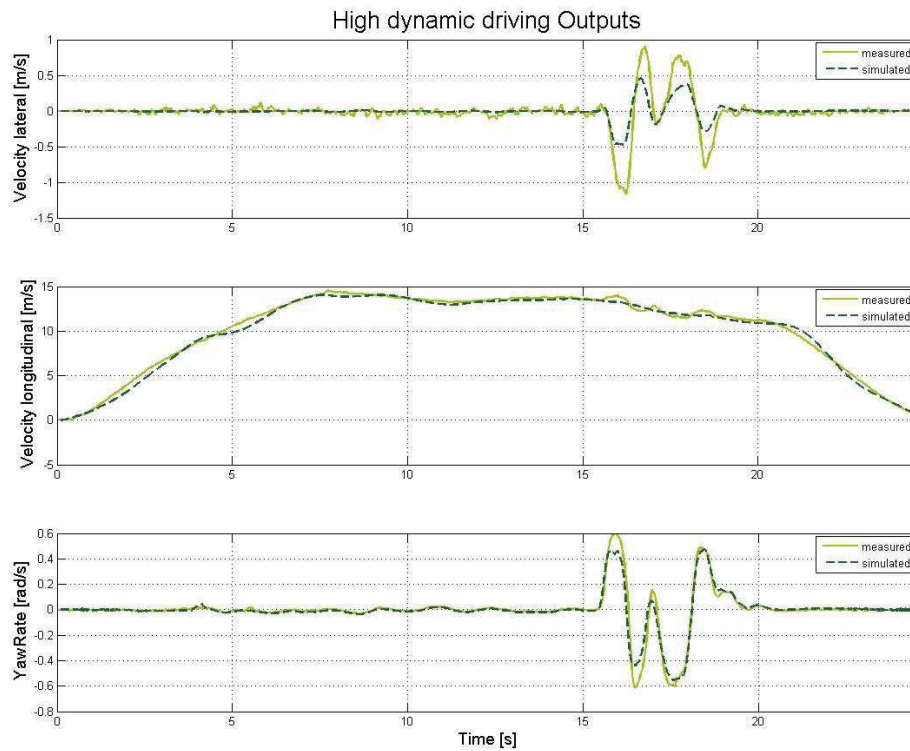
Figure 2.12: Model outputs at high dynamic driving

possible with a suitable accuracy. The here presented vehicle model generates vehicle states that mostly match the measured vehicle states in normal and highly dynamic driving.

2.2 Vehicle dynamics controller

After the model and most important components for basic vehicle motion were introduced in the previous section, now, the various VDC of the virtual prototype are described roughly. Since these VDC have direct influence on the vehicle dynamics the vehicle observer has to be tested during VDC activation. Moreover, the performance of the VDC can be simulated with pure sensor signals and with outputs of the vehicle observer. Thus, an enhanced vehicle stability with vehicle observer information and VDC can be proven. The presented VDC are split into stability control and assistance control.

2.2.1 Stability controller

As the basic vehicle has a lack of stability and controllability in emergency manoeuvres or road conditions with low road friction, stability controllers have become standard in passenger vehicles in the last years. Here, controllers which only act on the vehicle stability are presented: ABS, TCS, ESC and TorVec. Apart from these controllers, other functions that improve vehicle performance and driver comfort are integrated in serial cars as well. A well-established function is the Sky-Hook controller that acts on the suspension in order to minimize the body roll and pitch variation. But as the main purpose of functions like these is not the enhancement of the vehicle stability, although they are doing it indirectly, and they are not integrated in the prototype there is no description given here.
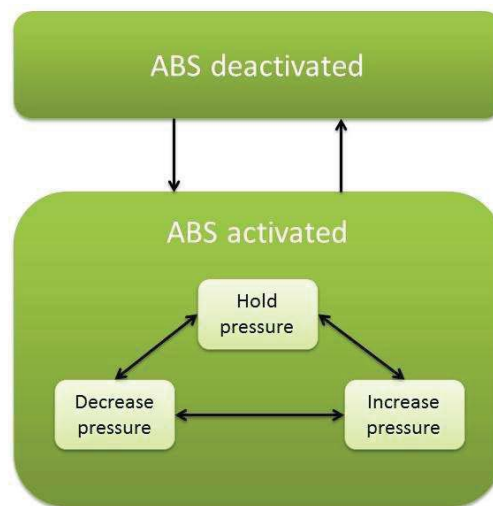
Anti-lock Braking System

Figure 2.13: ABS activation state machine

The ABS was the first stability control that was integrated in serial cars and was initiated in 1978. In nowadays vehicles the function individually controls the brake pressure of all four wheels by a 4-Channel ABS which is composed of four wheel speed sensors and four brake pressure valves. The lock of wheels during hard braking manoeuvres reduces the grip and thereby increases the braking distance. The additional by lock of steering wheels, caused by that, decreases the controllability of the vehicle which is why the ABS algorithm tries to keep the longitudinal wheel slip λ in a range of $0.08 - 0.25$. At this slip level a maximal grip domain is reached for almost all road conditions, see Fig. 2.3. Moreover, by preventing a locked wheel the tyre wear is equal which extends tyre longevity. The only drawback has the function at straight line braking on bulky roads where the building up of material in front of the slipping wheels is avoided and, thereby, the braking distance is longer in comparison to a locking wheel.

The ABS algorithm computes the specific longitudinal wheel slip λ_i with the information of the wheel speed from the sensor and the vehicle speed from the vehicle observer. Then, a finite state machine realizes the activation strategy - see Fig. 2.13.

The transition between activation and deactivation depends on whether the considered wheel is slipping or not.

When a slipping wheel is detected and the ABS is activated the brake pressure will be held by default and remains in this state if the wheel slip is in the range that is regarded as optimal. In case of higher wheel slip than this range or if the deceleration of the wheel exceeds a defined limit, the ABS sends commands to the valves in order to reduce brake pressure. In the same manner, the algorithm sends commands to the pumps to decrease the brake pressure if the wheel slip is lower than the optimal range or the acceleration exceeds a defined limit, which means that it is more efficient to brake the wheel than wasting energy by wheel slip.

Traction Control System

The TCS, also named Anti-Slip Regulation (ASR), is designed to control the motor torque and, thereby, prevent wheel slip during vehicle acceleration. Hence, the algorithm reduces the motor torque if a driven wheel slips. Similar to the ABS, the TCS guarantees the steering control for the driver, increases the life span of tyre and energy efficiency by avoiding burn-outs.

The TCS functionality in the prototype is integrated in the function TorVec. The explanation for that will be given in the following section.

Electronic Stability Control

ESC is currently the most advanced safety function embedded in mass-produced vehicles. It aims at accessing the vehicle state to avoid unstable driving situations in case of over- or understeering, as presented in Figure 2.14. To achieve this a vehicle stability domain is defined and provides orders to the actuators only if the vehicle transgresses this stability domain. Here, a standard ESC concept is introduced that uses differential braking in order to stabilise the vehicle. In detail, just one wheel is braked at the same time depending on the detected driving situation. To control the vehicle lateral dynamics the ESC needs sensor information of the angular wheel speeds, the steering angle, the lateral acceleration and the yaw rate. Additionally, information of road friction, longitudinal velocity, side-slip angle and tire slip, which all provided by a vehicle observer, are necessary.

The decision of activation of the ESC depends on the driving situation and the defined stability domain which are explained in the following. The stability domain is defined by computing maximum reference states for the yaw rate and the side-slip angle. As soon as one of the current vehicle states exceeds the corresponding maximum reference state the vehicle leaves the stability domain. The computation of these values is based on coefficients obtained through the analysis of the vehicle lateral dynamics. Based on the vehicle state information a Characteristic Vehicle Stability Indicator (CVSI) is de-
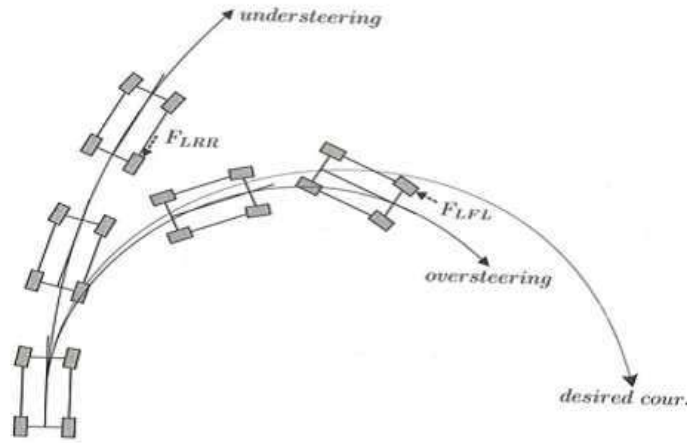
Figure 2.14: ESC principle

termined. The CVSI notifies if the vehicle is in over-, under- or neutral steering. The activation logic decides if the ESC should be active and which wheel should be braked by analysing the CVSI, vehicle state and maximum reference state information. Finally, the brake commands to the actuators are generated by the combination of the activation signals and the commands computed by the control algorithm that is explained as follows [13].

Once the maximum reference states are determined and the wheel to brake is selected, the ESC control algorithm computes the commands to the electro-valves. This control function is composed of two controllers in serial: the first one is an online-computed linear state space controller K_c, providing the targeted contact forces between the wheels and the road surface. The second controller is a PID controller, converting these forces into electro-valve commands. As the core of ESC is based on the computation of K_c, only the way to compute this feedback is presented here while the PID gains are calibrated empirically. The feedback controller, K_c, is calculated through a pole-placement-method, considering the vehicle as a linear system. To obtain a linear model of the vehicle dynamics, the reduced two track vehicle model f is considered and linearised online by computation of the Jacobian. The pole-placement state feedback, described in eq. (2.26), is performed considering the pole matrix G and the Moore pseudo-inverse of the system input matrix, i.e., $\left[\frac{\partial f}{\partial u}\right]^+$. The operating point changes at each iteration, being considered to be the previous current state of the model at the previous step.

$$K_c = \left[\frac{\partial f}{\partial u}\right]^+ \cdot \left(\frac{\partial f}{\partial X} - G\right) \tag{2.26}$$

Here u is the input vector, X is the state vector and G is the pole matrix.

Torque Vectoring System

The function TorVec influences the lateral vehicle dynamics by a torque distribution and, thereby, improves vehicle stability in extreme driving manoeuvres. Particularly, this function is very suitable for electrically driven vehicles with at least two individual controllable machines. The here presented TorVec has a joint approach for the control of the longitudinal velocity and yaw rate and limitation of the longitudinal wheel slip. It is designed for an electric vehicle with two electric machines on the front axle, like displayed in Fig. 2.15.
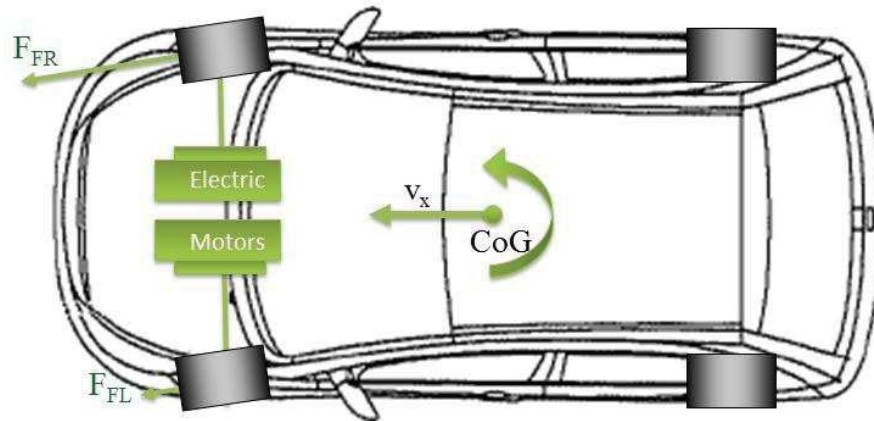

Figure 2.15: TorVec principle

The control scheme is a Linear Parametric Varying (LPV) control and the algorithm is based on a non-linear single track vehicle model [40]. The varying parameters are limited to a zone of normal driving between a longitudinal velocity range of $[12; 130]$ kph and a yaw rate range of $[-2; 2]$ rad/s. The stability and performance of the controller are ensured by applying the Lyapunov function, shaping filters and Linear Matrix Inequality (LMI)-conditions, H_∞ for stability and L_2 for performance. Furthermore, the concept respects the physical limits of the electric machines and the tyres. The electric machines are limited to power, maximum torque and torque rate where the tyres are limited to slip, vertical force and road friction.

In the control architecture shown in Fig. 2.16, the desired values for the longitudinal speed and the yaw rate are calculated based on the accelerator pedal position and the steering angle. The control inputs are computed by subtraction of the vehicle states, which are provided by the vehicle observer, from the desired values and an addition of Torque Slip Limiter (TSL) value. In the control algorithm a feed-forward and a feedback gain are computed with the additional input of the steering angle and result in a desired force for both front wheels. Finally, limitations of the TSL and a saturation lead to the applied wheel forces which are requested by TorVec.

Test drives with the prototype showed that the function entails an improved vehicle
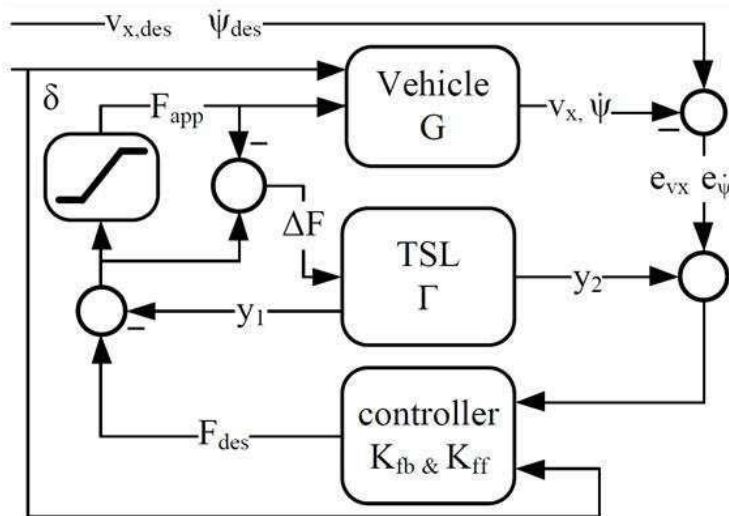
Figure 2.16: TorVec control architecture

performance for safety and comfort. A faster and more direct vehicle response to driver inputs, no spinning or blocking wheels during test drives and less under- and oversteering in high dynamic driving are the main factors for improved vehicle safety. The benefit of this function in terms of comfort is a smaller steering effort, in torque and angle, for the driver.

2.2.2 Assistance controller

Assistance controllers, also called ADAS, are designed to avoid accidents caused by driver mistakes and to increase driver comfort. In case of an impending situation they warn the driver or take over the vehicle control temporarily. In future, these controllers will be able to drive the vehicle fully autonomous without any driver commands. The augmentation of assistance controller in serial cars imposes new requirements on serial cars. The ASIL is more critical, more sensor information is needed with a maximum of accuracy and the software code which increases computational effort. Here, two assistance functions that are mostly integrated in nowadays serial cars and in the prototype are presented. These are the ACC for the longitudinal assistance and the LKAS for the lateral assistance.

Adaptive Cruise Control

When ACC is active, the basic control strategy is that the vehicle speed shall be controlled automatically either to maintain a distance to a heading vehicle, or to maintain the set speed, whichever speed is lower. The transition between these two control modes is regulated automatically by the ACC system.
In common ACC systems two different low level functions are used. In the speed control

mode, whenever no heading vehicle is detected, the vehicle speed must be controlled according to the driver-desired speed. The vehicle speed is regulated according to the heading vehicle speed in following control mode whenever a slower leading vehicle is detected. A validation subsystem finally handles error flags and respects functional and dynamic limits according to the current vehicle state. The functional top-level of the ACC is displayed in Fig. 2.17.
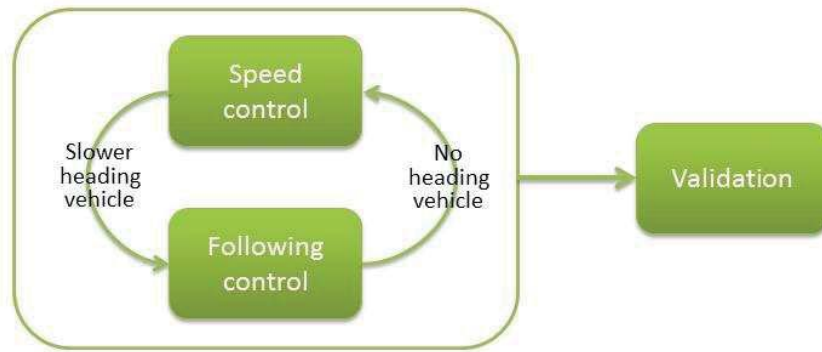

Figure 2.17: Top-level view of ACC function

During speed control mode the control error of the ACC algorithm is the difference between the driver selected speed v_{Drvr} and the current vehicle speed v:

$$e_{sc} = v_{Drvr} - v. \tag{2.27}$$

The requested vehicle acceleration from the ACC a_{ACC} is then computed by using this error and the speed control gain K_{sc}:

$$a_{ACC} = K_{sc} \cdot e_{sc}. \tag{2.28}$$

In following control, there are two control errors which have to be considered. The gap error which is calculated with the help of the distance to the heading vehicle d, the driver-desired time headway t_{Drvr} and the vehicle speed:

$$e_g = d - t_{Drvr} \cdot v. \tag{2.29}$$

The speed following error is the difference between the velocity of the heading vehicle v_h and the vehicle speed:

$$e_{sf} = v_h - v. \tag{2.30}$$

The aimed vehicle acceleration of the ACC in following mode is computed with the usage of the errors and gains for the gap K_g and the speed following K_{sf}:

$$a_{ACC} = K_g \cdot e_g + K_{sf} \cdot e_{sf}. \tag{2.31}$$

The validation subsystem achieves the control of the output with respect to the dynamic and functional limits. It raises an error flag as soon as the subsystem has to limit the output acceleration according to the previous limitation.

The function showed good performance for speed and following mode during test drives with the prototype on the test track. The final control error was sufficient, the driver selected gap was kept to the heading vehicle and the acceleration felt comfortable to the passengers.

An extended ACC version which respects a safe speed and includes an Autonomous Emergency Braking (AEB) was developed as well. The safe speed is calculated with the information of the road environment, like curves, road friction, and of a digital map, e.g. legal speed limits. By this speed limitation the function increases the energy efficiency compared to the presented basic ACC. The AEB applies the brakes in critical situations, independently of the driver, to avoid or mitigate the accident. Consequently, the distance to a front object is measured by perception functions and if this distance reaches a minimum safety distance (related to the ego vehicle speed), the brakes are autonomously activated. Since the extended ACC is out of focus in this work it is not described in detail here.

Lane Keeping Assistance System

The LKAS gets active when the driver is inattentive and the car is moving towards the lane border. In this case the algorithm takes over control for a limited time frame and moves the vehicle back to the middle of the lane (see Fig. 2.18). Similar to the effect of TorVec a controlled torque distribution on the driven front axle generates a yaw moment that steers the vehicle to the desired trajectory. The necessary information for this function is provided by cameras that detect the lane markings and by the vehicle observer that allocates the current vehicle dynamic state.
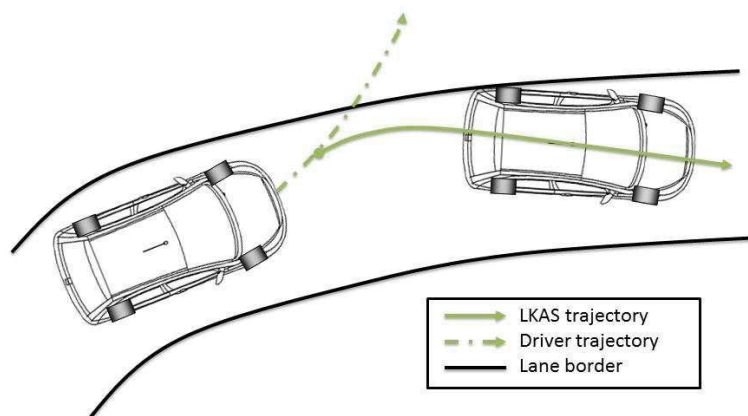

Figure 2.18: LKAS principle

The basic idea of LKAS is to compute the steering angle that is necessary to keep the vehicle on the desired trajectory. This strategy can be decomposed in three steps:

1. Computation of the required yaw rate r_R from the predicted Y_p and the desired Y_d lateral displacement:
   Using Taylor's second order expansion and supposing that the side slip angle is negligible, it can be found that [17]:

$$r_R = -\frac{2v}{L_s^2}(Y_d - Y_p),$$ (2.32)

   where L_s is the length of the prediction horizon.

2. Calculation of the steering angle that is required to reach the requested yaw rate:
   This is realized by an inverse transfer function of a vehicle dynamic model. Here, a linear two-Degree of Freedom (DoF) and a two-wheel model is used.

3. Computation of the predicted lateral deviation from the target line:
   The predicted lateral displacement Y_p is deduced from the real lateral displacement Y_r and from the relative yaw angle r_r:

$$Y_p = Y_r + L_s \cdot r_r,$$ (2.33)

   where this prediction takes the road curvature into account as well.

Moreover, the control strategy has to be a well configured transition logic that switches between the driver and the LKAS control of the steering. The algorithm is activated when the driver is identified as inattentive and the vehicle is moving towards a lane border. Thus, the function will not be activated if the driver wants to change the lane. The driver attention is monitored by analysing the steering torque and the direction indicators. The transition is realized in a state machine. Additionally, the handling of error flags and the adherence of functional and dynamic limits are realized in the function as well to avoid unintended vehicle steering.

2.3 Driver model

The driver model was designed for an automated function validation of defined test scenarios in changing environmental conditions. Here, the focus lies more on the repeatability of the scenarios than on getting a high realistic human driving behaviour. Moreover, there exist many approaches to model different driver types (sporty, aggressive, smooth,...) which can be found in literature, e.g. in [47] or [11]. In the vehicle model presented here only one driver type (normal) was used.
The driver model (see Fig. 2.19) receives information of the current vehicle state and the environment. Then, the relative position of the vehicle in its environment is computed. A simple state-space-controller calculates the optimum steering angle to keep the vehicle in the lane with the information of the relative yaw angle and the lateral deviation to
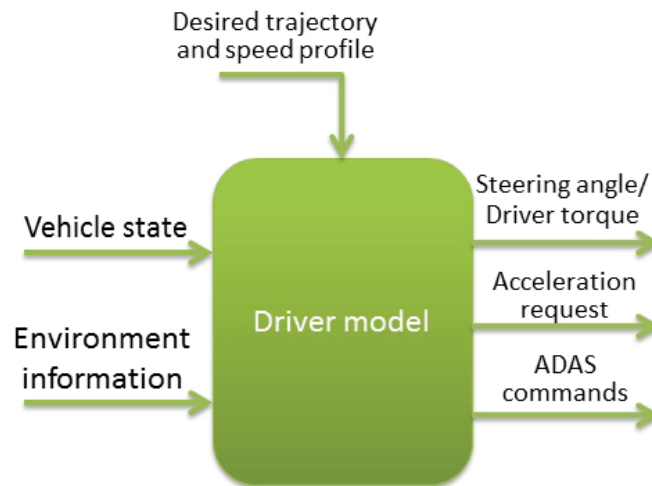
Figure 2.19: Top-level view of driver model

the middle of the lane. The relative yaw angle is the angle between the vehicle yaw angle and the yaw angle of the road. In that way curvature is compensated in this control. The longitudinal control, i.e. the acting on brake and accelerator pedal, is designed by a Proportional-Integral-Derivative (PID) control. Here, the control input is computed by subtraction of the wished velocity from the current vehicle speed. The desired speed can be given as fixed value or as speed profile. In addition to the dynamic control of the driver there are many options to control set parameter of the equipped ADAS, change the car key position, plug a charge cord and set the gear number.

2.3.1 Driving scenarios

For the function validation a set of different driving scenarios was implemented according to published norms. Here, the steering and accelerator behaviour of the driver was designed for these standardized tests. The tests are straight line driving, constant radius turning, brake in bend, step steer, lift off oversteer, sine with dwell, and reverse driving. A short description for each test is given in the following subsections. In general, all scenarios were simulated for different road friction coefficients and varying initial speeds.

Straight line driving

In the straight line driving scenarios the steering angle is constantly at zero and the acceleration request is either positive, to achieve a desired vehicle speed, or negative in order to break until vehicle standstill. In both cases the respective pedal is pressed to its maximum to achieve the highest acceleration rates and to ensure the TCS and, accordingly, the ABS activation.

Straight line acceleration tests are mostly performed to measure the time the vehicle

needs to accelerate from standstill to a certain speed. However, the time to accelerate to a speed of $100\,kph$ is the most common value and adducted to compare the acceleration potential of different cars. For this work it was very helpful to model high tyre slip during this acceleration period when TCS was deactivated. A more detailed explanation will be given in the next chapter.

The straight line braking scenario was built-up according to [1]. From a given initial speed the vehicle performs a strong deceleration until standstill. By that the stopping distance can be measured which is an important value for the vehicle performance and active vehicle safety. The vehicle observer performance could be improved significantly, in particular when ABS was deactivated and tyre blocking occured.

Constant radius driving

In the constant radius driving scenario the dynamic behaviour, especially the lateral, of a vehicle should be analysed. In [2] three different methods are presented: Constant radius, constant steering-wheel and constant speed. As the first method is the easiest to arrange since no extra calculations for analysis are necessary, this one was chosen for simulation. Moreover, the driver model is suitable for this method as well as due to the lane keeping algorithm included. The driver is modelled to follow a given radius at a constant speed. The tests were simulated for different radii, speeds and road-friction coefficients. Furthermore, both driving directions, clockwise and anti-clockwise, were simulated. The initial velocity of the vehicle was set to the respective desired speed.

Bend driving

The bend driving tests are used to analyse the vehicle behaviour when sudden acceleration or deceleration occurs. The execution for sudden acceleration and brake in a bend was done according to [3]. Just as for the constant radius driving the simulation runs were done for both driving directions. The basic requirement for the sudden acceleration change is a steady state circular driving condition. When this requirement is fulfilled the step on the accelerator pedal and brake pedal respective virtually to their maximum is executed, the steering angle is held constant and the gear is switched to neutral. Again the scenario was simulated for varying initial and desired speeds, radii and road friction.

Lift-off oversteer

The intention of the lift-off oversteer scenario is to determine the effect of sudden occurrence of a lift-off condition on course holding and directional behaviour of a vehicle operating a steady-state circular motion. In general, a lift-off means that when the vehicle is in gear and the accelerator pedal is fully released very quickly [5].

The scenario may be performed in two methods. In this case it was simulated in constant radius tests. When the vehicle establishes a steady-state condition the steering angle is fixed, the accelerator pedal is released as quick as possible and the gear remains in its position. Like in the previous scenarios the simulation was repeated under varying environmental conditions, initial speeds and radius.

Step Steer

The step steer scenario is used to determine the lateral vehicle dynamics. In contrast to the previous scenarios this one is an open-loop manoeuvre which has no realistic driving conditions but is suitable to test the vehicle dynamics.
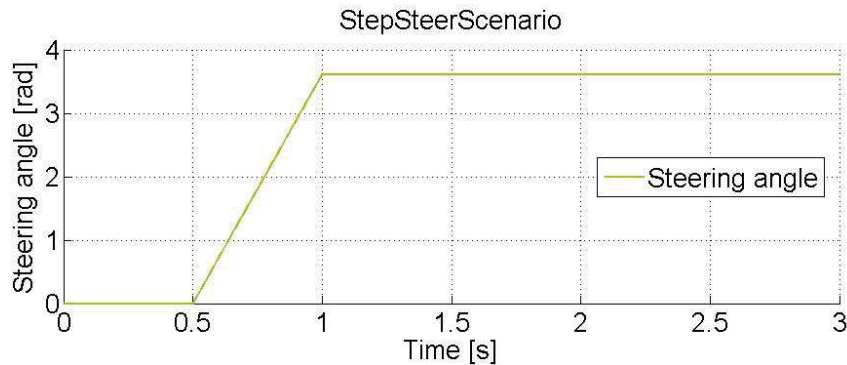

Figure 2.20: Steering angle in step steer scenario

According to [4] the initial speed is set to $80\,kph$ and the steering angle is in zero position. Starting with an almost zero yaw rate the steering angle has to be turned to a defined value, here $3.6128\,rad$ as quick as possible and kept constant until the measured vehicle states are steady-state (see Fig. 2.20). During the steering movement the gear is switched to neutral so that no longitudinal effects occur. The simulations were repeated for speed steps of $20\,kph$ and different road conditions.

Sine with dwell

The sine with dwell scenario was developed by the Alliance of Automobile Manufactors and the National Highway Traffic Safety Administration (NHTSA) to provide data that is used to objectively compare vehicle performance [22].
The steering angle in this scenario is basically a sine with identical amplitudes except for the break of $500\,ms$ when the minimum was reached. For the sinusoidal frequencies of $0.5\,Hz$ or $0.7\,Hz$ are used. In Fig. 2.21 the example of a sine with dwell steering for an amplitude of $3.6128\,rad$ and a frequency of $0.7\,Hz$ is shown.
The simulation of this scenario was executed for different speeds, steering amplitudes, frequencies and road adhesions.

Reverse driving

The scenario of reverse driving was integrated to cover both driving directions and to avoid sign failures during the development phase. In contrast to the other scenarios the focus is not on the evaluation of vehicle dynamics. Slow speed reverse driving with and without steering movement was simulated which is likely to occur in realistic driving situations.
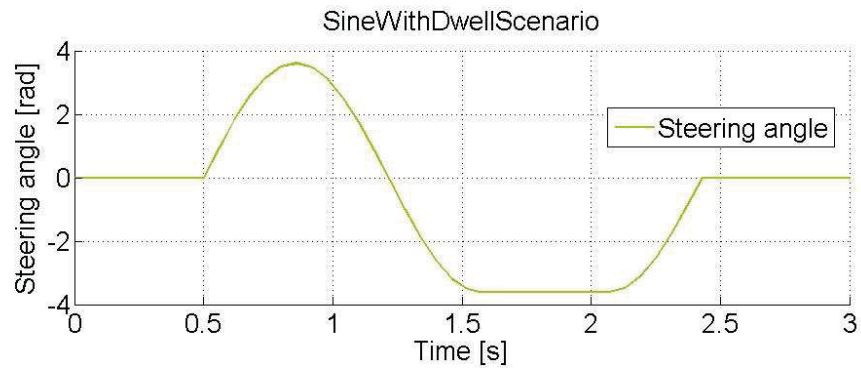
Figure 2.21: Steering angle in sine with dwell scenario

In this case the calculation of the vehicle speed within the vehicle observer had to be extended. This will be explained in the next chapter.

3 Vehicle Observer

The term 'observation' is seen as capture of the vehicle and the environment by sensors. In general, the result of a measurement is a measurement vector which exists out of the detected measurement attributes and a measurement time which is relevant for the estimation of a dynamic processes. An observation reduces the real world to the attributes detected by the sensors.

ADAS need reliable and accurate information of the current vehicle state and the environment for an optimal and safe control of the vehicle actuators. The vehicle observer's task is to determine the required vehicle states and changing environmental parameters as precisely as possible even if some are not measured by sensors directly.

An overview of filter concepts, a detailed survey of Kalman filters and the evaluation for the best concept in this vehicle application are given in the next section. Afterwards, the top-level structure of the vehicle observer, the data flow and signal definition are presented. In section 3.3 the plausibility check with the detection and correction mechanisms in the basic version is explained. The subsystem EKF, which implies the general EKF concept for observation of the vehicle states, and the necessary computation are introduced in section 3.4. Here, the used vehicle and tyre models are shown and the proof of observability of the complete vehicle state observer is given. Section 3.5 elaborates on the issue of the estimation of variable vehicle and environmental parameters. The approach for each of the estimated parameters is specified there. The stability assessment subsystem, which computes the dynamic stability limits of the vehicle based on the estimated states and parameters, is presented in section 3.6. Finally, in section 3.7, the calculation of the driven distance of the vehicle is described .

3.1 Filter and estimation concepts

There are several filter concepts which are compatible with this challenge to smooth measured sensor signals and to estimate unmeasured vehicle states. In Tab. 3.1 filter concepts of the category g-h-filters are listed which determine the desired values by a recursive method. With the help of the coefficients g and h a quantification between the current measurement and the last estimated value is realised. They differ in the method by evaluating these coefficients the one which may be constant over all iteration steps or may vary with every iteration step. [15]

Statistical methods handle the system state as a random variable which is symbolised through a conditional probability density. This conditional probability density represents the information that is gathered from the measurement values on which it is based as well. The realisation of the measurement values affects the form of the density function.

	Concept
1	Wiener filter
2	Fading-memory polynomial filter
3	Expanding-memory polynomial filter
4	Kalman filter
5	Bayes filter
6	Least-squares filter
7	Benedict-Bordner filter
8	Lumped filter
9	Discounted least squares g-h-filter
10	Critically damped g-h-filter
11	Growing memory filter

Table 3.1: g-h-filter concepts according to [15]

On the basis of this density function three different optimal estimation values are defined which are shown in Fig. 3.1.:

- Conditional mode - maximum of the density function

- Conditional median - symmetry of area

- Conditional mean - CoG of the density function

If the observed system should consider the dynamical behaviour of the observed object as well, a suitable model has to be regarded for the estimation. The observation of dynamic systems is outlined in the following section.
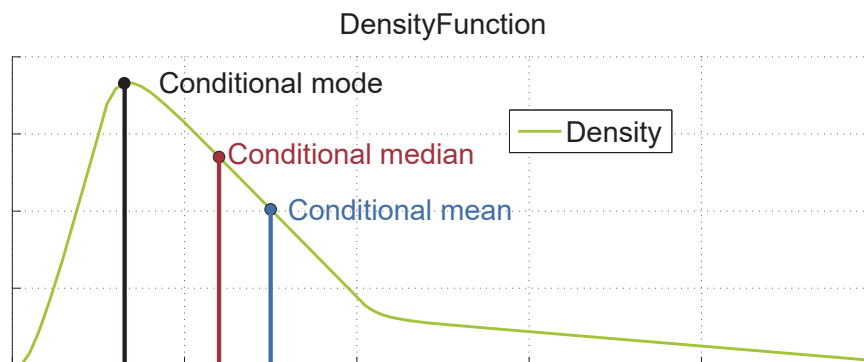

Figure 3.1: Different estimation values for a density function

3.1.1 Linear stochastic systems

The state vector of the observed object contains dynamic states, e.g. the acceleration and the yaw rate. For an accurate and reliable observation, a model that takes into account the dynamic movement is necessary. The following statement and annotations are based on [9] and [28].

The motion of an object can be described by a dynamic equation from a continuous linear stochastic system:

$$\dot{x}(t) = F(t)x(t) + C(t)u(t) + w(t), \tag{3.1}$$

where x is the system state vector, u the control input vector, w the zero-mean uncorrelated process noise vector, F the dynamic system matrix, C the coupling input matrix and G the process noise coupling matrix.

The measurement equation is equal to:

$$y(t) = H(t)x(t) + D(t)u(t) + v(t), \tag{3.2}$$

with the measurement vector y, the measurement sensitivity matrix H, the output coupling matrix D and the measurement noise vector v. The dimensions of the vectors and matrices in Equation 3.1 and 3.2 depend on the system model that should be described with the dimension of system states n and the dimension of measurement states ℓ that shall be observed (see Tab. 3.2).

Symbol	Dimensions	Symbol	Dimensions
x, w, C	$n \times 1$	F	$n \times n$
y, v, D	$\ell \times 1$	H	$l \times n$
		Δ, δ	scalar

Table 3.2: Dimensions of vectors and matrices in linear models

Without the process noise w and measurement noise v the system would be a deterministic one. In stochastic systems both noise terms are assumed to be white noise, meaning zero mean and finite variance, and as independent stochastic processes.

In general, applications for the observation of dynamic objects are not able to work in continuous mode but with fixed time steps, thus, discrete-time. This is also valid for most automotive applications. In this work, the target hardware, the VHU, runs with a quasi-fixed sample time. In discrete systems the assumption is made, that the control input vector in equation 3.1 is constant for a certain time.

The dynamic model for a discrete linear stochastic system in a Random Sequence (RS) with initial conditions is then set up as follows:

$$x_k = \Phi_{k-1}x_{k-1} + \Gamma_{k-1}u_{k-1} + G_{k-1}w_{k-1}, \tag{3.3}$$

where x_{k-1} is the system state vector at time t_{k-1}, x_k is its value at time $t_k > t_{k-1}$, Φ_{k-1} is the state transition matrix for the system at time t_k, u_k is the input vector to

the system at time t_k and Γ_k the corresponding input coupling matrix.
The measurement equation in discrete time is equal to:

$$z_k = H_k x_k + D_k u_k + v_k, \tag{3.4}$$

The process noise is assumed to be white and zero-mean uncorrelated, so that the following equation holds with the covariance Q and the Kronecker delta function Δ:

$$E\left[w_k\right] = 0, \tag{3.5}$$

$$E\left[w_{k1} w_{k2}^T\right] = Q_{k_1} \Delta(k_2 - k_1). \tag{3.6}$$

Accordingly, the measurement noise is supposed to be white and zero-mean uncorrelated with the covariance R:

$$E\left[v_k\right] = 0, \tag{3.7}$$

$$E\left[v_{k1} v_{k2}^T\right] = R_{k_1} \Delta(k_2 - k_1). \tag{3.8}$$

Moreover, the noise sequences w_k and v_k are assumed to be uncorrelated to each other:

$$E\left[w_{k_1} v_{k_2}^T\right] = 0 \text{ for random } k. \tag{3.9}$$

As the system can be described by the last state completely it is called a Markov sequence.
The matrices Φ, Γ, G, H and D are supposed to be known and may vary with time. The scope tends towards the conditional expected value of the system state $\hat{x}(j|k)$ at the time j

$$\hat{x}(j|k) \equiv E\left[x(j)|Z^k\right], \tag{3.10}$$

with the condition that

$$Z_k \equiv \{z(j)\}_{j=1}^k \tag{3.11}$$

notates the measurement values at an arbitrary time k. A distinction is made between

1. the system state estimation (for $j = k$),

2. the smoothed system state (for $j < k$),

3. the predicted system state (for $j > k$).

The estimation error is defined as:

$$\tilde{x}_k \equiv x_{k-1} - \hat{x}_k \tag{3.12}$$

The conditional covariance matrix of the current system state is then:

$$\begin{aligned}
P_k &\equiv E\left[\left[x_{k-1} - \hat{x}_k\right]\left[x_{k-1} - \hat{x}_k\right]^T | z^k\right] \\
&= E\left[\tilde{x}_k \tilde{x}_k^T | z^k\right]
\end{aligned} \tag{3.13}$$

3.1.2 Kalman filter

A Kalman filter in general is an estimator for linear-quadratic problems, which is given in estimating the instantaneous state of a linear dynamic system which is perturbed by white noise. The estimator provides the statically optimal result with respect to any quadratic function of the estimation error.

The Kalman filter is a set of mathematical equations that were named after its developer Rudolf E. Kalman. A special feature of the 1960 released filter concept is the special mathematical structure which facilitates the use in real-time applications in different technical areas. Mostly it is used for the control of complex dynamic systems such as continuous manufacturing processes, aircraft, ships, spacecraft and of course in the automotive sector.

Basically, the Kalman filter has a recursive algorithm to compute the optimal estimation value which considers all available measurement values up to the current time. If the density function is normally distributed for the state as well as for the measurement values, the state density function, which bases on the measurement values, is not normally distributed as well and the optimal estimation values coincide like shown in Fig. 3.1.

In the next sections the theory of standard Kalman filter, which is suitable for linear systems, the extended and unscented Kalman filter, which are designed for non-linear systems, will be introduced.

In general, Kalman filter algorithms are separated in two main computation steps: the prediction step and the correction step. Results of the prediction step are marked with $(-)$ and results of the correction step are labelled with $(+)$. In the prediction step the predicted state, based on the input vector and the system model, and the predicted state estimate covariance are computed. Afterwards, among other operations, the optimal Kalman gain $\bar{K}_k$ is calculated and the state estimation and the estimated covariance are updated in the correction steps. The estimate covariance is used in the next time step for the prediction computation again.

Standard Kalman-Filter

The algorithm of the Standard Kalman-Filter (SKF), which is known as linear Kalman filter as well, starts with the initial values of the state $E(x_0) = \hat{x}_0$ and the covariance $E(\tilde{x}_o \tilde{x}_o^T) = P_0$, so that the n_x dimensions of the normal distribution are completely described. The estimation of the predicted state $\hat{x}_k(-)$ at the time k with covariance $P_{k-1}(+)$ is done by updating with a new measurement, z_k, as follows:

1. **Prediction step**
   The priori estimate $\hat{x}_k(-)$ of x_k will be determined with the current state estimate $\hat{x}_{k-1}(+)$, the state transition matrix, the control input vector and the input coupling matrix:

   $$\hat{x}_k(-) = \Phi_{k-1}\hat{x}_{k-1}(+) + \Gamma_{k-1}u_{k-1} \qquad (3.14)$$

   The priori covariance matrix $P_k(-)$ is computed by the use of the posteriori covariance $P_{k-1}(+)$, the state transition matrix and the covariance matrix of the process

noise:

$$P_k(-) = \Phi_{k-1} P_{k-1}(+) \Phi_{k-1}^T + Q_{k-1} \tag{3.15}$$

2. **Correction step**
   Computing the optimal Kalman gain $\bar{K}_k$ using the priori covariance, the sensitivity matrix and the covariance matrix of the measurement noise:

$$\bar{K}_k = P_k(-) H_k^T \left[H_k P_k(-) H_k^T + R_k \right]^{-1} \tag{3.16}$$

Update the covariance matrix to get the posterior covariance matrix $P_k(+)$ with the identity matrix I, the Kalman gain and the sensitivity matrix:

$$P_k(+) = \left[I - \bar{K}_k H_k \right] P_k(-) \tag{3.17}$$

Finally, compute the successive values of $\hat{x}_k(+)$, recursively using the calculated results of $\bar{K}_k$, the given initial estimated states $\hat{x}_0$ and the measurement input data z_k:

$$\hat{x}_k(+) = \hat{x}_k(-) + \bar{K}_k \left[z_k - H_k \hat{x}_k(-) \right] \tag{3.18}$$

For a correct functionality of the SKF certain postulations have to be fulfilled. The initial estimation state $\hat{x}_0$ and the covariance P_0 have to be known as well as the state transition matrix and the sensitivity matrix. Moreover, the process and measurement noise are assumed to be zero mean Gaussian white noise and known:

$$E\left[w_k \right] = 0, \tag{3.19}$$
$$E\left[w_{k1} w_{k2}^T \right] = Q(k) \Delta(k_2 - k_1), \tag{3.20}$$
$$E\left[v_k \right] = 0 \tag{3.21}$$
$$E\left[v_{k1} v_{k2}^T \right] = R(k) \Delta(k_2 - k_1). \tag{3.22}$$

In addition, there are no correlations between the noise signals and the initial state x_0:

$$E\left[x_0 w_k^T \right] = 0, \tag{3.23}$$
$$E\left[x_0 v_k^T \right] = 0, \tag{3.24}$$
$$E\left[v_j w_k^T \right] = 0. \tag{3.25}$$

During the computation of the priori and the posterior covariance matrix it should be checked for symmetry and positive definiteness. Here, any failure indicates to either a software error or an ill-conditioned problem.
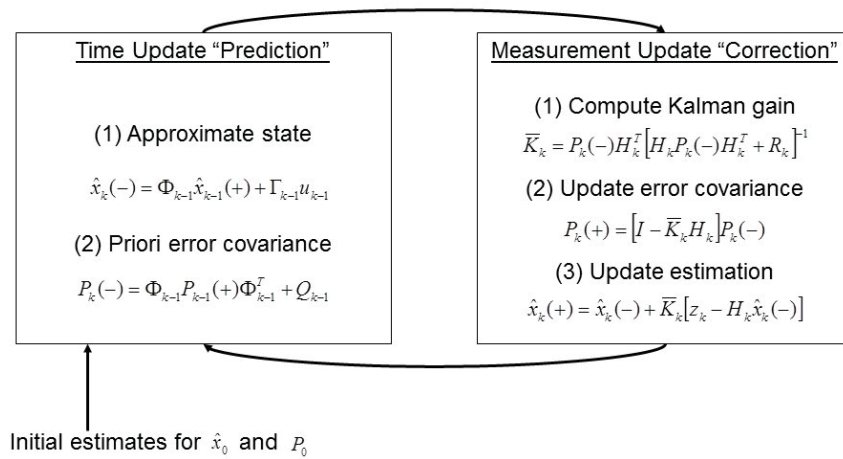The overview of the SKF algorithm is shown in Fig. 3.2.

Figure 3.2: Standard Kalman filter algorithm

Linearisation methods

The SKF for discrete and continuous systems was deduced in the previous section and the resulting optimal estimator is simple in form and powerful in effect. The combination of linear functions, quadratic performance criteria, in detail the minimization of the quadratic norm of the estimation error, and Gaussian statistics is essential for the development of this estimator.

But as many dynamic systems and sensors have no complete linear behaviour, but one that is not too far away from it, extensions for such non-linear problems have to be applied. Different techniques for the linearisation of the non-linear functions around the current system state were designed to fit the equations into the Kalman filter concept. These techniques are applicable if f and h are twice-continuously differentiable only. Basically, the linearisation around a nominal trajectory and the linearisation about the estimated trajectory are two techniques to solve this problem and will be explained roughly now.

Linearisation about the nominal trajectory   A nominal trajectory refers to the trajectory which is obtained when the random variates assume their expected values. But the nominal trajectory will have small deviation to the real trajectory due to unknown influences on the plant like in most dynamic systems. These influences are, for example, the initial system state x_0, the process noise w_k and the measurement noise v_k. If the non-linear function f is differentiable infinitely often, the small deviations to the real trajectory can be represented by a Taylor series expansion about the nominal trajectory. The magnitudes of the deviations are determined by the variances of the variates involved. The approximation is acceptable when terms beyond some order may be ignored if these deviations are relatively small compared to the higher order coefficients of the expansion. These magnitudes, however, have to be evaluated before making such

an assumption.

The symbol ϑ denotes the deviations from the nominal,

$$\vartheta x_k = x_k - x_k^{nom}, \tag{3.26}$$

$$\vartheta z_k = z_k - h(x_k^{nom}, k). \tag{3.27}$$

If the high order terms can be neglected the Taylor series expansion of $f(x, k-1)$ with respect to x at $x = x_{k-1}^{nom}$ in discrete form is:

$$
\begin{aligned}
x_k &= f(x_{k-1}, k-1) \\
&= f(x_{k-1})^{nom}, k-1) + \left.\frac{\partial f(x, k-1)}{\partial x}\right|_{x=x_{k-1}^{nom}} \vartheta x_{k-1} \\
&= x_k^{nom} + \left.\frac{\partial f(x, k-1)}{\partial x}\right|_{x=x_{k-1}^{nom}} \vartheta x_{k-1}
\end{aligned}
\tag{3.28}
$$

or

$$
\begin{aligned}
\vartheta x_k &= x_k - x_k^{nom} \\
&= \left.\frac{\partial f(x, k-1)}{\partial x}\right|_{x=x_{k-1}^{nom}} \vartheta x_{k-1}
\end{aligned}
\tag{3.29}
$$

Simplified, when the high order terms are neglected, the deviation is approximated with:

$$\vartheta x_k \approx \Phi_{k-1}^{[1]} \vartheta x_{k-1} + w_{k-1}, \tag{3.30}$$

where the first order approximation coefficients are given by a $n \times n$ constant matrix:

$$
\begin{aligned}
\Phi_{k-1}^{[1]} &= \left.\frac{\partial f(x, k-1)}{\partial x}\right|_{x=x_{k-1}^{nom}} \\
&= \left.\begin{bmatrix}
\frac{\partial f_1}{\partial x_1} & \frac{\partial f_1}{\partial x_2} & \frac{\partial f_1}{\partial x_3} & \cdots & \frac{\partial f_1}{\partial x_n} \\
\frac{\partial f_2}{\partial x_1} & \frac{\partial f_2}{\partial x_2} & \frac{\partial f_2}{\partial x_3} & \cdots & \frac{\partial f_2}{\partial x_n} \\
\frac{\partial f_3}{\partial x_1} & \frac{\partial f_3}{\partial x_2} & \frac{\partial f_3}{\partial x_3} & \cdots & \frac{\partial f_3}{\partial x_n} \\
\vdots & \vdots & \vdots & \ddots & \vdots \\
\frac{\partial f_n}{\partial x_1} & \frac{\partial f_n}{\partial x_2} & \frac{\partial f_n}{\partial x_3} & \cdots & \frac{\partial f_n}{\partial x_n}
\end{bmatrix}\right|_{x=x_{k-1}^{nom}}
\end{aligned}
\tag{3.31}
$$

Analogous to the non-linear transfer function the non-linear measurement transfer function h can be represented by a Taylor series when it is sufficiently differentiable and the

assumption is made that the high order terms can be neglected:

$$h(x_k, k) = h(x_k^{nom}, k) + \left.\frac{\partial h(x, k)}{\partial x}\right|_{x = x_k^{nom}} \vartheta x_k \tag{3.32}$$

or

$$\vartheta z_k = \left.\frac{\partial h(x, k)}{\partial x}\right|_{x = x_k^{nom}} \vartheta x_k. \tag{3.33}$$

The alternative representation to the equations 3.32 and 3.33 for the deviations in the measurement is given by:

$$\vartheta z_k = H_k^{[1]} \vartheta x_k, \tag{3.34}$$

where the first-order variational term is

$$
\begin{aligned}
H_k^{[1]} =& \left.\frac{\partial h(x, k)}{\partial x}\right|_{x = x_k^{nom}} \\[2mm]
=& \left.\begin{bmatrix}
\frac{\partial h_1}{\partial x_1} & \frac{\partial h_1}{\partial x_2} & \frac{\partial h_1}{\partial x_3} & \cdots & \frac{\partial h_1}{\partial x_n} \\[1mm]
\frac{\partial h_2}{\partial x_1} & \frac{\partial h_2}{\partial x_2} & \frac{\partial h_2}{\partial x_3} & \cdots & \frac{\partial h_2}{\partial x_n} \\[1mm]
\frac{\partial h_3}{\partial x_1} & \frac{\partial h_3}{\partial x_2} & \frac{\partial h_3}{\partial x_3} & \cdots & \frac{\partial h_3}{\partial x_n} \\[1mm]
\vdots & \vdots & \vdots & \ddots & \vdots \\[1mm]
\frac{\partial h_n}{\partial x_1} & \frac{\partial h_n}{\partial x_2} & \frac{\partial h_n}{\partial x_3} & \cdots & \frac{\partial h_n}{\partial x_n}
\end{bmatrix}\right|_{x = x_k^{nom}}.
\end{aligned}
\tag{3.35}
$$

Linearisation about the estimated trajectory As the linearisation about the nominal trajectory has the problem that the deviation towards the current trajectory increases with time, and, thereby, the significance of higher order terms in the Taylor series expansion increases as well, the method of the linearisation about the estimated trajectory is presented now.

When a system is sufficiently observable, then, the deviations between the current trajectory and the estimated trajectory will remain relatively small, so that the linearisation assumption is valid [27]. By replacing the nominal by the estimated trajectory the increasing deviation problem is solved and the Taylor series expansion can be evaluated.

A clear disadvantage of this method is the tendency towards high computational load in real-time. In contrast to the linearisation about the nominal trajectory, where Φ, H and $\bar{K}_k$ can be computed offline, in the linearisation about the estimated trajectory they have to be computed in real time as function of the priori estimate.

Thus, the only rearrangement in the evaluation of the partial derivatives is to replace the priori nominal state x_{k-1}^{nom} by the estimated state $\hat{x}_{k-1}$ and the current nominal state x_k^{nom} by the actual estimated state $\hat{x}_k$. Thereby, the matrices of the partial derivatives

now become

$$\Phi^{[1]}(\hat{x}, k) = \left. \frac{\partial f(x, k)}{\partial x} \right|_{x = \hat{x}_k(-)}, \tag{3.36}$$

and

$$H^{[1]}(\hat{x}, k) = \left. \frac{\partial h(x, k)}{\partial x} \right|_{x = \hat{x}_k(-)}. \tag{3.37}$$

Extended Kalman-Filter

Here, the first method to cope with Kalman filtering in 'slightly non-linear' problems is the EKF concept. The essential idea of the EKF was proposed by Stanley F. Schmidt and has been called the Kalman-Schmidt filter [10].

In case of a non-linear system the plant and measurement models, based on 3.1 where the entries C and G are equal to one and there is no direct influence of the input u on the output z, for a discrete stochastic system are presented by:

$$x_k = f(x_{k-1}, k-1) + u_k + w_{k-1}, \tag{3.38}$$
$$z_k = h(x_k, k) + v_k. \tag{3.39}$$

where f describes the non-linear transfer function for the system state and h is the non-linear measurement transfer function.

Analogous to the SKF the EKF algorithm can be separated into a prediction and a correction step:

1. **Prediction step**
   Computing the predicted state estimate with the non-linear equations

   $$\hat{x}_k(-) = f_{k-1}(\hat{x}_{k-1}(+)) + u_k, \tag{3.40}$$

   and the priori error covariance matrix

   $$P_k(-) = \Phi^{[1]}_{k-1} P_{k-1}(+) \Phi^{[1]T}_{k-1} + Q_{k-1}$$
   $$\text{with} \ \ \Phi^{[1]}_{k-1} \approx \left. \frac{\partial f}{\partial x} \right|_{x = \hat{x}_k(-)}. \tag{3.41}$$

2. **Correction step**
   Calculation of the optimal Kalman gain

   $$\bar{K}_k = P_k(-) H^{[1]T}_k \left[H^{[1]}_k P_k(-) H^{[1]T}_k + R_k \right]^{-1}$$
   $$\text{with} \ \ H^{[1]}_k \approx \left. \frac{\partial h}{\partial x} \right|_{x = \hat{x}_k(-)}, \tag{3.42}$$

the posterior error covariance matrix

$$P_k(+) = \left[I - \bar{K}_k H_k^{[1]} \right] P_k(-),$$
(3.43)

and the predicted estimate on the measurement

$$\hat{x}_k(+) = \hat{x}_k(-) + \bar{K}_k(z_k - H_k^{[1]} \hat{x}_k(-)).$$
(3.44)

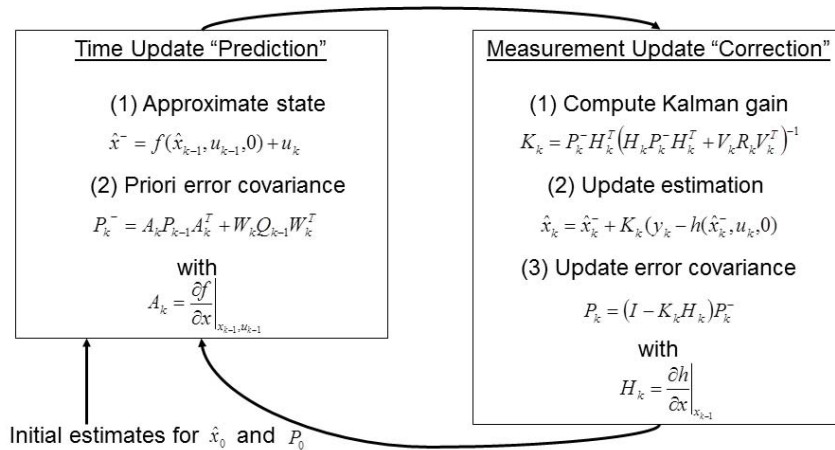In Fig. 3.3 an overview of the EKF algorithm is given.

Figure 3.3: Extended Kalman filter algorithm

Unscented Kalman-Filter

Another method that is used to estimate non-linear systems is the Unscented Kalman-Filter (UKF) which was introduced by Julier and Uhlmann in 1997 [38]. The concept promises performance like the EKF for non-linear systems and almost the same computational effort.

It uses the principle in which a set of discretely sampled points can be used to parametrise mean and covariance. Therefore, the linearisation of the non-linear system is replaced by a deterministic approach - the unscented transformation. Here, the state distribution is approximated again by the use of a Gaussian Random Variable (GRV) but is represented by a set of chosen sample points - the sigma points. This set of sigma points completely covers the true mean and covariance of the GRV, and when applied to a non-linear system, captures the posterior mean and covariance exactly to the 3rd order of the Taylor series expansion for any non-linearity. What is noteworthy here, is that the computational effort of this method can be compared to the one of the EKF algorithm where the linearisation steps are quite complex.

The Unscented Transformation (UT) is a method for calculating the statistics of a ran-

dom variable which undergoes a non-linear transformation [38]. Let x be a random variable with the dimension L that is propagated through a non-linear function $y = g(x)$. The mean $\bar{x}$ and the covariance P_x of x are assumed to be known. To compute the statistics of y a matrix X of $2L + 1$ sigma vectors X_i is formed with the following equations:

$$\begin{aligned}
X_0 &= \bar{x} \\
X_i &= \bar{x} + \left(\sqrt{(L + \kappa)P_x} \right)_i \quad \text{i} = 1, \ldots, \text{L} \\
X_i &= \bar{x} - \left(\sqrt{(L + \kappa)P_x} \right)_{i-L} \quad \text{i} = \text{L} + 1, \ldots, 2\text{L},
\end{aligned} \tag{3.45}$$

where κ is a scaling parameter for the distribution of the sigma points around $\bar{x}$. In case of a Gaussian distribution the condition $\kappa = 3 - L$ has to be fulfilled. The term $\left(\sqrt{(L + \kappa)P_x} \right)_i$ represents the ith row of the covariance matrix. This set of sigma points is now transformed with the non-linear function

$$Y_i = g(X_i) \, i = 0, \cdots, 2L, \tag{3.46}$$

the mean and covariance for y are approximated using a weighted sample mean and covariance of the posterior sigma points,

$$\hat{y} \approx \sum_{i=0}^{2L} w_i^{(m)} Y_i \tag{3.47}$$

$$P_y \approx \sum_{i=0}^{2L} w_i^{(c)} (Y_i - \hat{y})(Y_i - \hat{y})^T, \tag{3.48}$$

and the corresponding weighting factors w_i are given by

$$\begin{aligned}
w_0^{(m)} &= \frac{\kappa}{(L + \kappa)} \\
w_0^{(c)} &= \frac{\kappa}{(L + \kappa)} + (1 - \chi^2 + \zeta) \\
w_i^{(m)} &= w_i^{(c)} = \frac{1}{[2(L + \kappa)]}
\end{aligned} \tag{3.49}$$

where χ and ζ are scaling parameters which have influence on the spreading of the sigma points around the mean state $\hat{x}$. Usually, the χ is set to a very small positive value and ζ is set to zero.

A simple example for a two-dimensional system is shown in Fig. 3.4: the left plot shows the true mean and covariance propagation using the Monte-Carlo sampling; the centre plots show the results using a linearisation approach like it is realised in the EKF; the right plots show the performance of the UT (note only five sigma points are required). By this, the superior performance of the UT becomes clear.

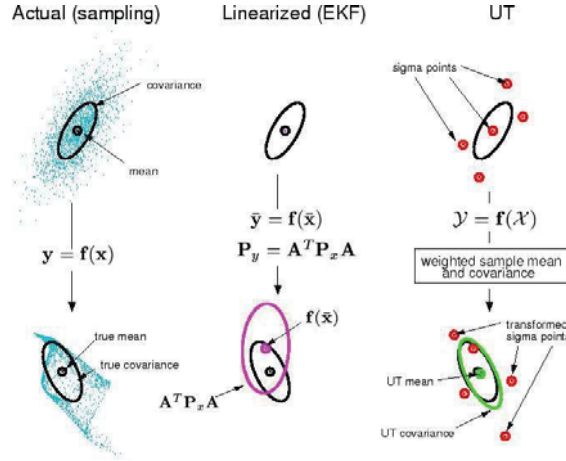The UKF algorithm is a straightforward extension of the unscented transmission to

Figure 3.4: Example of the Unscented transformation

recursive estimation of non-linear systems. Again, the algorithm for discrete systems can be represented by the prediction and correction steps with the initial conditions $\hat{x}_0 = E[x_0]$ and $P_0 = E\left[(x_0 - \hat{x}_0)(x_0 - \hat{x}_0)^T\right]$

1. **Prediction step**
   Compute the set of sigma points with

$$X_{k-1} = \begin{bmatrix} \hat{x}_{k-1} & \hat{x}_{k-1} + \sqrt{(L+\kappa)P_{k-1}} & \hat{x}_{k-1}\sqrt{(L+\kappa)P_{k-1}} \end{bmatrix}, \qquad (3.50)$$

for $k \in [1, \cdots, \infty]$. The priori mean and covariance are calculated by

$$X_i = f(X_{k-1}) \qquad (3.51)$$

$$x_k(-) = \sum_{i_0}^{2L} w_i^{(m)} X_i \qquad (3.52)$$

$$P_k(-) = \sum_{i_0}^{2L} w_i^{(c)} (X_i - \hat{x}_k(-))(X_i - \hat{x}_k(-))^T + Q_k \qquad (3.53)$$

2. **Correction step**

55

Computation of the measurement estimation and the covariances

$$\hat{y}_k(-) = \sum_{i_0}^{2L} w_i^{(m)} h(X_i) \tag{3.54}$$

$$P_{\tilde{y}_k \tilde{y}_k} = \sum_{i_0}^{2L} w_i^{(c)} (h(X_i) - \hat{y}_k(-))(h(X_i) - \hat{y}_k(-))^T + R_k \tag{3.55}$$

$$P_{x_k y_k} = \sum_{i_0}^{2L} w_i^{(c)} (X_i - \hat{x}_k(-))(h(X_i) - \hat{y}_k(-))^T, \tag{3.56}$$

and the estimation update equations

$$\hat{x}_k = \hat{x}_k(-) + P_{x_k y_k} P_{\tilde{y}_k \tilde{y}_k}^{-1} (y_k - \hat{y}_k(-)) \tag{3.57}$$

$$P_k = P_k(-) - K P_{\tilde{y}_k \tilde{y}_k} K \tag{3.58}$$

$$\text{with } K = P_{x_k y_k} P_{\tilde{y}_k \tilde{y}_k}^{-1} \tag{3.59}$$

Although the UKF offers improvements in the approximation of non-linear transfer and measurement equations, it is noteworthy that the overall number of computations is almost the same as for the EKF. Moreover, this concept is applicable if the measurement vector has the same dimension for all sets of sigma points only. That condition is not fulfilled in every real system. The overview of the UKF algorithm is given in Fig. 3.5.
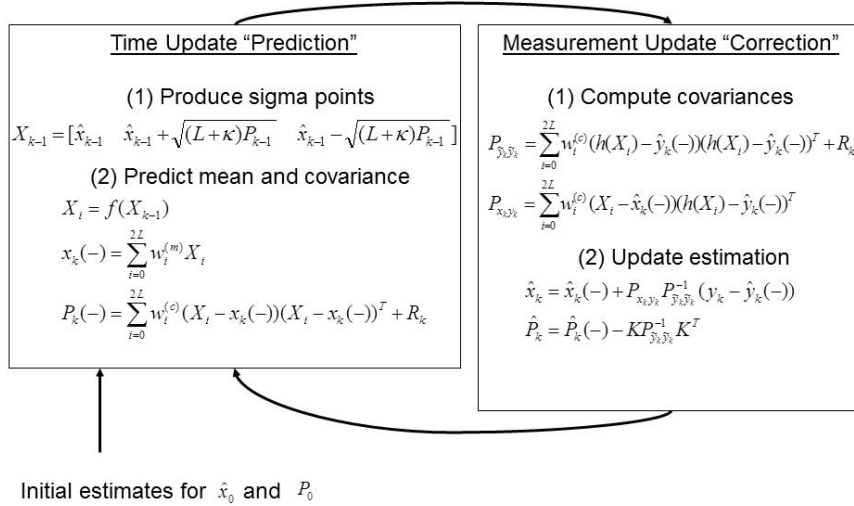
Figure 3.5: Unscented Kalman filter algorithm

As the improvements of the approximations of the non-linear system and measurement equations are obvious, the complexity of the complete concept has to be compared to the one of the EKF. Here, the effort for the choice of sigma points affects the overall computational load since they have to be calculated for the system and measurement equation. For a measurement function which is highly non-linear, and their linearisation is evaluated symbolic, the UKF algorithm has a significant higher execution time.

Recent publications try to minimise the effects of linearisation that come with trigonometric and exponential functions [37] or try to optimise the scaling of the sigma points [39].

As an application example for the UKF [66] estimates vehicle states from the inertial sensor, the odometry and the Differential Global Positioning System (DGPS). Here, simulations show an improved performance compared to the EKF but no verification with real sensor data is given.

3.1.3 Evaluation of most proper Kalman-filter

After the three different Kalman filter concepts - SKF, EKF and UKF - were presented, now, an evaluation of the most proper concept for the estimation of vehicle states has to be figured out. Accuracy and computational complexity of these concepts should be analysed in detail in order to choose the optimal approach for the implementation on the VHU. Therefore, a simple single track model and a discrete filter for each approach was built and tests for different driving manoeuvres were simulated. The discrete form of the filter is chosen because of the target hardware which is not real-time applicable. The execution time of the controller was estimated to $T_S = 10ms$.

The well-known single track model (STM), also referred to as bicycle model, is the easiest and most common model to describe the vehicle dynamics [46] [7]. It was designed by Riekert and Schunck in 1940 basically for the analysis of steering and distortion behaviour during strong side wind effects [56]. Today, it is mainly used in the early development phase of lateral vehicle controllers and for the detection of driver commands, like in the ESC. The model concentrates both wheels on front and rear axle to one wheel in the centre of the vehicle (see Fig. 3.6).

Under the assumption that the lateral wheel forces are equal for left and right the lateral force generation is linear to the combined tyre slip angle α. For the longitudinal motion a general, longitudinal input force F_x is combined. In general, two variants of the STM are used - a linear and a non-linear version. As the performance of the different Kalman filter variants should be analysed here, the non-liner STM is used. But this model can be linearised for any fixed velocity v_x.

Basically, this non-linear STM has three states. The first one is the longitudinal velocity v_x, second the lateral velocity v_y and the third the yaw rate ψ. The non-linear model is
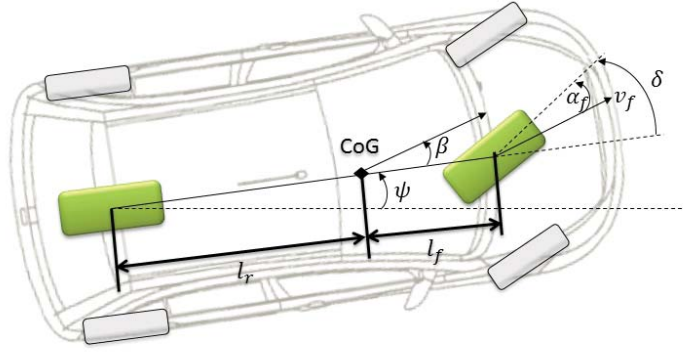
Figure 3.6: Single track model

described by the following equations:

$$\dot{v}_x = v_y r + \frac{1}{m} F_x \tag{3.60}$$

$$\dot{v}_y = -\frac{C_{y,f} + C_{y,r}}{m v_x} v_y + \left(\frac{-l_f C_{y,f} + l_r C_{y,r}}{m v_x} - v_x \right) r + \frac{C_{y,f}}{m} \delta \tag{3.61}$$

$$\dot{r} = \frac{l_r C_{y,r} - l_f C_{y,f}}{I_z v_x} v_y - \frac{l_f^2 C_{y,f} + l_r^2 C_{y,r}}{I_z v_x} r + \frac{l_f C_{y,f}}{I_z} \delta + \frac{1}{I_z} M_z \tag{3.62}$$

The parameters and their values are given in Tab. 3.3. The last term in equation 3.62 is integrated because of the additional yaw moment M_z that is created by the torque distribution of the function TorVec. By that, the analysis of the Kalman filter concepts is close to the real applications even in this early phase of development. The STM is suitable to simulate vehicle motion as long as the tyre forces remain in their linear force generation. So the lateral acceleration should remain under $|4|m/s^2$ and the tyre slip $|\lambda| < 0.15$ and the tyre slip angle $|\alpha| < 0.1$ are assumed to be small.
Note that the second state is exchangeable by the side slip angle β by the relation:

$$\beta = arctan\left(\frac{v_y}{v_x} \right) \tag{3.63}$$

The inputs to each Kalman filter are the steering angle at the front wheels δ, the longitudinal force F_x and the additional moment around the z-axis M_z. To all of these inputs is added white noise with a level that is expected with the real hardware as well. The states that should be estimated are the side slip angle $\hat{\beta}$ and the yaw rate $\hat{r}$. Here, the side slip angle is measurable with extremely expensive sensors in reality only.
The state vector for the Kalman filter has the from $x = [v_x, v_y, r]$, the input vector $u = [F_x, \delta, M_z]$ and the measurement vector $y = [\beta, r]$. For the non-linear transfer function of the system f the equations 3.60-3.62 were used. The non-linear measurement transfer function h was formed to get the desired vehicle states, thus, by the use of 3.63

Symbol	Value	Description
l_f	1.240	Distance from CoG to front axle $[m]$
l_r	1.240	Distance from CoG to rear axle $[m]$
$C_{y,f}$	70000	Cornering stiffness of front axle $[N]$
$C_{y,r}$	84000	Cornering stiffness of rear axle $[N]$
m	1492	Total mass of the vehicle $[kg]$
I_z	1800	Moment of inertia around the z-axis $[kgm^2]$

Table 3.3: Vehicle parameter of the non-linear single track model

and the state r as direct output. The parameter for each concept, system and measurements covariance matrices, spreading of sigma points, were tuned until the results were satisfying. They do not represent the optimum but still are significant enough to compare the outcomes.

The simulation was designed as standalone model for each Kalman filter concept and was executed for different scenarios. To analyse the different concepts, execution time and estimation accuracy were compared.

To analyse the computational effort of the concepts, the model contains as few additional computations to the filter algorithms as possible. Hence, only the distorted signals of the non-linear STM as source and a sink for the estimated state is integrated. The introduced non-linear STM is used as reference model here. The simulations were repeated ten times to exclude influences of other processes of the computer on the execution time. In Fig. 3.7 the estimation results for the lateral deviation from the middle of the lane in a sine with dwell for an initial velocity of $65\,kph$ are shown. Where the estimated state of the EKF concept remains close to the reference signal all the time, the estimated state of the SKF and the UKF concept show great deviation between simulation time $0.8 - 1.6, s$ and a minor deviation for the SKF concept between $2.0 - 3, s$. That is because of the non-linear behaviour of the vehicle and the drawback of this standard concept. Overall the EKF method offers the results with the highest accuracy, particularly in situations with non-linear vehicle motion.

For the analysis of the estimation accuracy, the Normalised Mean Square Error (NMSE) was computed in a post-processing step. This value is computed by:

$$NMSE(x, \hat{x}) = \sum_{i=1}^{k} \frac{|x_k - \hat{x_k}|^2}{|x_k|^2} \tag{3.64}$$

Here, the index i represents the order of the discrete sample time. The results of the complete simulations for each concept are summarized in Tab. 3.4. The advantages of the SKF of the lower computational complexity compared to the other concepts is very obvious. Likewise, the accuracy of the EKF and UKF Kalman filter concept is outstanding in contrast to the classic Kalman filter approach. Moreover, the NMSE of the SKF is not higher since the vehicle dynamics during most of the simulation time remain in
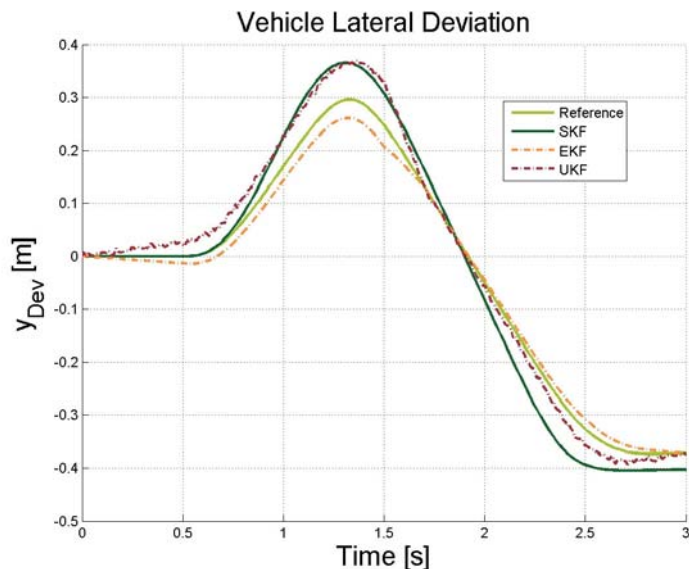
Figure 3.7: Estimation of the lateral deviation

their linear regime in which this concept has a satisfying performance Fig. 3.7. But as in the linear vehicle regime instability is very unlikely and ADAS help to increase the drivers comfort in such situations it is more important to achieve high accuracy of the measured vehicle states during highly non-linear and dynamic vehicle movements from a point of view of passenger safety.

Concept	Average execution time $[s]$	Average NMSE
SKF	4.758	0.087
EKF	7.217	0.004
UKF	7.184	0.012

Table 3.4: Vehicle parameter of the non-linear single track model

Since the high accuracy of the concept has priority, the choice had to be made between the EKF and the UKF concept. As the computational effort for the EKF concept is almost the same as for the UKF concept but the accuracy is three times better, the EKF concept was selected for the further work of designing a vehicle observer for an electric vehicle.

3.2 Vehicle observer structure

After the filtering concepts were presented, three different Kalman filters were analysed in a simple application and the decision was made to work with the EKF concept. Now,

the structure of the complete vehicle observer is presented. Basically, the vehicle observer is composed of five subsystems, see Fig. 3.8, that fulfil different requirements. Here, a rough description of each functionality will be given.
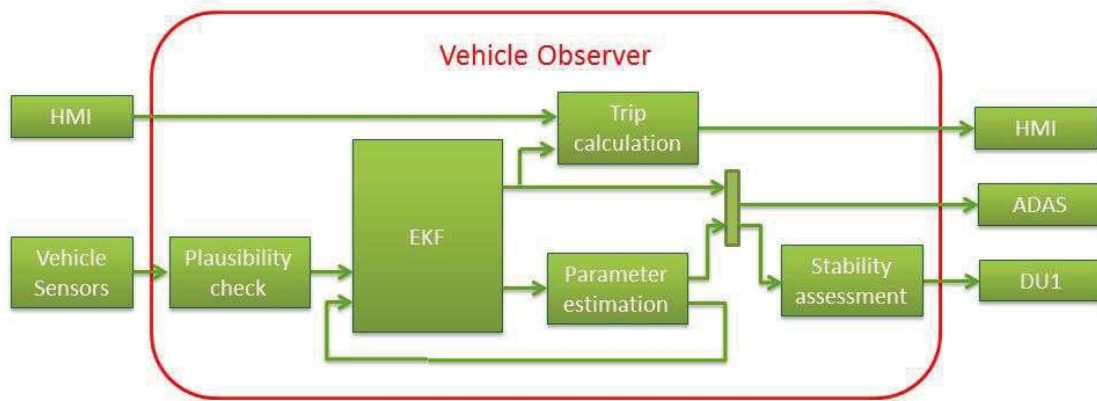
Figure 3.8: Structure with subsystems of the Vehicle Observer

The plausibility check (see section 3.3) is the first receiver of the sensor signals. Here, the analysis of the sensor signals and, if required, the correction of false signals or even the replacement of missing or delayed signals is realized. In addition, a confidence value dependent on the signal checks is computed.

In the EKF-named subsystem the required vehicle states for a safe vehicle control of the ADAS are estimated using a Dugoff Tyre model, a non-linear two-track vehicle model and the EKF algorithm itself (see section 3.4).

The calculation of variable vehicle and environmental parameters is realized in the parameter estimation subsystem. This is realised by use of dynamical equations in driving situations when predefined values hold. The detailed description is given in section 3.5. Afterwards, the computation of stability limits for the current vehicle state and the environmental conditions are presented in section 3.6.

Finally, in section 3.7, the calculation of the driven distance of the vehicle is introduced.

3.2.1 Data Flow and signal definition

In this section the data flow in the top level and the definition of in- and outputs of the vehicle observer shall be explained to provide the reader with an overview.

Data flow

As seen in Fig. 3.8, the incoming sensor signals are analysed in the plausibility check block. If this test block is successfully executed, the signals are transmitted to the EKF block which first calculates the auxiliary quantities of the tyres: slip, side slip and forces.

Subsequently, the EKF algorithm is executed and the vehicle states are computed. With the results from the vehicle state observer the estimation of unknown and variable parameters is done. The estimated parameters are then fed back to the EKF subsystem to update the model equations. By the use of the estimated parameters and the observed vehicle states, the stability limits for the vehicle are evaluated. These limits are sent to the DU1 directly. The trip calculation of the vehicle needs the observed vehicle states and a signal from the HMI which basically is initiated by the driver directly. The computed values are sent to the HMI and displayed in the odometer at the instrument cluster.

Finally, the output of the vehicle observer contains the vehicle states, estimated parameters, the confidence value, stability limits and the driven distance.

Signal definition

Here the in- and outputs of the vehicle observer are specified in detail. The vehicle observer receives the following signals from the equipped sensors:

- Yaw rate r with the longitudinal a_x and lateral acceleration a_y provided, by the yaw rate sensor

- The angular velocities ω_i of the four wheels transmitted by the ABS with their respective status

- Steering angle δ, measured by a steering angle sensor which is mounted on the steering column together with the status, a message count and a checksum

- The angular velocities Ω_i of the two electric machines on the front axle

In Tab. 3.5 the list of input signals with unit, allowed range, expected accuracy and noise is displayed:

Signal name	Unit	Range	Accuracy	Maximal noise
Yaw rate	$°/s$	±1.7453	0.005	0.096
Longitudinal acceleration	g	±4.1768	0.0001274	0.064
Lateral acceleration	g	±4.1768	0.0001274	0.064
Wheel velocity	$1/pm$	$0 - 4095$	1	$-$
Wheel velocity status	-	$0 - 3$	1	$-$
Steering angle	$°$	±3276	0.1	0.1
Steering angle status	-	$0 - 255$	1	$-$
Steering angle message count	-	$0 - 15$	1	$-$
Steering angle checksum	-	$0 - 15$	1	$-$
Machine velocity	rpm	±60000	1	$-$

Table 3.5: List of input signals

The list of desired output signals can be split into the vehicle states and parameters:
Vehicle states:

- Angular wheel velocity of the front axle

    – Measured by the four wheel speed sensors

- Longitudinal Tyre slip of the front axle

- Steering angle and status

    – Measured by the steering angle sensor

- Norm velocity and status

- Longitudinal and lateral acceleration

    – Measured by the yaw rate sensor

- Longitudinal and lateral velocity

- Yaw rate

    – Measured by the yaw rate sensor

- Side slip angle

Parameters:

- Vehicle mass

- Maximum longitudinal acceleration and status

- Minimum inverse curve radius and status

- Trip- and Odometer value

- Road friction of the front axle

- Vehicle observer confidence

In Tab. 3.6, unit, range and aimed accuracy are listed for the output signals. Where most of the output signals are obvious, the minimum inverse curve radius represents the inverse of the minimum possible drivable curve radius for the current estimated road friction coefficient. For more details see sub-chapter 3.6.

After all input and output signals are defined, now, the subsystems of the vehicle observer will be explained in detail. The first subsystem to be presented in the following section is the plausibility check.

Signal name	Unit	Range	Accuracy
Angular wheel velocity (front axle)	rad/s	± 250	0.0078
Longitudinal Tyre slip (front axle)	-	± 1	0.0156
Steering angle	rad	± 2.529	0.00007
Norm velocity	kph	$0 - 250$	0.0039
Longitudinal acceleration	m/s^2	± 17.658	0.001
Lateral acceleration	m/s^2	± 17.658	0.001
Longitudinal velocity	m/s	± 63.9	0.0019
Lateral velocity	m/s	± 10	0.0004
Yaw rate	rad/s	± 1.745	$6.1e^{-5}$
Side slip angle	rad	± 1.5707	$6.1e^{-5}$
Vehicle mass	kg	$1000 - 2050$	50
Maximum longitudinal acceleration	m/s^2	$0 - 8$	0.0001
Minimum inverse curve radius	$1/m$	$0 - 10$	0.00015
Trip- and Odometer	km	$0 - 9999999$	0.1
Road friction	$-$	$0.1 - 1.2$	0.1
Vehicle Observer confidence	$-$	$0 - 1$	0.01
Signal status	$-$	$0 - 1$	1

Table 3.6: List of output signals

3.3 Plausibility Check

As the performance of the vehicle observer depends on the input signals a novel plausibility check is implemented. This sub-function checks the sensor signals which then serve the observer. Moreover, the lately published ISO 26262 [35] defined new requirements for the software integration in vehicles. Here, guidelines for necessary software safety mechanisms at the software architecture level are specified. To fulfil these requirements a novel robust plausibility check is presented here with regard to the work of Versmold and Saeger [65].

The function plausibility check as the first receiver verifies the incoming sensor signals and detects faulty or missing signals. It basically consists of four subsystems: detection mechanism, correction mechanism, calculation of signal confidence and vehicle observer activation. Moreover, the sensor signals are converted to International System of Units (SI) at the beginning of the plausibility check. The arrangement of the plausibility check is shown in Fig. 3.9.
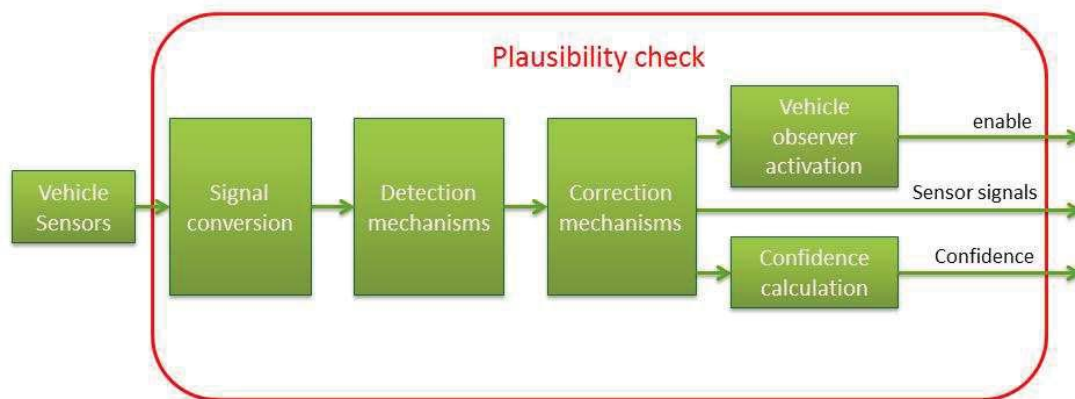
Figure 3.9: Structure with subsystems of the Vehicle Observer

The signal error detection mechanisms are set together out of a single signal check, a redundant signal check and a model-based signal check. Moreover, some error handling mechanisms are included in this function. Here, signals that are detected as faulty are corrected in the redundant check, if possible, and missing signals are replaced temporarily. Additionally, an offset compensation is implemented during standstill. The function is completed by the calculation of the confidence and an activation decision of the vehicle observer algorithm. The precise functionality of each block will be explained in the next sections starting with the signal conversion towards SI.

3.3.1 Signal Conversion

The SI is the most widely used modern form of metric systems in science. It is based on seven base units and 22 named and an indeterminate number of unnamed coherent derived units to build a coherent system. The first standards were published in 1960.
In this case, SI is used to avoid functional errors that are caused due to false presumptions of the signal unit. All project partners agreed to develop their functions on this international system. But as there is no possibility to influence the sensor signal units, the vehicle observer is responsible for the conversion.
The converted signals, signal unit, factor and SI unit are listed in Tab. 3.7. It has to be noticed that for the steering angle the steering gear ratio has been considered since for most ADAS and vehicle model equations, the steering angle at the front wheels is used instead of the steering angle at the steering wheel.

Signal name	Sensor Unit	Factor	SI unit
Yaw rate	$°/s$	$\frac{\pi}{180}$	rad/s
Acceleration	g	9.81	m/s^2
Wheel velocity	$1/pm$	$\frac{2\pi}{60}$	rad/s
Steering angle	$°$	$\frac{\pi}{180 \times 22.6}$	rad

Table 3.7: List of converted signals

3.3.2 Detection Mechanisms

The detection mechanisms block is designed to detect signal errors and to report the false sensor functionality to the correction mechanisms afterwards. The subsystem composed of the single signal check, the redundant signal check and the model based signal check. These functions are executed simultaneously and are independent of each other. The detailed functionality of each detection mechanism is explained in the following.

Single signal check

The single signal check contains the range check of all sensor signals, the check of gradients and the analysis of status signals to validate signal correctness.
The range check is done by comparing the current signal with the range given by the respective data sheet (see Tab. 3.5).
The check of gradient for every signal is done in the second sub function. The limits for the absolute gradient value were evaluated by the analysis of measurement data from the prototype in driving situations with high dynamics (see Tab. 3.8). The effects of the TorVec lead to a bigger absolute gradient value on the front axle.
The value of the confidence calculation is equal to one whenever the range and gradient check detect no failure. If the signal value, or rather the gradient, does not exceed a

Signal name	Sensor Unit	Absolute gradient
δ	rad	$0.0352\ [rad/s]$
a_x	m/s^2	$1.6992\ [m/s^2]$
a_y	m/s^2	$3.1992\ [m/s^2]$
r	rad/s	$0.1396\ [rad/s^2]$
$\omega_{1,2}$	rad/s	$14.2031\ [rad/s^2]$
$\omega_{3,4}$	rad/s	$2.9063\ [rad/s^2]$

Table 3.8: List of converted signals

specific lower threshold, the confidence value is not affected. As soon as the property value exceeds this lower threshold the confidence value decreases linearly until it reaches its minimum by crossing the upper threshold. The process of the confidence value calculation can be seen in Fig. 3.10. As the falsification has different influences on the vehicle control, for instance the information of the wheel speeds are more important than the lateral acceleration, there are specific confidence limits for each signal. The explanation will be given in section 3.3.4.
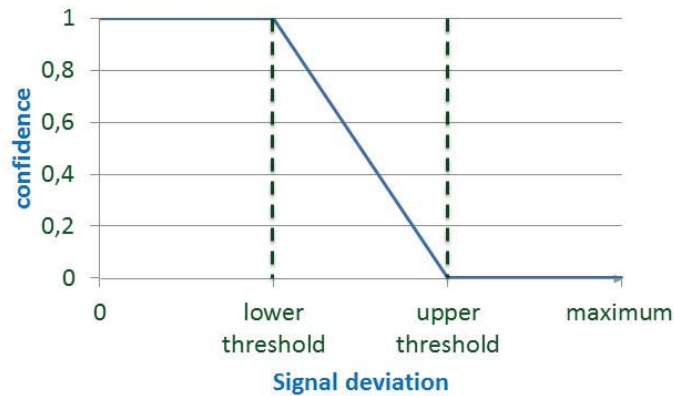
Figure 3.10: Confidence process for a single signal check

Additionally, the status signals are evaluated in the single signal check as well. The status for the specific wheel velocity is zero for a correct signal and the steering angle status for a correct signal is seven. All other values are judged as implausible signal. As there are no status signals for the accelerations and the yaw rate, the signals are set to their maximum values if the sensor is disconnected. So the diagnosis for the signals measured by the yaw rate sensor works for a broken or disconnected sensor and, thereby, more signal checks have to be applied in the remaining detection mechanisms. In general, the confidence is lowered if the status signals indicate an implausible sensor signal beginning

from a time window of at least 5 time steps only. This timing was implemented to avoid jumps in the confidence that may affect the ADAS influence on the vehicle by oscillating actuator commands. This would mean a downgraded level of comfort to the driver.

For the steering angle two more signals are analysed in terms of signal correctness. The message count signal monitors the transmission of the steering sensor. It informs the receiving functions if messages are lost between the reception of two messages by increasing the value for every sent message. As the signal has a range of $0 - 15$ it comes to an overflow when a new message is transmitted and the previous message count value was 15. So changes by 1 and 16 between two steps are seen as correct signal whereas other values indicate a problem. The checksum of the steering angle represents the checksum of all bytes on the CAN matrix to detect errors that may have been introduced during transmission. The rule to build the checksum, thus verifying the data integrity, is:

$$
\begin{aligned}
\text{temp\_result} =& \text{lowerbyte(LWS\_Angle) XOR higher byte(LWS\_Angle)} \\
& \text{XOR LWS\_Speed XOR LWS\_Stat} \\
\text{checksum} =& \text{higher nibble(temp\_result)XOR lower nibble (temp\_result)} \\
& \text{XOR Msg\_Count}
\end{aligned}
\tag{3.65}
$$

The terms "lowerbyte" and "higherbyte" are used when a data type uses more than one byte. The "lowerbyte" is the byte that holds the least significant part of an integer - the last eight bits of a 16-bit signal. Vice versa the "higherbyte" holds the most significant part - the first eight bits of a 16-bit signal. Likewise, the "lowernibble" contains the least significant part of a 8-bit signal and the "highernibble" the most significant part.

Redundant signal check

Compared to the single signal check the redundant signal check offers a much higher detection potential. It uses redundant sensor signals for the analysis and calculates the confidence value from the difference between them. The obvious disadvantage of this method is the need of redundant sensors which stands in conflict to the cost optimisation in the automotive production.

As the prototype will not be equipped with redundant sensors the angular wheel speeds ω_i of the front axle and the machine velocities Ω_i are used for the redundant signal check. Hence, the rotation speed should not deviate a lot since they are statically connected. Falsification of this check would indicate either a mechanical or a communicational problem. As a consequence the torque of the motors would be set to zero in order to prevent unsafe motor control that may result in an unstable state of the vehicle.

In order to not affect the vehicle performance during small deviations a safety gap of $15\,rad/s$ was implemented. The inequality for the evaluation of the redundant signal check including the conversion of the machine velocity is:

$$
\left| \omega_i - \left| \Omega_i \frac{\pi}{30} \right| \right| < 15 \ \frac{1}{sec}, \text{ for } i = 1, 2.
\tag{3.66}
$$

Moreover, the different angular wheel speeds are seen as additive redundant signals which have a smaller influence on the confidence than the proper check introduced before. This check was implemented to monitor and validate all measured wheel speeds together. The analysis of the signals is arranged in two different steps: The detection of the deviation between each wheel and the determination of the deviating signal. A deviation of wheel speeds is valid when the difference of both wheel speeds divided by the smaller one is larger than 0.2:

$$\left| \frac{\omega_i - \omega_j}{min(\omega_i, \omega, j)} \right| < 0.2, \text{ for } i, j \in [1, 2, 3, 4]. \tag{3.67}$$

This check is done for each possible combination of wheel speeds. In order to determine which wheel speeds are deviating the three detection results for each wheel are added. In case that this sum is less than three the respective wheel speed is determined as valid otherwise as deviated.

Additionally, a check of axle speed is implemented. Here, the front and rear wheel detection results are summarized. If an axle deviation is detected the mean of the rear wheel speeds is assumed as reference signal. In acceleration situations especially, when the wheel slip of the driven axle is great, this method shows good performance.

The confidence of the redundant signal check depends on the results of different velocity sensors and the number of signals detected as deviated. Again, the confidence is 1 if no critical deviation of the wheel speeds is detected. With an increasing number of deviating signals the confidence decreases linearly until it is 0 when all wheel speeds are detected as deviated. Or, in case the proper redundant check fails, the confidence is lowered to 0.39 directly to cut off the motor torque immediately.

Model-based signal check

In contrast to the redundant signal check the model-based check examines the connections between different signals for the confidence assessment. Here, analytical connections based on mathematical description and vehicle behaviour modelling procures the basis for the evaluation of the signal plausibility. The here presented model-based signal check is extended by two special checks that guarantee the signal correctness for TorVec. The model-based signal check was developed on the fact, that in driving manoeuvres with side slip angle unequal 0, e.g. curve driving, the outer wheels spin with higher velocity than the inner ones. Through empirical determination in the non-linear 14 DoF simulation model based on [54] and analysis of data recorded in test drives with the prototype the following formula, which describes the dependence between wheel speed and yaw rate, could be formed:

$$\Delta \omega = \frac{b_f}{r_{eff}} \times r. \tag{3.68}$$

Here, the maximum deviation between the different wheel speeds $\Delta\omega_{max}$ should be equal to the absolute yaw rate r multiplied by the vehicle width b_f and divided by the effective tyre radius r_{eff}. As this equation was evaluated in a vehicle model the range of validity

is limited due to parameter variations during dynamic driving situations. Thus, this formula is valid as long as the side slip angle of the vehicle is below $0.1047\,rad$ which covers all "normal" driving situations.

As the activation of the function TorVec might lead to damage of the driveshaft if it distributes the torque based on wrong vehicle states, two more checks were implemented that validate the sensor data for this function. For instance, an offset in the steering angle sensor could generate a maximum delta torque even on straight road which is a big safety concern as well. Consequently, two concepts for the detection of wrong sensor signals that potentially effect mechanical damage were implemented:

1. The comparison of sensor yaw rate with the estimated yaw rate that is based on a single track model according to:

$$
\begin{aligned}
\dot{r} =& a_{21}\beta + a_{22}r + b_2\delta_f, \text{ with assumption } \beta = 0 \\
=& -\frac{11.069}{v}r + 65.444\delta_f \\
a_{22} =& \frac{2\left(l_r^2 c_r - l_f^2 c_f\right)}{Jv};\ b_2 = \frac{2c_f l_f}{J}
\end{aligned}
\tag{3.69}
$$

   Here, the estimated longitudinal velocity of the previous time step $v_{x,k-1}$ is used. Finally, the difference between the measured yaw rate and the computed yaw rate should remain under $0.1\,rad/s$ to be valid.

2. A rough interrelation between the angular wheel speed process and the current longitudinal acceleration. If the wheel is rolling when driving straight, the wheel acceleration and vehicle acceleration are almost the same. This check is another validation of the information about the longitudinal motion of the vehicle provided by different sensors. The equation for this check is:

$$
\begin{aligned}
a_x =& \dot{\omega} \times r_{eff} \\
=& \frac{\omega_{3,k} - \omega_{3,k-25}}{\Delta T} \times r_{eff}
\end{aligned}
\tag{3.70}
$$

Here, one of the non-driven wheels wheels that is not influenced by the active torque distribution was chosen. The long time period between the two wheel speed measurements, 24 time steps which means $240\,ms$, was selected to compensate noise effects during low speed.

The confidence value is calculated from the deviation between the model equation and the measured values in all cases by adding the result of the model-based equation to the default confidence value one. Since the equation result affects the confidence only if this result is negative, the confidence value will decrease bounded to the formula.

3.3.3 Correction Mechanisms

The correction mechanisms block is composed of the replacement of signals and the offset compensation. Just as in the detection mechanisms the blocks are executed si-

multaneously and work independently. The functionality of this block is based on the results of the detection mechanisms. The detailed description is explained in the next two sub-sections.

Signal replacement

The signal replacement is designed to catch two possible failures: Delayed or missing and faulty sensor signals. The replacement of faulty sensor signals touches upon the results of the redundant signal check described in 3.3.2. Here, the index signal sets the switch for the signal replacement where the mean of the valid wheel speeds is taken as reference.
The exact functionality of the signal replacement by the use of Markov chain concept will be given in 4.

Offset compensation

As any of the equipped sensors has offset problems over lifetime or due to incorrect mounting, the detection and correction of that deviation is very important for a robust and reliable state estimation. The developed concept for offset compensation integrates the sensor signals during valid standstill according to the following equation:

$$\hat{\zeta}_i = \frac{1}{t_{standstill}} \times \int u_i dt \qquad (3.71)$$

Where $\hat{\zeta}_i$ is the estimated offset, $t_{standstill}$ is the time of valid standstill and u_i is the analysed sensor signal. Here, standstill is seen as valid when the angular velocity of all four wheels is below a defined threshold near to 0. In detail, the offset is computed for the lateral and longitudinal acceleration and the yaw rate. To protect the concept against fatal sensor malfunctions, the estimated offset value is limited to the respective data of each sensor. The concept was validated with recorded sensor signals from test drives with the prototype (see section 5) and is asssuming, that the vehicle is standing on a plane surface.

3.3.4 Confidence calculation

In general, the confidence expresses the reliability and accuracy of the estimated outputs of the vehicle observer. The maximum value of the confidence is 1. In this case, the best accuracy and reliability is guaranteed for all output signals. With decreasing value the accuracy decreases successively.
The confidence was classified into three levels: the performance level where different torques on the front axle are allowed, the safety level where equal torque for the electric machines is allowed only and an emergency level where no torque will be applied.
For the performance level the lateral and longitudinal acceleration might show implausible signal information only. These two signals do not have much influence on the vehicle control. Thereby, a malfunction is not considered as critical. If the steering angle or
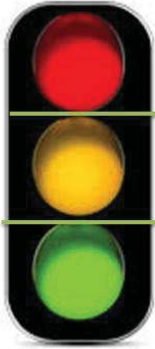
the yaw rate signals do not pass the detection checks, the torque will be kept equal since these two signals are very important for the lateral dynamics of the vehicle. As soon as the angular velocities of the vehicle indicate a problem no torque will be applied because no valid prediction of the current vehicle speed can be made and false torques might cause a vehicle accident. An overview of the confidence level is given in Fig. 3.11.

	Failed plausibility check	Confidence range	Drivetrain limitation
	ω_i, Ω_i	$[0 - 0.39]$	No torques at all
	δ, r	$[0.4 - 0.69]$	Equal torques only
	a_x, a_y	$[0.7 - 1]$	Different torques allowed

Figure 3.11: Confidence levels and drivetrain limitations

3.3.5 Vehicle observer activation

In order to save calculation capacity of the VHU, the vehicle observer algorithm should not be executed permanently. As the integrated ADAS do not affect the vehicle motion during standstill or in low speed situations the vehicle observer is activated when the vehicle surpasses a certain threshold only. Because this decision should be independent of the wheel slip the two angular velocities of the non -driven rear axle are taken into consideration.
In addition, the confidence value of the received sensor signals should be greater than 0.4. According to 3.3.4 there is no need for the ADAS for the vehicle observer outputs since no torque is applied for a confidence below this threshold.
Finally, the vehicle observer algorithm is executed if both rear wheels have an angular velocity greater than $0.1047\,rad/s$ and the confidence is above 0.4. When deactivated default vehicle states will be calculated (see 3.4.7) and the estimated parameters hold their last evaluated value.

3.4 Extended Kalman Filter Algorithm

3.4.1 Build up and functionality

The EKF-titled subsystem can be divided into three different subsystems (see Fig. 3.12).
Here, the calculation of slip and sideslip of the wheels, the computation of the tyre forces
with the Dugoff Tyre model and the execution of the EKF algorithm can be separated,
which will be explained in detail in the following subsections. The functionality of this
subsystem contains the main task of the vehicle observer function: to smooth distorted
sensor signals and to compute unmeasured vehicle states. The observed vehicle states
are: $\hat{a}_x$ the longitudinal acceleration, $\hat{v}_x$ the longitudinal velocity, $\hat{a}_y$ the lateral acceler-
ation, $\hat{v}_y$ the lateral velocity, $\hat{r}$ the yaw rate and $\hat{\beta}$ the side slip angle.
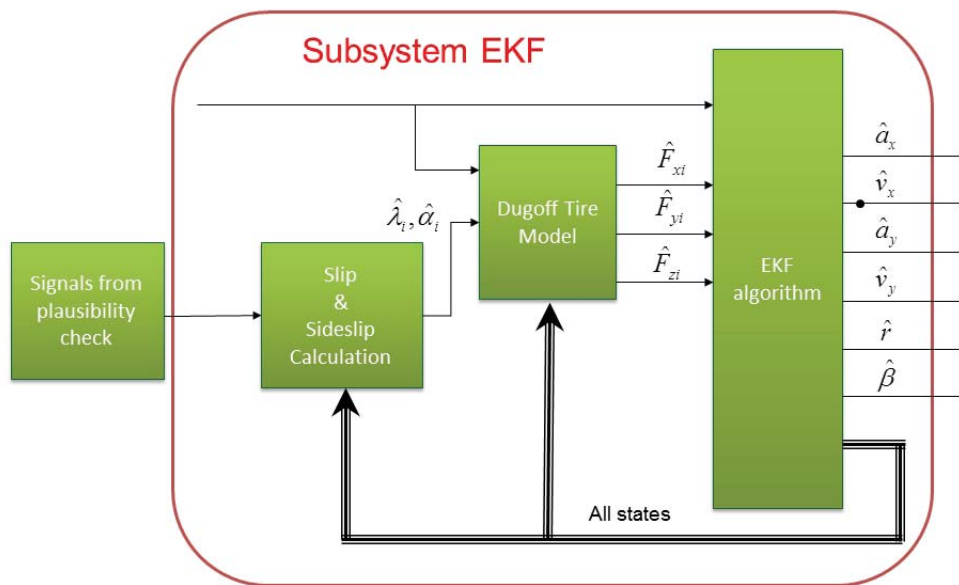
Figure 3.12: Structure of the EKF subsystem

3.4.2 Slip and Side slip Calculation

The slip describes the relative motion between the tyre and the road surface it is moving
on. Whereas the slip represents the longitudinal motion, the side slip stands for the
complementary lateral relative movement between tyre and road surface. They are basi-
cally needed to compute the tyre forces of the vehicle. The formulas for the calculation

of the front and rear slip on the left side 3.72 and right side 3.73 are:

$$\hat{\lambda}_{L,i} = \frac{\hat{r}_{eff_i}\omega_i - \left(\hat{v}_x - r\frac{a_{f/r}}{2}\right)\cos(\delta_i)}{max\left(\left|\hat{r}_{eff_i}\omega_i\right|, \left|\hat{v}_x - r\frac{a_{f/r}}{2}\right|\right)} \qquad \text{for } i = 1,3 \text{ and} \qquad (3.72)$$

$$\hat{\lambda}_{R,i} = \frac{\hat{r}_{eff_i}\omega_i - \left(\hat{v}_x + r\frac{a_{f/r}}{2}\right)\cos(\delta_i)}{max\left(\left|\hat{r}_{eff_i}\omega_i\right|, \left|\hat{v}_x + r\frac{a_{f/r}}{2}\right|\right)} \qquad \text{for } i = 2,4. \qquad (3.73)$$

Here, r_{eff} is the effective tyre radius of the particular wheel and $a_{f/r}$ is the width of the front/rear axle. These two equations are valid for a non-steered rear axle only $(\delta_3 = \delta_4 = 0)$.

Since the effective tyre radius and the longitudinal speed of the vehicle are not measured by the mounted sensors, these values are taken from the results of the vehicle observer. Thus, a feedback between the in- and outputs of the vehicle observer is created which is delayed with one discrete step in order to avoid an algebraic loop.

The equations for the computation of the front and rear sideslip on the left and right side for front and rear axle are shown as follows:

$$\hat{\alpha}_i = \delta_f - \arctan\frac{\hat{v}_y \pm rl_{f/r}}{\hat{v}_x \pm r\frac{a_{f/r}}{2}} \qquad \text{for } i = 1,2 \qquad (3.74)$$

$$\hat{\alpha}_i = -\arctan\frac{\hat{v}_y \pm rl_{f/r}}{\hat{v}_x \pm r\frac{a_{f/r}}{2}} \qquad \text{for } i = 3,4. \qquad (3.75)$$

Notice that the steering angle at the rear wheels is assumed to be zero at any time. Additional to the computation of the slip of the wheels the information of the lateral velocity is needed, which will also be taken from the vehicle observer.

With the information of the slip and side slip of the tyres and the measured sensor data it is possible to compute the tyre forces in longitudinal, lateral and horizontal direction. This is done with the Dugoff Tyre model, which is described in the next section.

3.4.3 Dugoff Tyre Model

The Dugoff Tyre model was developed by Dugoff and others in 1969 [20] as an alternative to the elastic foundation analytical tyre model. Although the applications of Pacejka [51] and Burckhardt [16] tyre models are widely spread, the Dugoff Tyre model was chosen because of the following two advantages:

- Independent values of tyre stiffness in lateral and longitudinal direction are allowed

- Direct relation of the lateral and longitudinal forces to the road friction coefficient in transparent equations

Before the model equations can be used, the horizontal tyre forces of the vehicle have to be computed. Here, the equation from Jazar [36] is chosen on the assumption that

there is no road slope:

$$\hat{F}_{z,1} = m \cdot \left(\frac{l_r}{l_f + l_r} \cdot g - \frac{h_{CoG}}{l_f + l_r} \cdot \hat{a}_x \right) \cdot \left(\frac{1}{2} + \frac{h_{CoG}}{a_f \cdot g} \cdot \hat{a}_y \right) \tag{3.76}$$

$$\hat{F}_{z,2} = m \cdot \left(\frac{l_r}{l_f + l_r} \cdot g - \frac{h_{CoG}}{l_f + l_r} \cdot \hat{a}_x \right) \cdot \left(\frac{1}{2} - \frac{h_{CoG}}{a_f \cdot g} \cdot \hat{a}_y \right) \tag{3.77}$$

$$\hat{F}_{z,3} = m \cdot \left(\frac{l_f}{l_f + l_r} \cdot g + \frac{h_{CoG}}{l_f + l_r} \cdot \hat{a}_x \right) \cdot \left(\frac{1}{2} + \frac{h_{CoG}}{a_r \cdot g} \cdot \hat{a}_y \right) \tag{3.78}$$

$$\hat{F}_{z,4} = m \cdot \left(\frac{l_f}{l_f + l_r} \cdot g + \frac{h_{CoG}}{l_f + l_r} \cdot \hat{a}_x \right) \cdot \left(\frac{1}{2} - \frac{h_{CoG}}{a_r \cdot g} \cdot \hat{a}_y \right) \tag{3.79}$$

where g is the gravitational acceleration constant and h_{CoG} is the height of the CoG. By the use of the Dugoff Tyre model the longitudinal force is given by:

$$F_{x,i} = C_x \cdot \frac{\hat{\lambda}_i}{1 + \left| \hat{\lambda}_i \right|} \cdot f(\sigma_i). \tag{3.80}$$

The lateral force is given by:

$$F_{y,i} = C_y \cdot \frac{\tan(\hat{\alpha}_i)}{1 + \hat{\lambda}_i} \cdot f(\sigma_i). \tag{3.81}$$

C_x and C_y are the longitudinal and lateral cornering stiffness and σ_i is given by:

$$\sigma_i = \frac{\mu_i \cdot F_{z,i} \cdot (1 + \hat{\lambda}_i)}{2 \cdot \left[\left(C_x \cdot \hat{\lambda}_i \right)^2 + (C_y \cdot \tan(\hat{\alpha}_i))^2 \right]^{\frac{1}{2}}}. \tag{3.82}$$

μ_i is the tyre-road friction coefficient of the respective tyre. The function of σ_i is given by:

$$f(\sigma_i) = (2 - \sigma_i) \cdot \sigma_i, \qquad \text{if } \sigma_i < 1 \tag{3.83}$$
$$f(\sigma_i) = 1, \qquad \text{if } \sigma_i \geq 1 \tag{3.84}$$

Together with the measured sensor signals these calculated tyre forces are the input for the EKF algorithm, which is described in the next section.

3.4.4 EKF Algorithm

As explained in 3.1.2 any type of the Kalman filters needs model equations to predict the system behaviour. For the representation of lateral dynamics with low lateral acceleration (less than $4\,m/s^2$) the well-known STM is often used. But as this model contains many simplifications, e.g. the two tyres of an axle are merged into a single tyre in the middle of the axle, the CoG is assumed to be on the road level, etc., a non-linear vehicle

model is chosen for this observer design in order to achieve a higher precision.
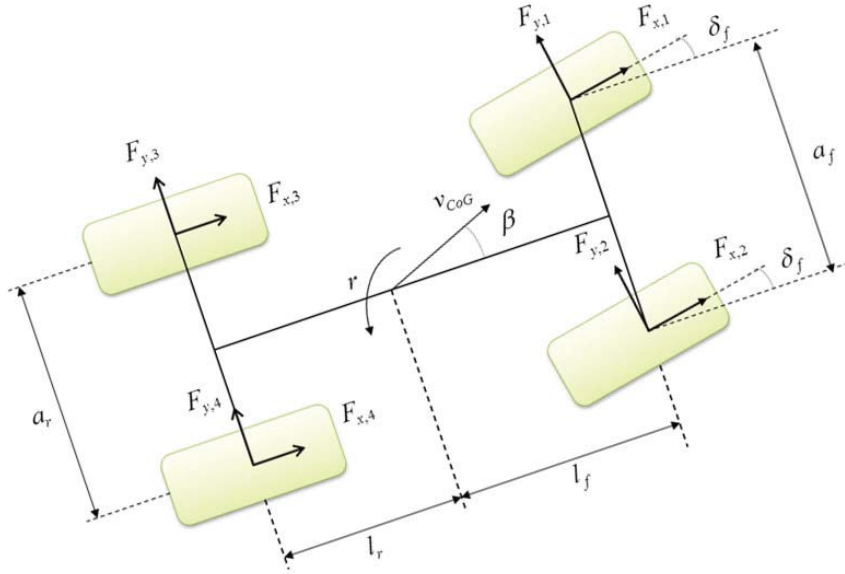
Figure 3.13: Non-linear two-track model

Moreover, the use of a non-linear model guarantees validation for driving manoeuvres with high vehicle dynamics. The vehicle model shown in Fig. 3.13 represents the longitudinal and lateral behaviours and the yaw rate dynamics in response to the interaction between the four wheels. In this vehicle model aerodynamic resistance, roll, pitch and heave motions are neglected. Thus, the dynamic equations for the two- track model are given by:

$$\dot{a}_x = 0 \tag{3.85}$$

$$\dot{v}_x = v_y \cdot r + \frac{1}{m}\left[(F_{x,1} + F_{x,2}) \cdot \cos\delta_f + F_{x,3} + F_{x,4} - (F_{y,1} + F_{y,2}) \cdot \sin\delta_f\right] \tag{3.86}$$

$$\dot{a}_y = 0 \tag{3.87}$$

$$\dot{v}_y = -v_x \cdot r + \frac{1}{m}\left[(F_{y,1} + F_{y,2}) \cdot \cos\delta_f + F_{y,3} + F_{y,4} + (F_{x,1} + F_{x,2}) \cdot \sin\delta_f\right] \tag{3.88}$$

$$\dot{r} = \frac{1}{I_z}\left[l_f \cdot ((F_{x,1} + F_{x,2}) \cdot \sin\delta_f + (F_{y,1} + F_{y,2}) \cdot \cos\delta_f) - l_r \cdot (F_{y,3} + F_{y,4})\right] \tag{3.89}$$

$$\dot{\beta} = -r + \frac{1}{m \cdot \sqrt{\left(\hat{v}_x^2 + \hat{v}_y^2\right)}}\left[(F_{x,1} + F_{x,2}) \cdot \sin\left(\delta_f - \hat{\beta}\right)\right.$$

$$\left. + (F_{y,1} + F_{y,2}) \cdot \cos\left(\delta_f - \hat{\beta}\right) + (F_{y,3} + F_{y,4}) \cdot \cos\left(\hat{\beta}\right)\right] \tag{3.90}$$

In this equation the orientation of the forces is in accordance to Fig. 3.13. By applying 3.85 and 3.87 to be zero, the Kalman filter transfer function for these two states gets a first-order polynomial that is called first-order delay element (PT1-element).

The state vector of the estimated system $\hat{x}$ is a combination of longitudinal velocity and acceleration, lateral velocity and acceleration, yaw rate and side slip angle:

$$\hat{x} = \left[\hat{a}_x, \hat{v}_x, \hat{a}_y, \hat{v}_y, \hat{r}, \hat{\beta}\right]^T \tag{3.91}$$

the input consists out of the longitudinal and lateral tyre forces and the steering angle:

$$u = \left[\hat{F}_{x,1}, \hat{F}_{y,1}, \hat{F}_{x,2}, \hat{F}_{y,2}, \hat{F}_{x,3}, \hat{F}_{y,3}, \hat{F}_{x,4}, \hat{F}_{y,4}, \delta_f\right]^T \tag{3.92}$$

Where the superscripted T stands for the transpose of the vector.

Hence, the two-track model can be described in state space by this equation:

$$\hat{\dot{x}} = f(\hat{x}, u) \tag{3.93}$$

As the states of the lateral and longitudinal velocity are integrations of their respective accelerations, the differential equations from 3.86 to 3.90 are valid for the vectorial non-linear function f.

For the concept of the EKF algorithm it is very important to define the relationship between the system states and the measured values. This is very easy if the measured signal is identical with the system state. In this approach this is appropriate for the longitudinal / lateral acceleration and the yaw rate. These are system states and so the measurement equation is linear as shown in the following example for the longitudinal acceleration:

$$y_1 = a_x = C_1 \cdot y \text{ with } C_1 = [0000100]. \tag{3.94}$$

The estimation of the system states will improve its precision, with the number of measured values involved. As the vehicle is equipped with four wheel speed sensors the following equations, that are valid for situations without any slip $\lambda_i = 0$, are used. The wheel speed in the vehicle coordinates are given by:

$$v_{x,1} = v \cdot \cos\beta - \frac{a_f}{2} \cdot r, \quad v_{y,1} = v \cdot \sin\beta + l_f \cdot r, \tag{3.95}$$

$$v_{x,2} = v \cdot \cos\beta + \frac{a_f}{2} \cdot r, \quad v_{y,2} = v \cdot \sin\beta + l_f \cdot r, \tag{3.96}$$

$$v_{x,3} = v \cdot \cos\beta - \frac{a_f}{2} \cdot r, \quad v_{y,3} = v \cdot \sin\beta - l_f \cdot r, \tag{3.97}$$

$$v_{x,4} = v \cdot \cos\beta + \frac{a_f}{2} \cdot r, \quad v_{y,3} = v \cdot \sin\beta - l_f \cdot r. \tag{3.98}$$

With these four equations and the use of the transformation into the wheel coordination with equation 2.13 the wheel velocity of the four wheels in longitudinal direction can be

computed:

$$v_x^{\omega_1} = v \cdot \cos\left(\beta - \delta_f\right) - \frac{a_f}{2} \cdot r \cdot \cos\delta_f + l_f \cdot r \cdot \sin\delta_f, \tag{3.99}$$

$$v_x^{\omega_2} = v \cdot \cos\left(\beta - \delta_f\right) + \frac{a_f}{2} \cdot r \cdot \cos\delta_f + l_f \cdot r \cdot \sin\delta_f, \tag{3.100}$$

$$v_x^{\omega_3} = v \cdot \cos\beta - \frac{a_f}{2} \cdot r \cdot \cos\delta_f - l_f \cdot r \cdot \sin\delta_f, \tag{3.101}$$

$$v_x^{\omega_4} = v \cdot \cos\beta + \frac{a_f}{2} \cdot r \cdot \cos\delta_f - l_f \cdot r \cdot \sin\delta_f. \tag{3.102}$$

By the use of these wheel velocities and the estimated effective tyre radius $\hat{r}_{eff,i}$ the rotational wheel speeds can be calculated:

$$\hat{\omega}_1 = \frac{1}{\hat{r}_{eff,1}} \cdot \left(\sqrt{\hat{v}_x^2 + \hat{v}_y^2} \cdot \cos(\delta_f - \hat{\beta}) - \frac{a_f}{2} \cdot r \cdot \cos\delta_f + l_f \cdot r \cdot \sin\delta_f\right) \tag{3.103}$$

$$\hat{\omega}_2 = \frac{1}{\hat{r}_{eff,2}} \cdot \left(\sqrt{\hat{v}_x^2 + \hat{v}_y^2} \cdot \cos(\delta_f - \hat{\beta}) + \frac{a_f}{2} \cdot r \cdot \cos\delta_f + l_f \cdot r \cdot \sin\delta_f\right) \tag{3.104}$$

$$\hat{\omega}_3 = \frac{1}{\hat{r}\_{eff,3}} \cdot \left(\sqrt{\hat{v}_x^2 + \hat{v}_y^2} \cdot \cos(\hat{\beta}) - \frac{a_r}{2} \cdot r\right) \tag{3.105}$$

$$\hat{\omega}_4 = \frac{1}{\hat{r}_{eff,4}} \cdot \left(\sqrt{\hat{v}_x^2 + \hat{v}_y^2} \cdot \cos(\hat{\beta}) + \frac{a_r}{2} \cdot r\right). \tag{3.106}$$

As the assumption for no tyre slip is not valid for all driving situations, an adaptive covariance matrix, see 3.4.6 for details, is formed to compensate the different vehicle behaviour during tyre slip.

Finally, the output of the two-track model in state space is described by:

$$y = h(\hat{x}, u), \text{with } h = [\hat{\omega}_1, \hat{\omega}_2, \hat{\omega}_3, \hat{\omega}_4, a_x, a_y, r]. \tag{3.107}$$

With the definition of the system equation the algorithm of the EKF can be explained in the next sections.

Prediction

The concept of the EKF can be derived from the design of a Kalman filter for linear systems. Here, the non-linear system equations are linearised around the current estimated system trajectory, so that the SKF equations can be applied. The postulate for the utilisation of the traditional stochastic equations is to discretise the system equation 3.93. Here, the assumption was made that the process has a state vector $x \in \Re^n$ with

$$x_k = f(x_{k-1}, u_{k-1}, w_{k-1}), \tag{3.108}$$

where w_k is a random variable that represents the process noise which is assumed to be zero-mean and uncorrelated. In general, the process noise is not assignable because of uncertainties of the non-linear system where the measurement noise should be analysed

by the sensor producer and documented in the specific data sheet. The system input is supposed as deterministic.

In the prediction step the approximate state and the priori error covariance matrix are calculated out of the system equations. In practice the exact individual noise for the process noise w_k is not known at each time step. However, one can approximate the state and measurement vector without setting them to zero.

The priori state is calculated by:

$$\hat{x}_k(-) = f(\hat{x}_{k-1}, u_{k-1}, 0) \tag{3.109}$$

and the priori error covariance matrix by use of

$$P_k(-) = \Phi_{k-1}^{[1]} P_{k-1}(+) \Phi_{k-1}^{[1]T} + W_k Q_{k-1} W_k^T, \tag{3.110}$$

with $\Phi_k^{[1]}$ as the Jacobian matrix of the partial derivatives of f with respect to x, that is

$$\Phi_{k-1[i,j]}^{[1]} = \frac{\partial f_{[i]}}{\partial x_{[j]}}(\hat{x}_{k-1}, u_{k-1}, 0), \tag{3.111}$$

and W_k as the Jacobian matrix of the partial derivatives of f with respect to w, that is

$$W_{k-1[i,j]}^{[1]} = \frac{\partial f_{[i]}}{\partial w_{[j]}}(\hat{x}_{k-1}, u_{k-1}, 0). \tag{3.112}$$

Here, i represents the dimension of the model functions and j the dimension of the system state which are equal in this application.

The influence of the additional yaw moment M_z, that is created by the torque distribution of TorVec, on the vehicle states and the priori system states is noticeable when the torque difference is close to the maximum only. In simulations the vehicle observer showed robust performance during active TorVec. Thus, the system equations were not modified to consider this yaw moment. Therefore, is applicable for most other vehicles as well.

Correction

In the correction step the prediction results are corrected with the help of the measurements and the priori error covariance is updated. Here, the optimal Kalman gain, the posterior covariance matrix and the predicted estimate on the measurements are computed. By that, the Kalman algorithm is completed.

Similar to the system function the measurement function 3.107 is linearised around the current predicted state and the zero mean measurement noise by the use of the traditional stochastic equations with a measurement $y \in \Re^m$:

$$y_k = h(x_{k-1}, u_{k-1}, v_{k-1}). \tag{3.113}$$

Again, v_k is assumed to be a random variable that represents the process noise which is zero-mean and uncorrelated.

First, the optimal Kalman gain is computed by:

$$\bar{K}_k = P_k(-)H_k^{[1]T} \left[H_k^{[1]} P_k(-) H_k^{[1]T} + V_k R_k V_k^T \right]^{-1},$$
(3.114)

with H_k as the Jacobian matrix of the partial derivatives of h with respect to x,

$$H_{k-1[i,j]}^{[1]} = \frac{\partial h_{[i]}}{\partial x_{[j]}} \left(\hat{x}_{k-1}, u_{k-1}, 0 \right),$$
(3.115)

and V_k as the Jacobian matrix of the partial derivatives of h with respect to v,

$$V_{k-1[i,j]}^{[1]} = \frac{\partial h_{[i]}}{\partial v_{[j]}} \left(\hat{x}_{k-1}, u_{k-1}, 0 \right).$$
(3.116)

The error covariance matrix update is computed by:

$$
\begin{aligned}
P_k(+) &= \left(I - \bar{K}_k H_k^{[1]} \right) P_k(-) \left(I - \bar{K}_k H_k^{[1]} \right)^T + \bar{K}_k V_k P_k V_k^T \bar{K}_k^T \\
&= \left(I - \bar{K}_k H_k^{[1]} \right) P_k(-),
\end{aligned}
$$
(3.117)

and, finally, the predicted state estimate is calculated by the use of the equation:

$$\hat{x}_k(+) = \hat{x}_k(-) + \bar{K}_k (y_k - H_k^{[1]} \hat{x}_k(-)).$$
(3.118)

For the implementation of the EKF, the system equations of the vehicle model have to be discretised. For this purpose the discretisation from Euler is chosen:

$$x_{k+1} = x_k + T \cdot f(x_k, u_k).$$
(3.119)

With the definition of the system equation and the explanation of the algorithm the proof of observability of the EKF can be explained in the next section.

3.4.5 Proof of observability

To guarantee that the presented non-linear system is observable, thereby the concept is feasible, an analysis of the observability is given here. Moreover, the performance of an observer is highly linked to the observability of the system. Thus, the proof of observability is a given for the presented observer concept.

Observability, in general, means that when the input vector u and the system matrices A and H are known with the process of the output vector z in a finite time $t_0 \leq t \leq t_1$ the initial state of the system $x(t_0)$ can be determined uniquely.

Since the chosen system is non-linear the observability analysis is done locally by using the Lie algebra [44]. In general, the system with $\dot{x} = f(\hat{x}, u)$ and $z = h(\hat{x})$ is locally observable at x_0 if there exists a neighbourhood of x_0 such that every x in that

neighbourhood other than x_0 is distinguishable from x_0. In general, the jth order Lie derivative of the function h_i along the vector field f is defined as:

$$L_f^j h_i(\hat{x}, u) = \frac{\partial L_f^{j-1} h_i(\hat{x}, u)}{\partial x} \cdot f(\hat{x}, u) \text{ with } j = 1, \dots, 6, \tag{3.120}$$

where

$$L_f^0 h(\hat{x}, u) = h(\hat{x}, u). \tag{3.121}$$

The observability matrix for each function h_i can be computed by:

$$o_j = \left[h_i(\hat{x}, u), L_f^1 h_i(\hat{x}, u), \dots, L_f^5 h_i(\hat{x}, u) \right]^T \text{ with } i = 1, \dots, 7. \tag{3.122}$$

The system is locally observable at x_0 if the observability matrix of all functions h has the same rank as the state dimension:

$$O_i = [o_1, o_2, o_3, o_4, o_5, o_6, o_7]^T. \tag{3.123}$$

As the rank of this matrix was constant, $rank(O_i) = 6$, throughout all simulations and post-processing simulations with measurements from the prototype as inputs, the system is locally observable. So the requirement for the observer design is fulfilled.

3.4.6 Adaptive System Covariance Matrix

During simulations it could be noticed that the performance of the vehicle observer showed not the desired accuracy. The reason for this is the accuracy of the non-linear two-track model equations in situations with high tyre slip (3.72, 3.73, 3.103 - 3.106), since in these cases the assumption for having no tyre slip is not valid of course.
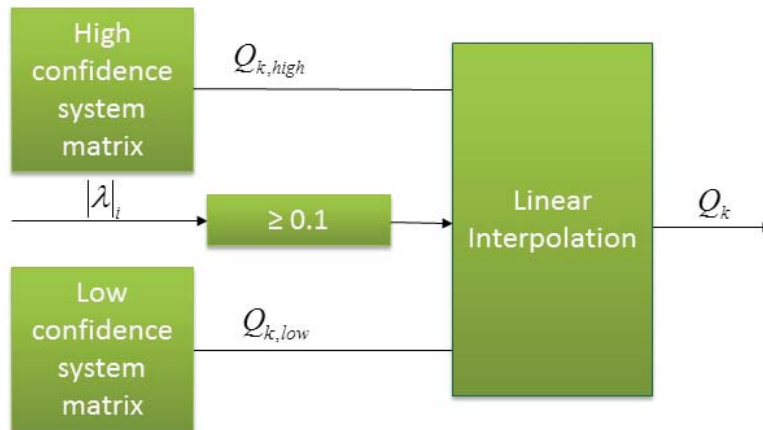
Figure 3.14: Structure of adaptive covariance matrix

To cope with this problem two system covariance matrices were designed: One for high model confidence during low tyre slip and one for low model confidence when the tyre slip exceeds a defined threshold. However, since switching might cause algorithm instability or lower the passenger comfort due to quick changing estimated vehicle states an interpolation between the two system covariance matrices was implemented (see Fig. 3.14). This interpolation guarantees a smooth transition of the matrices and prevents unwanted rapid changes of the observed states.

3.4.7 Default vehicle states

Whenever the vehicle observer algorithm is not activated (see 3.3.5) the so called default vehicle states are the output. They are composed partly of the sensor signals and partly by alternative computations. It is worth mentioning that the plausibility check is always activated and, thereby, the pre-processing computations are executed anyway.

For the states that are measured by sensors, longitudinal acceleration a_x, lateral acceleration a_y and yaw rate r, the signals are routed through the function whenever the vehicle observer algorithm is not activated.

As the lateral velocity v_y and the side slip angle β cannot be calculated by simple equations and these states are not essential for any other function, these states are set to zero whenever the vehicle observer algorithm is not in process.

As the longitudinal velocity v_x is displayed in the instrument cluster and other functions receive this vehicle state as well, an alternative effortless computation for the velocity is implemented. Here, all measured angular speeds, from the wheels ω_i and the electric machines Ω_i, are used. The electric machine speeds are utilised to determine the velocity direction, positive for forward and negative for backward movement, and to detect signal errors in a very basic way. The equation for the computation of the longitudinal velocity is:

$$v_x = sign(\Omega_2) \cdot (sign\,(\Omega_1) \wedge sign\,(\Omega_2)) \cdot \frac{0.2833}{4} \cdot \sum_{i=1}^{4} \omega_i. \qquad (3.124)$$

Here, the value 0.2833 represents the static effective tyre radius r_{stat}.

3.5 Parameter Estimation

As the vehicle has many variable parameters which have a great influence on the stability, the function parameter estimation was implemented in the vehicle observer. Here, the most important vehicle and environmental variables are estimated online. The input of this estimation is composed of all computed values in the EKF algorithm subsystem. Here, slip and side slip of tyres, tyre forces, steering angle, vehicle states and activation Boolean, which is determined in the plausibility check, are part of it.

There were many estimation methods developed in the past. In this case, the use of a combination of Kalman filter and Bayesian networks, an approach with non-linear observer and others were designed. Due to the fact that the computational effort of these concepts is very high, this work concentrates on an approach with low computational
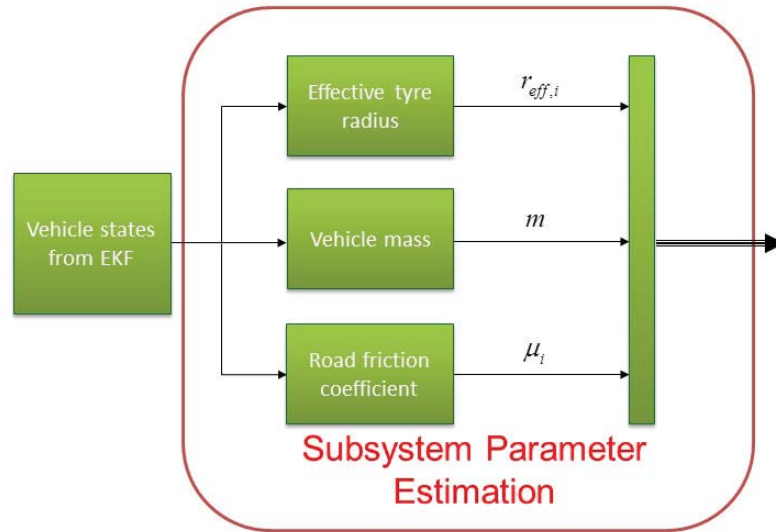
Figure 3.15: Structure of the parameter estimation

load in order to keep the algorithm of the whole vehicle observer real-time compatible. Therefore, an event seeking characteristic was chosen for the parameter estimation as, for instance, the estimation of the vehicle mass during constant velocity is not meaningful. The calculations for the three estimated parameters, effective tyre radius r_{eff}, vehicle mass m and the road friction coefficient μ_i, are arranged in parallel subsystems (see Fig. 3.15). First the estimation of the effective tyre radii is explained in the next section. The estimation of the vehicle mass is given in 3.5.2. Finally, the computation of the approximated road friction coefficient is given.

3.5.1 Effective Tyre Radius

In general, the tyre can be modelled as a springer-damper system in vertical and torsional direction, see 2.1.2. As the tyre radius is dependent on air pressure, speed and load, the effective tyre radius is very mutable. Basically, the effective radius, among other effects, is dependent on the inflation pressure. If this pressure decreases the tyre radius decreases as well which makes the wheel turn faster. Moreover, the estimation of the effective tyre radius is important for the calculation of the tyre slip (see equations 3.72 and 3.73) and the estimation of system states (see equations 3.103-3.106).
As shown in Fig. 3.16 the tyre radius on the front axle decreases with increasing velocity and vice versa for the rear axle. These effects were simulated during a straight line acceleration by the use of the complete vehicle model. The variation in terms of speed is strongly dependent on the tyre carcass structure. These results are used to demonstrate the general variation of the effective tyre radius only. In this case the CoG is located in the rear half of the vehicle because of the heavy high voltage battery. By that, the load force at high longitudinal accelerations has more effect on the rear wheels and with
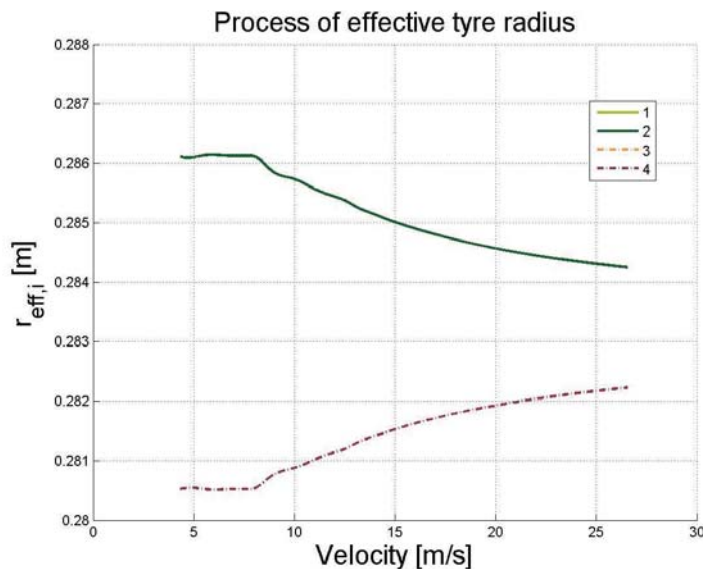
Figure 3.16: tyre radius over vehicle speed

smaller acceleration values the load is distributed to the front axle. Thereby, the effective tyre radius on the front axle decreases while that on the rear axle increases.

Additionally, lateral dynamics affect the effective tyre radius due to centrifugal force and vehicle weight distribution. A process of this effect is displayed in Fig. 3.17 where a sine with dwell driving scenario was simulated. Here, the influence of the CoG on the effective tyre radius of front and rear axle can be identified again. Furthermore, the left wheels have a smaller radius for negative yaw rates, due to the lateral load in right curves that is mainly on the left vehicle side, and a bigger radius for positive yaw rates since the lateral load in left curves is mainly on the right vehicle side. Vice versa this is valid for the right side as well. Because this effect has a direct impact on the wheel angular velocity ω_i, it has not to be taken into account in the effective tyre radius estimation since the wheel angular velocity is used in the computation of the effective tyre radius.

The equation for the estimation of the effective tyre radius needs the information of the longitudinal velocity and the respective angular wheel speed [36]:

$$r_{eff,i} = r_{0,i} - \epsilon_{r,i} = \frac{v_x}{\omega_i}, \tag{3.125}$$

where $r_{0,i}$ is the initial tyre radius at standstill and $\epsilon_{r,i}$ denotes the change of radius affected by deflation. Since this equation is valid for driving situations with no tyre slip, $\lambda_i = 0$, and and a steering angle equal to zero, $\delta_f = 0$, the computation is activated only if these conditions are valid.

Since the variation of the tyre radius for low velocities is almost zero, the calculation is activated for a wheel speed above $1\,m/s$. Below this speed the last estimated effective
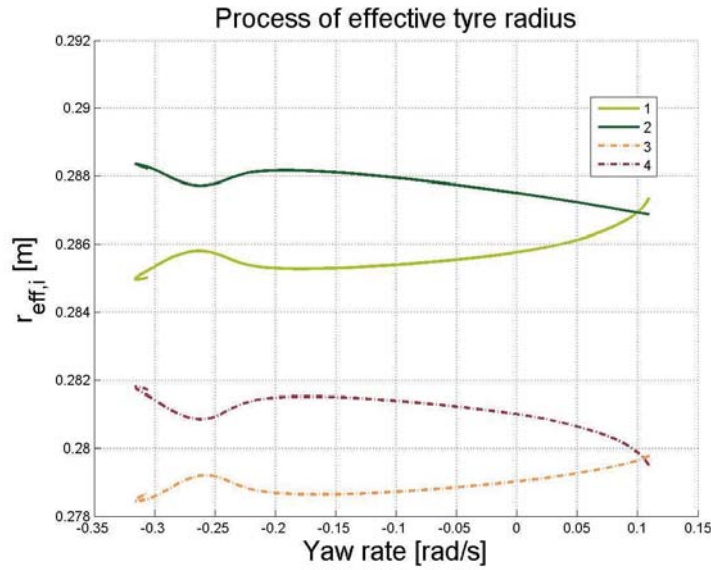
Figure 3.17: tyre radius over vehicle yaw rate

tyre radius is held. In order to avoid errors in the estimation the value of the effective tyre radius is limited to a range between $0.25\,m - 0.35\,m$.

3.5.2 Vehicle Mass

The variation of the vehicle mass, in general, has a potential of up to 40% and is strongly connected to the number of passengers, the payload and the amount of fuel. As an EV uses the high voltage battery as energy source, which has constant weight, the variation due to fuel is not relevant but still the variance can be up to 35%. Hence, the knowledge of the exact vehicle mass has benefits for the state estimation, the vehicle control and the energy management.

For the state prediction (see equation 3.86 and 3.88) and the estimation of the tyre forces (3.76-3.79) the feedback of the estimated mass improves the accuracy. The control algorithms of the implemented ADAS can use this parameter information for a more reliable computation of the moments that are needed for the desired vehicle motion. Moreover, infeasible brake or acceleration commands that might bring the vehicle in an unstable situation can be avoided. Finally, the energy management uses the vehicle mass to calculate the energy consumption estimation to the destination.

The vehicle mass estimation algorithms described in literature ([53], [12], [23], [8], [14]) are broadly classified on whether they are event-seeking or averaging. Since none of these algorithms satisfies the requirements of processing limitations, accuracy, speed of estimation, reliability, robustness, deviation and costs, a new kind of estimator was developed.

Here, an event-seeking estimator was designed that uses the results from the EKF al-

gorithm and and is therefore less susceptible for noise. The vehicle mass estimation is build of three subsystems: activation decision, mass estimation and logic decision, the latter discretising the estimated mass amongst others (see Fig. 3.18).
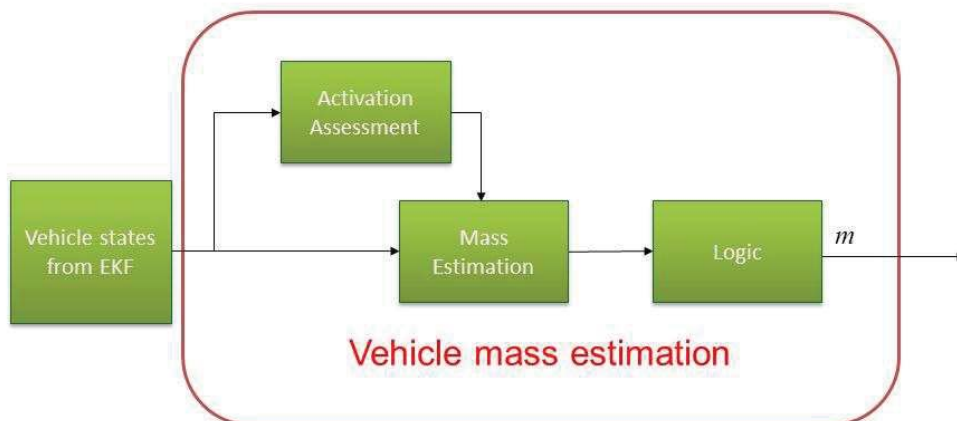
Figure 3.18: Structure of mass estimation

The activation assessment is a simple check if all conditions for the mass estimation are fulfilled. These conditions were evaluated empirically and restrict the activation to accelerating situations from standstill of the vehicle. The exact postulates for the activation check are listed in Tab. 3.9.

Condition	Sensor Unit
$|r| < 0.0175$	rad/s
$1 \leq a_x \leq 4$	m/s^2
$0.3 \leq v_x \leq 3.55$	m/s
$\lambda_i < 0.15$	$-$
$F_{x,1} > 400$	N
$F_{x,2} > 400$	N
$confidence = 1$	$-$

Table 3.9: Activation conditions for mass estimation

Through the activation decision the computation of the vehicle mass is only enabled whenever the activation decision was successfully executed. By this implementation, the mass estimator becomes the event seeking characteristic.

These defined conditions are checked with a sample time of $T_S = 10\,ms$ and the output of the activation assessment is Boolean. Whenever the output is true the mass estimation will be executed. The equation for the computation of the vehicle mass assumes

that there is no road slope and is given by:

$$\hat{m} = \frac{-F_{ext} + \sum_{i=1}^{4} F_{x,i}}{a_x} \tag{3.126}$$

Where F_{ext} are the external forces due to rolling resistance and aerodynamic drag which are computed by using empirical functions. Fig. 3.19 shows their contributions in different vehicle velocities. This figure indicates that at low speed, the rolling resistance, which remains almost constant over the whole velocity spectrum, becomes the dominant resistance force.
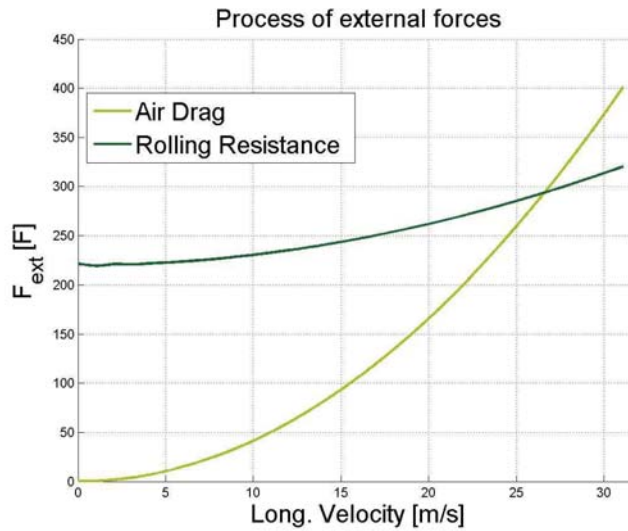
Figure 3.19: Process of the external forces

Finally, in the logic block three improvements for reliability, accuracy and robustness are implemented. Due to the aimed accuracy of $\pm 50\,kg$ the estimated mass is discretised in $50\,kg$ steps between the fixed minimum mass of $1300\,kg$ and the maximum presumed mass of $2250\,kg$. For a fast and reliable mass estimation at vehicle start-up the default vehicle mass of $1500\,kg$ is taken, as long as the mass estimation was not activated. Finally, the robustness of the mass estimation is increased by a time analysis of the evaluated mass. In detail, the estimated mass has to be constant for a time period of $1\,s$. Thus, the estimation is not susceptible for short influences of road banking/grade and unexpected aerodynamic forces.

3.5.3 Road Friction Coefficient

The estimation of the road friction coefficient has great impact on the control of a vehicle since the potential of tyre forces is limited to road conditions. Thereby, an accurate information of the road friction improves the safety and energy efficiency of a vehicle

by preventing motion requests that exceed the friction potential of the road surface and might lead to slipping wheels or an unstable vehicle.

Basically, the accuracy of the proposed road-friction coefficient estimation is determined by the tyre model. According to equations 3.80 until 3.82 there a two basic parameters which have great influence on the tyre forces: tyre longitudinal/lateral cornering stiffness C_x/C_y and the road friction coefficient μ. Whereas the cornering stiffness is characteristic for the tyre and is assumed to be constant, the road friction coefficient is variable and changes largely with road surface modifications.

The friction coefficient in general is the relation of the resulting friction force to the normal force F_N, where the consistency of friction has to be considered. For a given wheel, the normalized traction force, μ, is:

$$\mu_i = \frac{F_{res,i}}{F_N, i} = \frac{\sqrt{F_{x,i}^2 + F_{y,i}^2}}{F_{z,i}} \text{ for } i = 1, \ldots, 4. \tag{3.127}$$

For each wheel, μ_{max} is the maximum achievable value of $|\mu|$ that the presented approach estimates here. The friction coefficient, μ, at a tyre is related to the amount of slip at this tyre. The well-known model for this relationship is the presented "Magic-Formula" [51] which is used to generate the plots for traction and braking on four different road surfaces. In Fig. 3.20 it can be seen that μ is an increasing function of λ until a critical slip value, where μ reaches μ_{max} and then decreases.

Moreover, it is obvious that the friction slope is different for diverse road surfaces, that is defined as [31]:

$$M_i = \frac{d\mu_i}{d\lambda_i}|_{\mu=0}. \tag{3.128}$$

Whereas this equation is valid for even roads and small slip values.

Examples [36] for the maximum friction coefficient for a passenger car tyre 215/65 $R15$ and the according friction slope evaluated in simulation runs are given in the following table:

Road surface	Maximum friction coefficient μ_{max}	friction slope M
Dry asphalt	$0.8 - 0.9$	$45 - 50$
Dry concrete	$0.8 - 0.9$	$45 - 50$
Wet asphalt	$0.5 - 0.7$	$30 - 40$
Wet concrete	0.8	$35 - 45$
Gravel	0.6	35
Packed snow	0.2	7
Ice	0.1	2

Table 3.10: Average of maximum friction coefficients and friction slope
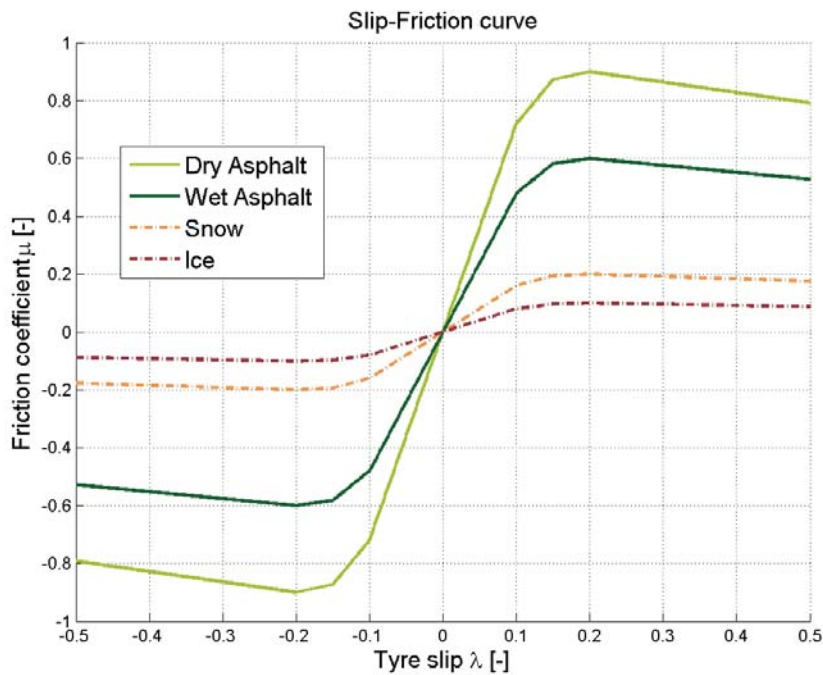
Figure 3.20: Friction coefficient over tyre slip

The phenomenon of friction has a big impact on the development of electromechanical systems since it occurs in nearly all interrelated motions where the surfaces of objects have contact to each other. For a prediction of the effects of friction on the system performance based on numeric simulations, dependable models are necessary.

But since the accuracy of the classic models was not sufficient enough and the complexity of the dynamic models was too high for implementation on the VHU or the convergence was not fast enough, a different concept was chosen for the implementation. This tyre-slip-based approach with Recursive Least Squares (RLS) will be presented in the next section.

RLS slip based estimation

A RLS concept was selected for the parameter identification that minimises a weighted linear least squares cost function related to the input signal. To find the parameter a and b a parameter vector is build, $\Theta^T = [a, b]$, and the functional of a residuum is minimised. This functional is defined as difference between the current output value $y(k)$ and the estimated model output $\hat{y}(k)$ that is based on the currently iterated parameters $\Theta(k)$. The iteration of the desired parameters is realised by application of the Gauss-Newton

algorithm in which the sum of the error squares should be minimised:

$$\sum (\hat{y}(k) - y(k))^2 \to min!. \tag{3.129}$$

The forgetting factor τ_{RLS} is introduced to assess the current data related to the past data. This factor with a range between 0 and 1 leads to exponential loss of memory from the past data. This fact has a high significance on the online identification of a time variable system since the influence of non representative values on the current model can be eliminated.

The complete RLS computation steps are given as follows [58]:

- Residuum $\Delta(k)$:
$$\Delta(k) = y(k) - \hat{y}(k) \tag{3.130}$$

- Priori estimation:
$$\hat{y}(k) = \Psi^T(k) \cdot \hat{\Theta}(k-1) \tag{3.131}$$

- Jacobi matrix of the residuum $\Delta(k)$ dependent on the parameter vector $\Theta(k)$:
$$\Psi(k) = \left[\frac{\partial \Delta(k)}{\partial a(k)} \cdot \frac{\partial \Delta(k)}{\partial b(k)} \right] \tag{3.132}$$

- Gain vector ρ for a simplified notation of the algorithm:
$$\rho(k) = \frac{P(k-1) \cdot \Psi(k)}{\Psi^T(k) \cdot P(k-1) \cdot \Psi(k) + \tau_{RLS}} \tag{3.133}$$

- Covariance matrix $P(k)$:
$$P(k) = \frac{1}{\tau_{RLS}} \left[P(k-1) - \rho(k) \cdot \Psi^T(k) \cdot P(k-1) \right] \tag{3.134}$$

- Estimation of parameters $\hat{\Theta}(k)$:
$$\hat{\Theta}(k) = \hat{\Theta}(k-1) + \rho(k) \cdot \Delta(k) \tag{3.135}$$

During this computation the matrix P will converge asymptotically to the error estimation covariance matrix of the identified parameters. Thereby, a static criteria for the validity of most scenarios is represented.

A common approach for the initialisation is $\hat{\Theta}(k_0) = 0$ for the parameter estimation and $P(k_0) = C \cdot I$ for the covariance matrix, where C is constant and $I = dim\Theta$ is the identity matrix [58]. Here, a big value of C implies that the reliance on $\hat{\Theta}(k_0)$ is very low and leads to a high adaptivity rate.

The overview of the complete RLS algorithm is given in Fig. 3.21:

To enable a linear estimation with the RLS concept the current longitudinal tyre slip $\hat{\lambda}_i$
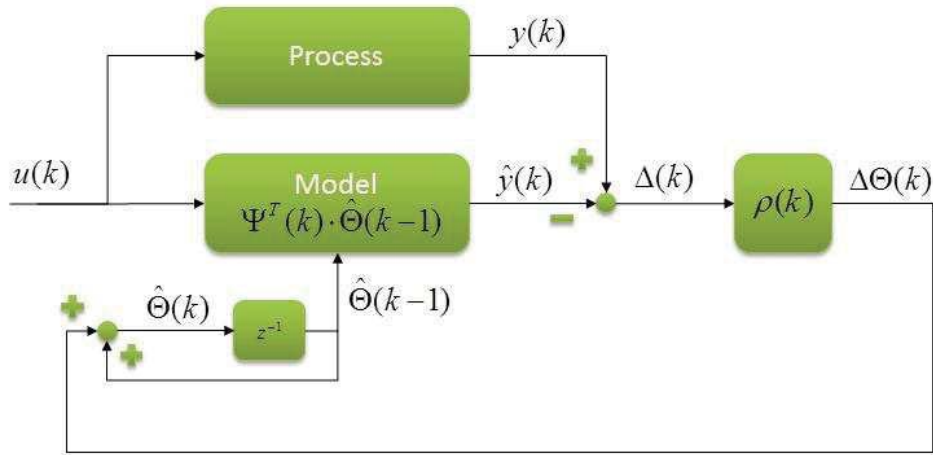
Figure 3.21: Structure of the RLS algorithm

is defined as input and computed according to 3.74 and 3.75:

$$u_i(k) = \hat{\lambda}_i(k) \text{ for } i = 1, \ldots, 4. \tag{3.136}$$

Generally, the maximum friction coefficient and friction slope M have a positive correlation and the relationship can be simplified as a curve obtained through interpolation of Table 3.10. The measurement input $y(k)$, which is the maximum friction coefficient based on the friction slope, when using 3.127 and 3.128 is then defined as:

$$y(k) = \mu_{max}(M). \tag{3.137}$$

For the estimation of the maximum friction coefficient a friction model has to be used. There exist several friction models that are fine for a rough identification of the friction coefficient based on observable in- and outputs. A comparatively recent published model is the LuGre-model [18], named after their designer at universities Lund and Grenoble. This model is able to simulate the bulk of observed friction effects without distinguishing a special case for the standstill. The friction is seen as resistance force of a bristle which describes the aggregated state of all bristles. Here, a longitudinal tyre slip, λ, based approach is chosen according to:

$$\hat{y}(k) = \frac{\mu'(0) \cdot \lambda}{1 + a \cdot \lambda + b \cdot \lambda^2}. \tag{3.138}$$

The initial gradient $\mu'(0)$ is constant for almost all road conditions and has a value of 30. The current road friction coefficient is then a function of the longitudinal tyre slip and the parameters a and b. As the number of the unknown parameter is two the identification of the model is relatively easy.
This model represents the relation between the road friction coefficient μ and the current

longitudinal tyre slip λ and, thereby, enables the linear estimation of the parameters a and b. The accuracy of this approach is dependent on the tyre slip and the method to estimate the parameter.

3.6 Stability Assessment

The vehicle observer computes stability limits to guarantee the stability of the vehicle and an optimal use of the propulsion torque. With these limits, the DU1 restricts motion requests, either from the driver or from ADAS that exceed the stability limits.

In detail, the maximum longitudinal acceleration and the minimum curvature are calculated based on the circle of forces [51] by the use of the longitudinal velocity $\hat{v}_x$ and the maximum road friction coefficient $\hat{\mu}_{max}$.

The absolute maximum longitudinal acceleration a_x^{max} for braking and acceleration is computed by [57]:

$$a_x^{max} = \frac{1}{4} \cdot g \cdot \sum_{i=1}^{4} \hat{\mu}_{max,i}. \tag{3.139}$$

The absolute minimum curvature γ for left and right bends is calculated with:

$$\gamma^{min} = \frac{1}{4 \cdot v_x^2} \cdot g \cdot \sum_{i=1}^{4} \hat{\mu}_{max,i} = a_x^{max} \cdot \frac{1}{v_x^2}. \tag{3.140}$$
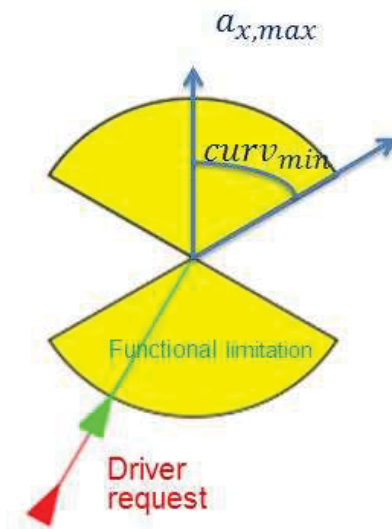
Figure 3.22: Limitation of driver request

In both upper equations the average of the four estimated maximum friction coefficients

is computed, to get one value for each limit.

An example of the functionality of the stability assessment is shown in Fig. 3.22. Here, the yellow area represents the zone in which the motion requests are stable. The driver, symbolized by the red arrow, wants to brake with a mild left steering but as the braking would exceed the stability zone, the driver request is restricted by the functional limitation, which is symbolized by the green arrow.

3.7 Trip Computation

The calculation of the driven distance is needed as information for the driver and displayed in the instrument cluster of the vehicle. On the one hand there is the odometer value of the driven distance over vehicle lifetime and on the other hand there is the tripmeter value which can be reset by the driver at any time. The signal request to reset this value is transmitted by the HMI software. Physically, the driver pushes a button in the instrument cluster.

The calculation for odometer s_o and tripmeter s_t is very simple as the longitudinal velocity is integrated by:

$$s_{o,k} = s_{o,k-1} + \hat{v}_{x,k} \cdot \Delta T \cdot 0.001, \tag{3.141}$$

$$s_{t,k} = s_{t,k-1} + \hat{v}_{x,k} \cdot \Delta T \cdot 0.01. \tag{3.142}$$

The difference in the last factor of the computations is based on the desired accuracy. The odometer needs an accuracy of $1\,km$ whereas the tripmeter is more accurate with a resolution of $0.1\,km$.

4 Markov Chains for signal replacement

As the performance of the presented vehicle observer depends highly on the sensor signals, a concept for the handling of delayed or missing sensor signals is introduced in this chapter. By the use of the Markov Chain method missing sensor information is estimated and transmitted to the vehicle observer algorithm. Thereby, the concept increases the robustness to sensor failures and, moreover, has an augmented safety for the passenger in the vehicle.

Firstly, the problem of delayed or missing sensor signals is explained. Afterwards, the method of Markov Chains is introduced. An overview of the build up and functionality is given in section 4.3, the calculation of the initial distribution is presented in section 4.4 and the design of the transition matrices is shown in section 4.5. Finally, the computation of the state of the Markov Chain is given.

4.1 Problem of Delayed or Missing Sensor Signals

Where sensor signal drop-outs or delays have been more or less neglected in past vehicle control architectures since the driver requests had the highest priority for the actuator commands, the increased amount of electronics in vehicle control makes new demands to this issue. By the augmented electric vehicle control, the safety, comfort and efficiency of the entire car is improved and the driver is relieved by a system take-over of vehicle control for an increased number of manoeuvres. Thus, the trend to raise the grade of automation gradually leads from a vehicle merely controlled by the driver to a vehicle which is driven autonomously. Current forecasts estimate autonomous driving on highways for the year 2025.

By the rising grade of automation the importance of reliable sensor signals is increasing as well because the performance of ADAS control algorithms are dependent on them. This means that wrong, delayed or missing sensor information can lead to a degraded automation state or bring the vehicle in an unstable state. In both cases, the safety of the passengers is no longer guaranteed. A fact, that calls for new interception concepts. Moreover, there is a paradigm shift in the type of operation since in the past, the specification was to have a fail-safe operation, which means that the control should either control everything and work perfectly or should not engage at all. For highly automated or autonomous driving the requirement for the control operation is to perform fail-tolerant in every situation. Therefore, any failure should be compensated to guarantee at least a degraded mode where the control is able to operate with limited performance or to maintain a state of safety without endangering other road users.

For instance, there will be a defined time slot for the transition phase from autonomous driving mode to driver vehicle control in case of a detected failure that limits the vehicle

performance. The autonomous driving will switch to a limp home mode, try to enter a safe spot and the passengers are informed to take over the vehicle control. Yet the length of this time slot is not fixed by law. The vehicle control has to guarantee this safe vehicle mode and, thereby, relies on the provided sensor information. Currently, Original Equipment Manufacturer (OEM) tend towards a transfer time between $5 - 10\,s$ for highly automated driving and a transfer time longer than $10\,s$ for autonomous driving [32].

4.2 Introduction to Markov Chains

In this section, a general explanation and the basic properties of Markov Chains method are introduced. In 1907, Andrei A. Markov began the study of an important new type of change process. In this concept the outcome of a given experiment can affect the outcome of the next experiment. This type of stochastic process is called Markov Chain [29]. The most specific characteristic of Markov Chains is that they are memoryless: the next state depends only on the current state and not on the sequence of events that preceded it. In general, Markov Chains are applicable in discrete and continuous time. As the target hardware is a micro-controller with discrete sample time we focus on the discrete time method.

The assumption for discrete-time Markov Chains [49] is the definition of a limited set of possible states, the bounded state space I. The process starts in one single state $i \in I$ and changes over time. More precisely, we assume a finite state space with $I = \{1, 2, \cdots, l\}$ where $l \in N = \{1, 2, \cdots\}$ is an arbitrary but specified natural number. For every state $i \in I$ the probability χ that the considered system at instant of time $n = 0$ is in state i is given by:

$$0 \leq \chi_i \leq 1, \text{ with} \sum_{i=1}^{l} \chi_i = 1. \tag{4.1}$$

The vector $\chi = (\chi_1, \cdots, \chi_l)^T$ of all single probabilities $\chi_1, \cdots, \chi_l$ forms the initial distribution of the Markov Chain. Similar to the initial distribution there is a probability $p_{i,j}$ that the system state changes from state i directly to state j. As this probability exists for every pair of states $i, j \in I$ a $l \times l$ matrix can be built. This matrix is called the transition matrix $P = (p_{ij})_{i,j=1,\cdots,l}$ and is given by:

$$p_{i,j} \geq 0, \text{ with} \sum_{j=1}^{l} p_{i,j} = 1. \tag{4.2}$$

For every quantity $I = \{1, 2, \ldots, l\}$ and for every vector $\chi = (\chi_1, \ldots, \chi_l)^T$ there is a respective matrix $P = (p_{ij})$, that fulfils the requirements (4.1) and (4.2). The Markov Chain can be defined as follows:

- Unless $X_0, X_1, \ldots : \Omega \to I$ is a series of stochastic variables that are defined

in the same state space (Ω, F, P) and they take their value out of the quantity $I = \{1, 2, \ldots, l\}$.

- Then $X_0, X_1, \ldots$ is called a homogeneous Markov Chain with the initial distribution $\chi = (\chi_1, \ldots, \chi_l)^T$ and the transition matrix $P = (p_{ij})$, if (4.3) is valid for arbitrary $n = 1, 2, \ldots$ and $i_0, i_1, \ldots, i_n \in I$.

$$P(X_0 = i_0, X_1 = i_1, \ldots, X_n = i_n) = \chi_{i_0} p_{i_0 i_1} \ldots p_{i_{n-1} i_n} \tag{4.3}$$

Moreover, the following points have to be considered:

- A quadratic matrix $P = (p_{ij})$ that fulfills (4.2) is called stochastic matrix.

- With the following definition the meaning of the intuitive equation (4.3) is pointed out, especially the notation of initial distribution and transition matrix.

Theorem 2.1

The series X_n of arbitrary values from I is called a Markov chain if there exists a stochastic matrix $P = p_{ij}$, so that

$$P(X_n = i_n | X_{n-1} = i_{n-1}, \ldots, X_0 = i_0) = p_{i_{n-1} i_n} \tag{4.4}$$

for any $n = 1, 2, \ldots$ and $i_0, i_1, \ldots, i_n \in I$ with $P(X_{n-1} = i_{n-1}, \ldots, X_0 = i_0) > 0$.
The proof is given by the assumption that $(X_n)_{0 \le n \le N}$ is Markov (χ, P), then

$$\begin{aligned} P(X_0 &= i_0, X_1 = i_1, \ldots, X_N = i_N) \\ &= P(X_0 = i_0) P(X_1 = i_1 | X_0 = i_0) \; \cdots \; P(X_N = i_N | X_0 = i_0, \ldots, X_{N-1} = i_{N-1}) \\ &= \chi_{i_0} p_{i_0 i_1} \ldots p_{i_{N-1} i_N}. \end{aligned} \tag{4.5}$$

On the other hand, if (4.3) holds for N, then the summation of both sides over $i_n \in I$ and using $\sum_{j \in I} p_{ij} = 1$ it is obvious that (4.3) holds for $N - 1$ and, by induction

$$P(X_0 = i_0, X_1 = i_1, \ldots, X_n = i_n) = \chi_{i_0} p_{i_0 i_1} \ldots p_{i_{n-1} i_n} \tag{4.6}$$

for all $n = 0, 1, \ldots, N$. In particular, $P(X_0 = i_0) = \chi_{i_0}$ and, for $n = 0, 1, \ldots, N - 1$ equation (4.5) is valid. So $(X_n)_{0 \le n \le N}$ is Markov (χ, P).
The next result confirms the basic Markov property: the memoryless characteristic. $\gamma_i = (\gamma_{ij} : j \in I)$ is for the unit mass at i, where

$$\gamma_{ij} = \begin{cases} 1, & \text{if } i = j \\ 0, & \text{otherwise .} \end{cases} \tag{4.7}$$

Theorem 2.2

Let $(X_n)_{n \ge 0}$ be Markov (χ, P). Then, conditional on $X_m = i$, $(X_{m+n})_{n \ge 0})$ is Markov (γ_i, P) and is independent of the random variables $X_0, \ldots, X_m$.
The proof is produced by the random event A determined by $X_0, \ldots, X_m$ that conducts

to

$$P(\{X_m = i_m, \ldots, X_{m+n} = i_{m+n}\} \cap A | X_m = i)$$
$$= \gamma_{ii_m} p_{i_m i_{m+1}} \cdots p_{i_{m+n-1} i_{m+n}} P(A | X_m = i) \tag{4.8}$$

then the result follows by theorem 2.1. First, consider the case of elementary events

$$A = \{X_0 = i_0, \ldots, X_m = i_m\}. \tag{4.9}$$

In that case it has to be shown

$$P(X_0 = i_0, \ldots, X_{m+n} = i_{m+n} \text{ and } i = i_m / P(X_m = i))$$
$$= \gamma_{ii_m} p_{i_m i_{m+1}} \cdots p_{i_{m+n-1} i_{m+n}} P(X_0 = i_0, \ldots, X_m = i_m \text{ and } i = i_m) / P(X_m = i) \tag{4.10}$$

which is true by theorem 2.1. In general, any event A determined by $X_0, \ldots, X_m$ may be written as a countable disjoint union of elementary events

$$A = \bigcup_{k=1}^{\infty} A_k. \tag{4.11}$$

The desired identity (4.8) for A follows by summing up the corresponding identities for A_k.

In order to calculate the probability that after n steps of the Markov Chain the system is in a given state, we regard distributions and measures χ as row vectors whose components are indexed by I, just as P is a matrix whose entries are indexed by $I \times I$. When I is finite, the states are labelled $1, 2, \ldots, N$. Consequently, χ will be an N-vector and P an $N \times N$-matrix. For these objects, matrix multiplication is a familiar operation. The matrix multiplication is extended to the general case with definition of a new measure χP and a new matrix P^2 by

$$(\chi P)_j = \sum_{i \in I} \chi_i p_{ij}, \quad (P^2)_{ik} = \sum_{j \in I} p_{ij} p_{jk}. \tag{4.12}$$

Similarly, the definition of P^n is done for any n. The first transition matrix P^0 is the identity matrix I, where $(I)_{ij} = \gamma_{ij}$. The context will make it clear when I refers to the state space and when to the identity matrix. The diction for the (i, j) entry in P^n is established as $p_{ij}^{(n)} = (P^n)_{ij}$.

In the case where $\chi_i > 0$ it is written $P_i(A)$ for the conditional probability $P(A | X_0 = i)$. By the Markov property at time $m = 0$, under P_i, $(X_n)_{n \geq 0}$ is Markov (γ_i, P). Thus, the behaviour of $(X_n)_{n \geq 0}$ under P_i does not depend on χ.

Theorem 2.3

Let $(X_n)_{n \geq 0}$ be Markov (χ, P). Then, for all $n, m \geq 0$,

1. $P(X_n = j) = (\chi P^n)_j)$

2. $P_i(X_n = j) = P(X_{n+m} = j | X_m = i) = p_{ij}^{(n)}$

The proof for the first point is given by theorem 2.1:

$$
\begin{aligned}
P(X_n = j) &= \sum_{i_0 \in I} \cdots \sum_{i_{n-1} \in I} P(X_0 = i_0, \ldots, X_{n-1} = i_{n-1}, X_n = j) \\
&= \sum_{i_0 \in I} \cdots \sum_{i_{n-1} \in I} \alpha_{i_0} p_{i_0 i_1} \ldots p_{i_{n-1} j} = (\alpha P^n)_j
\end{aligned}
\tag{4.13}
$$

The second proof is produced by Markov property, conditional on $X_m = i, (X_{m+n})_{n \geq 0}$ is Markov (γ_i, P), so $\chi = \gamma_i$ is set in 1.

In light of this, theorem $p_{ij}^{(n)}$ is the n-step transition probability from i to j.

4.3 Buildup and functionality

The error correction mechanisms are based on the analysis of the sensor signals by the error detection algorithm (3.3.2). The Markov Chain algorithm will only be executed whenever a sensor signal is detected either as delayed or missing. In order to reduce the computational effort there are several different subsystems containing a specific algorithm of the Markov Chain method. Only one of them will be activated, depending on the information of missing or delayed signals reported by the error detection mechanisms (see Fig. 4.1).
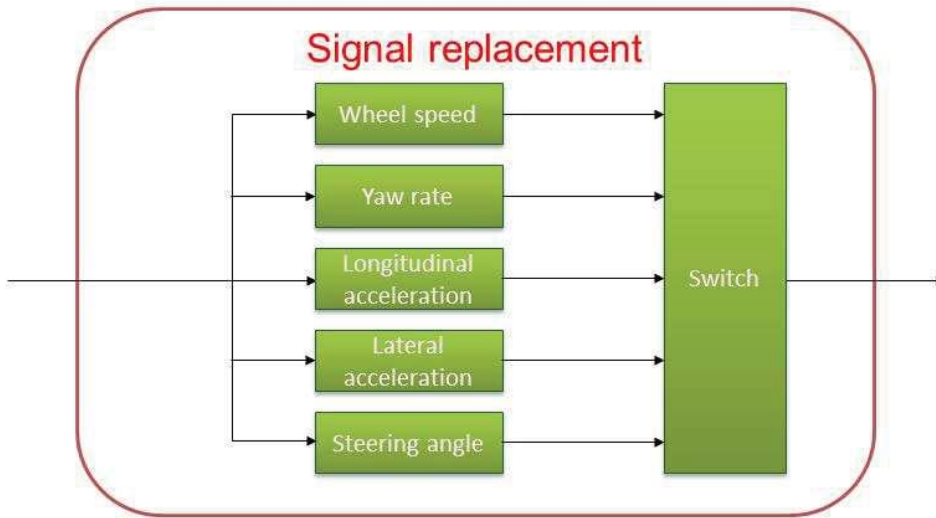
Figure 4.1: Structure of the signal replacement

For example, the wheel speed subsystem will be enabled whenever the error detection mechanisms detect a delayed or missing wheel speed signal. The signal bus entering the signal replacement subsystem contains the measured sensor signals as well as the results from the error detection mechanisms. Here, the Markov Chain concept replaces

the delayed or missing sensor signals based on the still available sensor signals and the last measured value of the specific signal. The following output signals are transmitted to the presented vehicle observer: the four wheel speeds, the yaw rate, longitudinal and lateral acceleration and the steering angle.

Each of the subsystems is build by two subsystems itself - the calculation of the input signals for the Markov Chain and the Markov Chain function. In the first subsystem the last measured sensor signal is held, the gradient of the last available sensor signals is calculated and the tendency for a state change is computed. In the Markov function the confidence is calculated and the Markov Chain state for the delayed or missing sensor signal is estimated. Here, the computation of the initial distribution, the Markov Chain algorithm and the final state calculation are carried out. The generic structure for all signal replacement subsystems using the Markov Chain concept is given in Fig. 4.2.
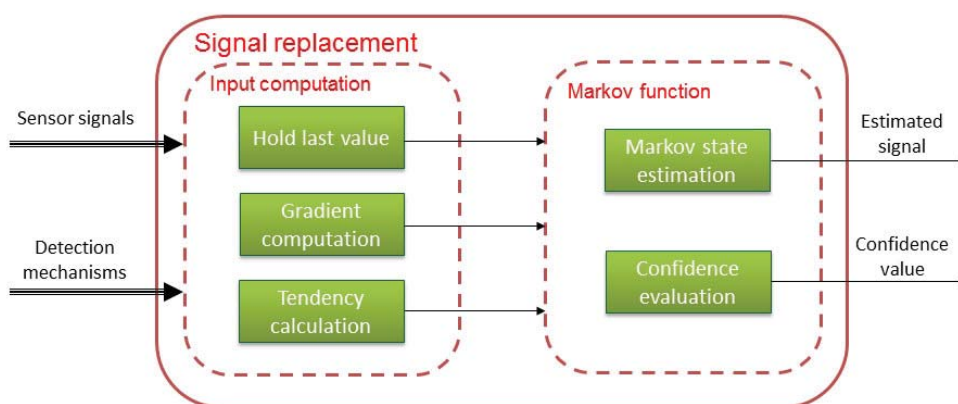
Figure 4.2: Generic structure of one signal replacement subsystem

4.4 Calculation of initial distribution

The initial distribution for each Markov Chain is based on the last available measurement from the sensor with malfunction and the current values from the remaining available sensor signals. First of all, the range for the specific sensor has to be discretised with a fixed number of states i. Thus the vector for the initial distribution u has a dimension of $1 \times i$. As the last measurement represents the basis for the initial distribution, the current measurements are taken to estimate the probabilities for the surrounding states. In particular, the first initial distribution of the last measured state i is set to 0.5. The remaining 0.5 are allocated by calculating the distributions on the basis of the current measurements where every subsystem has its own equations. In the second time step the estimated state is seen as reference measurement and the probability of it is set to 0.5. Hence, the computation of the initial distribution is an ongoing process and, thereby, executed online. Moreover all computations that are belonging to the initial distribution

are calculated without any dimensions.

The detailed equations for every subsystem will be given in the following subsections. In general, the maximum gradients σ_u for each signal u are compared to the defined interval Δu and, thus, the number of states m that may have an initial distribution greater than zero is calculated by $m = \frac{\sigma_u}{\Delta u}$. The tendency towards which direction of the last measured state the next state will tend is determined by comparison to thresholds for the gradients of the specific measurement. These threshold values were evaluated empirically in simulations with highly dynamical manoeuvres and were verified by outcomes of recorded data from real test drives. If the gradients cross this certain threshold, only the distribution of the m states to the left and accordingly right side of the last measured state are upgraded. In case no threshold is crossed, the remaining 0.5 are allocated equal to the $m/2$ entries to each side. The sum to add for each entry is calculated by $d_u = \frac{0.5}{m}$. Moreover, an adjacent tendency value ζ based on the available sensor signals that give additional information for the direction and the dimension of state changes of the currently missing or delayed sensor signal is computed. In each subsystem either the signals that are directly linked to the missing sensor signals or information about the current process can be derived from it. Here, easy equations that represent the connections between the different sensor signals are derived. The results are standardised and limited to enable an easy adjustment for the Markov Chain state estimation algorithm, especially the design of the initial distribution.

After the buildup and the functionality were introduced shortly, the detailed description of the calculation of the initial distribution is given in the next subsections starting with the equations for the absence of one of the four wheel speed sensors. As the holding of the last measured sensor signal and the computation of the gradient are simple equations and are the same for all subsystems, these sub functions are not explained here.

4.4.1 Wheel speed

As stated above first of all the range for the wheel speed sensor $[0 - 2551/pm]$ has to be discretised for the initial distribution vector u_ω with a length of 101 entries. This means, that every entry in the vector represents an wheel speed according to:

$$u_{\omega,i} \equiv \omega_{j,max}/101 \cdot (i - 1), \tag{4.14}$$

where j represents the wheel number.

Since the wheel speed sensor is the only one equipped on the vehicle that can been seen as a redundant sensor since there is a sensor for each of the four wheels, an additional computation was implemented for the absence of a wheel speed sensor signal in the calculation of the initial distribution. In detail, the mean wheel speed of the three remaining sensor signals is computed to get more information about the process of the missing sensor signal. The advantage of taking all available wheel speeds is that the speed of spinning wheels on the driven front-axle and shortly blocked wheels during

braking is almost compensated by the mean. So the mean wheel speed is computed by:

$$\omega_{mean}(k) = \frac{1}{3} \cdot \sum_{j=1}^{3} \omega_j(k), \tag{4.15}$$

where the index $j = [1 - 3]$ represents the current measurements of the available wheel speeds.

The adjacent tendency value for the direction and dimension of the state process is calculated by:

$$\zeta(k) = \omega_{mean}(k) - \omega_j(k_0), \tag{4.16}$$

where $\omega_j(k_0)$ is the last received sensor signal.

Now, the last measured signal $\omega_j(k_0)$, the derivative $\dot{\omega}_j(k_0) = \frac{\Delta\omega}{T} = \frac{\omega_j(k) - \omega_j(k-1)}{T}$ with T as sample time, the mean wheel speed ω_{mean} and the adjacent tendency ζ value are transmitted to the Markov function. In the calculation of the initial distribution 4.1, the basic index i_0 for the design of the vector u_{ω_i} is computed by

$$i_0(k) = \left\lfloor \left(\frac{\omega_j(k_0)}{\sigma_u} \right) \right\rceil, \tag{4.17}$$

where $\lfloor \rceil$ are the Gaussian brackets and represent the nearest integer to $\left(\frac{\omega_j(k_0)}{\sigma_u} \right)$.

To consider the adjacent tendency value ζ an auxiliary variable m is calculated by:

$$m(k) = sign(\zeta(k)) \cdot \left\lfloor \left| \left(\frac{\zeta(k)}{\zeta_{lim}} \right) \right| \right\rfloor, \tag{4.18}$$

where ζ_{lim} is the value to standardise the adjacent value and $\lfloor \rfloor$ are the Gaussian brackets and represent the largest integer less than or equal to $\left| \left(\frac{\zeta(k)}{\zeta_{lim}} \right) \right|$. Finally, the base index i_{base} is built by the sum of the basic index i_0 and the auxiliary variable m:

$$i_{base}(k) = i_0(k) + m(k). \tag{4.19}$$

Afterwards, this base index i_{base} is set to 0.5 in the vector of the initial distribution:

$$u_{\omega,i}(1, i_{base}) = 0.5. \tag{4.20}$$

After the base index value in the initial distribution vector is set, the remaining 0.5 according to 4.1 are logically distributed. This is done by the consideration of the maximum gradients σ_u and special rules when the base index reaches one limit of the defined state space. This logic for the different cases is given in the following table:

This table is also valid for the configuration of all the other initial distributions. After the composition of the initial distribution for a missing wheel speed sensor signal was introduced now this is done for the yaw rate.

Condition	Distribution
$(i_{base} == i_{min}) \,\&\& \,(\dot{\omega}_i(k_0) < -\sigma)$	$u_{\omega,i}(1, i_{base}) = 1$
$(i_{base} == i_{max}) \,\&\& \,(\dot{\omega}_i(k_0) > \sigma)$	$u_{\omega,i}(1, i_{base}) = 1$
$(\dot{\omega}_i(k_0) > \sigma) \,||\, (i_{base} == i_{min})$	$u_{\omega,i}(1, i_{base+1}) = 0.5$
$(\dot{\omega}_i(k_0) < -\sigma) \,||\, (i_{base} == i_{max})$	$u_{\omega,i}(1, i_{base-1}) = 0.5$
else (default)	$u_{\omega,i}(1, i_{base-1}) = 0.25 \,\&\& \,u_{\omega,i}(1, i_{base+1}) = 0.25$

Table 4.1: Distribution rules for initial distribution vector

4.4.2 Yaw rate

In the input calculation for the initial distribution of the yaw rate and all following subsystems, the equation of the adjacent tendency will be given only as the remaining operations in this system do not change.

As the wheel speeds give an approximate account of the yaw rate, see [21], all wheel speeds are considered for the evaluation of the adjacent tendency. Let us assume the prior adjacent tendency ζ^* as:

$$\zeta^*(k) = (\omega_2(k) - \omega_1(k)) \cdot 0.2 + (\omega_4(k) - \omega_3(k))\,. \tag{4.21}$$

Here, the difference of the front axle is included with a fifth of it since slippery or blocking wheels on this driven axle might disturb the computation results.

Moreover, as the lateral acceleration a_y influences the yaw rate as well, the rate of change of this measured signal is also taken into account. To face the problem of inaccurate sensor signals and the dynamics of the vehicle, the derivative of the prior adjacent tendency and the lateral acceleration are taken into consideration in the final adjacent tendency calculation:

$$\begin{aligned} \zeta(k) &= \dot{\zeta}^* \cdot 0.5 - \dot{a}_y \\ &= (\zeta^*(k) - \zeta^*(k-1)) \cdot 0.5 - (a_y(k) - a_y(k-1))\,. \end{aligned} \tag{4.22}$$

Similar to the input calculation subsystem, in the Markov function subsystems all calculations are the same except those of the auxiliary variable m and the base index i_{base}. Where the equation for the variable auxiliary changes for every subsystem since the synchronisation, the base index changes only because the wheel speed signal is unsigned and the other measured sensor signals are signed. Thus, the calculation of the index for the last measured sensor signal in the defined state space system requires an offset value that has to be added in order to begin at the zero value.

The auxiliary value for the estimation of the yaw rate is computed with:

$$m(k) = sign(\zeta(k)) \cdot \left[\left(\left| \left(\frac{\zeta(k)}{\zeta_{lim}} \right) \right| \right) \right], \tag{4.23}$$

where for each subsystem different limiting adjacent values ζ_{lim} are valid and given in Tab. 4.2.

As stated above, the base index changes by adding an offset, here half of the state space 101:

$$i_{base}(k) = i_0 + 101 + m(k). \tag{4.24}$$

4.4.3 Longitudinal acceleration

As the longitudinal acceleration is very important for the implemented ADAS control algorithms, the estimation by Markov Chain methodology during sensor signal delay or absence has to be designed very carefully. Compared to the previous introduced subsystem, only the computation of the adjacent tendency value differs.

Again, the wheel speeds give information about the process of the longitudinal acceleration but due to the sensor signal resolution and occurring wheel slip all wheel speeds are considered to design the initial distribution. So the prior adjacent value is:

$$\zeta_i^*(k) = (\omega_i(k) - \omega_i(k-1)) \ \text{ with } i = (1, \cdots, 4), \tag{4.25}$$

where in contrast to equation 4.21 the front and rear wheel speeds are included equally since the influence of high wheel slip showed no big effect on the results during simulation. To solve the problem of high oscillation during low differences between wheel speeds at following time steps, the prior adjacent value is derived again and the mean of these four results is computed:

$$\zeta(k) = \frac{1}{4} \left(\sum_{i=1}^{4} \zeta_i^*(k) - \zeta_i^*(k-1) \right). \tag{4.26}$$

The remaining equations in the Markov function subsystem are exactly the same as for the calculation of the initial distribution of the yaw rate.

4.4.4 Lateral acceleration

In the input computation subsystem an additional operation was included in the design of the initial distribution for the lateral acceleration a_y. To identify the current lateral acceleration the derivative of a crosswise wheel pair is considered. This is done since the direction of the lateral acceleration is directly linked to the wheel speed process of the left and the right side. Here, the front left and rear right wheel speeds were taken into account but any other combination of left and right tire speed would be fine as well. Hence, the priori adjacent value of the current lateral acceleration is determined by:

$$\zeta^*(k) = \frac{(\omega_1(k) - \omega_4(k)) - (\omega_1(k-1) - \omega_4(k-1))}{T}. \tag{4.27}$$

The adjacent tendency value for the lateral acceleration is extended by a logical check since there is no influence of the wheel speeds, so the priori tendency value ζ^*, on the lateral acceleration as long as the steering angle or the yaw rate of the vehicle are close to zero. This is valid for the assumption that the road conditions, here friction and

inclination, are in a normal zone. In detail, the influence is cancelled out if the steering angle is $\delta < \pm 0.01 rad$ or the yaw rate is $r < \pm 0.01 rad/s$.

As the yaw rate is a good indicator for the process of the lateral acceleration and, thereby, for the real vehicle lateral movement, it has more significance for the calculation than the wheel speeds. Moreover, the steering activity has not been incorporated since during standstill or high wheel slip this may lead to false results. The final adjacent tendency value is computed by:

$$\zeta(k) = \begin{cases} -\left(\frac{r(k)-r(k-1)}{T}\right), & \text{if } ((\delta < \pm 0.01) \,||\, (r < \pm 0.01)) \\ \zeta^*(k) \cdot \frac{1}{200} - \left(\frac{r(k)-r(k-1)}{T}\right), & \text{if } ((\delta \geq \pm 0.01) \,||\, (r \geq \pm 0.01)). \end{cases} \tag{4.28}$$

The rest of the equations in the calculation of the initial distribution are exactly the same as for the yaw rate computation.

4.4.5 Steering angle

The steering angle of the vehicle is not only the most important signal for the correct functionality of the vehicle observer and the correct execution of the ADAS functions, it is as well the one which is hardest to estimate when the sensor or the network has a failure. As stated before, the actual steering angle might be totally independent of the other measured vehicle states such as yaw rate or lateral acceleration due to slippery road or road inclination.

During analysis of the steering angle in dynamic and normal driving situations it turned out that most reliable information of the process can be extracted from the difference of the front wheel speeds and the yaw rate. To enable an individual handling of both signals in the design of the initial distribution, the priori adjacent is formed as a vector:

$$\zeta^*(k) = (\omega_2(k) - \omega_1(k), r(k))^T. \tag{4.29}$$

For the evaluation of the adjacent tendency vector, an ongoing comparison of the current sensor signals to the one when the signal loss of the steering angle sensor occurred is implemented. Therefore, the final adjacent tendency vector is computed by:

$$\zeta(k) = (\zeta^*(k) - \zeta^*(k_0)). \tag{4.30}$$

In the composition of the initial distribution exist two auxiliary variables m and n which are calculated with:

$$\begin{pmatrix} m \\ n \end{pmatrix}(k) = sign\begin{pmatrix} \zeta_\omega(k) \\ \zeta_r(k) \end{pmatrix} \cdot \left\lfloor \left(\left| \left| \begin{pmatrix} \zeta_\omega(k)/\zeta_{\omega,lim} \\ \zeta_r(k)/\zeta_{r,lim} \end{pmatrix} \right| \right| \right) \right\rfloor. \tag{4.31}$$

Finally, the table of the maximum gradient values σ, that were evaluated by empirical work for each sensor signal with recorded measurements of the prototype vehicle, and the adjacent tendency limits ζ are shown in Tab. 4.2. These values base on the general sample time for the entire vehicle observer with $T_s = 10ms$.

Signal	σ	ζ
ω_i	2	1
r	0.171	5
a_x	0.5	0.007
a_y	50	0.2
δ	0.002	$\binom{0.007}{0.04}$

Table 4.2: Limit value for gradient and adjacent tendency

A short explanation of the outliers in this table should be given here. On the one hand the maximum gradient value for the lateral acceleration results from the high dynamic driving manoeuvres. On the other hand the high adjacent tendency value follows from the addition of the wheel speeds as well as from lateral acceleration during high dynamic driving scenarios.

4.5 Design of transition matrices

The first important task when designing the transition matrices for the Markov Chains is the definition of the bounded state space. As the ranges of the respective sensors are known by their data sheet, the task is to find a good agreement between the wanted accuracy and the restriction of computational effort. In Tab. 4.3 the empirically gathered values for the equal spaced interval Δu, the range given by the data sheet and the arising length of the state space l, which showed good performance, are listed. Hence, each transition matrix P has the size $l \times l$.

	Δu	range	l	unit
ω_i	2.5	$0 - 250$	101	rad/s
r	0.02895	± 2.895	201	rad/s
a_x	0.177	± 17.70	201	m/s^2
a_y	0.177	± 17.70	201	m/s^2
δ	0.005547	± 0.5547	201	rad

Table 4.3: Discretisation of signals

Similar to the calculation of the initial distribution, the row entries of the transition matrices are calculated. The most important differences are that the current measurements are neglected and the calculation of the entries is done offline. Therefore, the transition matrices are static and the Markov Chain is called a homogeneous one. At the beginning, the maximum number of possible state changes for each signal is taken into account by using the current gradient and the remaining sensor signals. In a second

step the static distribution vector is built where the probability values are concentrated around the current state entry which results in a binomial distribution is done. An example of the probability values for an even and uneven distribution vector is given in the following picture.
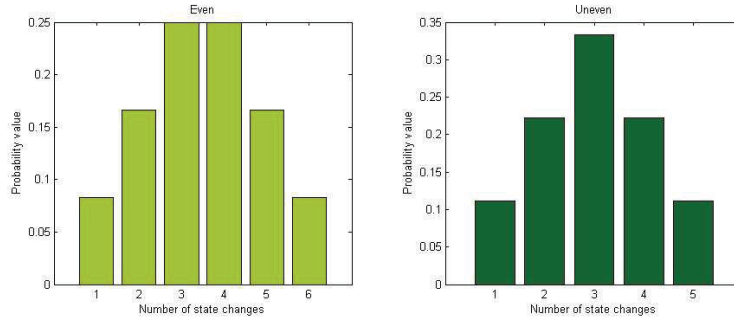
Figure 4.3: Binomial distribution of probability values for even and uneven case

The computation for each row j is done by incrementing the starting index for the distribution vector. Here, special rules for the distribution at the outer limits were integrated so that the sum of each row is equal to 1 like as defined in eq. 4.2. In fact, the distribution values are lowered from the current state space entry.

4.6 Computation of Markov Chain state

Consequently, the outputs of the Markov Chain state estimation are calculated based on the use of the online computed initial distribution u_i and the offline calculated transition matrix P_i for the respective activated subsystem. As the complete vehicle observer is designed for a sample time of $T_s = 10(ms)$ the equation

$$v_i(k) = u_i(k) \cdot P_i^n \tag{4.32}$$

is updated in every execution step k. Here, v is a vector of the dimension $1 \times l_i$. In case of delayed signals this calculation is done for the first power of P_i. In case of missing signals the power increases with the time of signal absence. To reduce the computational effort the row searching is limited to the gradient thresholds. But as this vector v can not be used for the final state estimation, an additional computation is implemented.
For a higher accuracy of the state estimation during delayed or missing sensor signals all non-zero entries of the vector v are taken into account. Here, an interpolation is implemented and, by this, the defined limited state space is extended without any high computational complexity. This post-processing is composed of four different steps.
Firstly, all indices of entries in v_i that are non-zero are written into a new vector v_i^*.
Secondly, a factor g is calculated that compensates the decreasing probability values for a longer activation time of the Markov Chain state estimation. That factor guarantees that the sum of all probability values remains at 1 for all time steps k. This factor is

computed by the use of the following equation:

$$g(k) = \frac{1}{\sum_{j=1}^{d} v_i^*(j)},$$

(4.33)

where d is the last entry of vector v_i^*.

The sum f of the weighted probabilities for all non-zero entries, which results in the index of the state space, is computed in the third step according to:

$$f(k) = \sum_{j=1}^{d} g(k) \cdot v_i^*(j) \cdot v_i(j).$$

(4.34)

In contrast to the defined state space, the index f can also represent fraction numbers and, thereby, enable a higher precision of the result.

Finally, the Markov Chain state estimation is computed by:

$$\hat{u}_i = f(k) \cdot \Delta u_i$$

(4.35)

In the here introduced concept, by the use of Markov Chains, the time for replacement of missing signals is bounded to a maximum of $t_{max} = 3\ (s)$. As the safety concept accepts tolerance times of $50(ms)$ to detect false sensor performance the sample time is short enough to fulfil this requirement.

5 Results

After the developed functions Vehicle Observer and Markov Chains were described in detail in the chapters before, now the validation of these functions should be given. Firstly, the software was validated in general with simulation runs for the described driving manoeuvres, see 2.3.1. When the results met the defined accuracy, the software was converted and integrated into the VHU for the second validation step. During this work, these validation steps were repeated several times for an optimised performance in terms of execution efficiency and accuracy of the results.

In order to integrate the designed software into the VHU of the prototype it had to be converted into machine code. The machine code is required to run the software on the micro-controller with the highest efficiency. A drawback of the machine code is that it is not very intelligible which makes debugging work almost impossible.

Moreover, the data types of the functions had to be converted from floating point into fixed point as the micro-controller is optimised for operations with fixed point data. Here, the hardware was limited to 32-bit signals which resulted in a slight lowered accuracy compared to the floating point software during simulation runs.

Due to technical limitations and safety concerns with the prototype, the validation was split for the two software blocks. On the one hand the Vehicle Observer software was implemented into the target hardware on the prototype. On the other hand the complete observer including Markov Chains algorithm was tested by Hardware in the Loop (HiL) with measured sensor signals from the prototype as inputs.

In this chapter the validation of the Vehicle Observer with prototype runs is given in section 5.1. Here, different driving manoeuvres were carried out. In section 5.2 the performance of the Markov Chains method for signal replacement is shown during HiL tests.

5.1 Prototype results

During the eFuture project many vehicle tests were defined and performed with the prototype. Here, two scenarios for the developed software are discussed: Slalom driving and double lane change.

The tests took place at the airbase in Giebelstadt where a plain area of about 315×70 meters was available. The road surface is concrete for the complete area. The handling tests covered circular driving, double lane change, slalom driving, straight acceleration and braking at different speeds. The tests were done with and without the function Torque Vectoring to proof the enhanced stability control with this function. The figures for all presented scenarios were measured with enabled Torque Vectoring. In this case, the additional generated yaw moment changes the expected model behaviour in the EKF

subsystem so that a deviation would occur if the designed observer was not adaptive and robust enough.

The measurement signals were recorded from three CAN buses with the software CA-NOE. For the reference measurements a Correvit optical sensor [59] was fixed on the rear right door (see Fig. 5.1). This sensor measures the longitudinal velocity, the lateral velocity and the side slip angle of the vehicle. Since the Correvit sensor was not fixed in the CoG of the vehicle an additional calculation has to be done in order to clear position influences on the measurements. In detail, the yaw rate multiplied by the lateral distance of the sensor to the CoG has to be added to the lateral velocity. The lateral distance was measured by hand during standstill: $l_{Corr} = 0.6m$. It turned out, that the impact on the measurement of the side slip angle could be neglected.

Figure 5.1: Prototype equipped with Correvit sensor

As the figures of the different vehicle states are not specific enough for the analysis of the vehicle observer accuracy, the computation of the Root Mean Square Error (RMSE) is inserted. In general, the RMSE of a data series is just one value. This method was extended by a sliding window so that the accuracy can be analysed at different moments during the process. Here, the length of the sliding horizon was set to $t_{slide} = 2 \ s$. With a sample time $T_s = 0.01 \ s$, the latest 200 values are taken into account to compute the current $RMSE_i$. The equation is given by:

$$RMSE_i = \sqrt{\frac{T_s}{t_{slide}} \sum_{k=k_i}^{k=k_i+\Delta T} (x(k) - \hat{x}(k))^2} \tag{5.1}$$

Where T_s is the before mentioned sample time, k_i is the starting index of the simulation time, x is the reference value and $\hat{x}$ is the observed value. This calculation could be carried out for the three states that are measured by the Correvit optical sensor. Here, the most important results for circular driving, double lane change and road friction estimation are presented.

5.1.1 Slalom driving
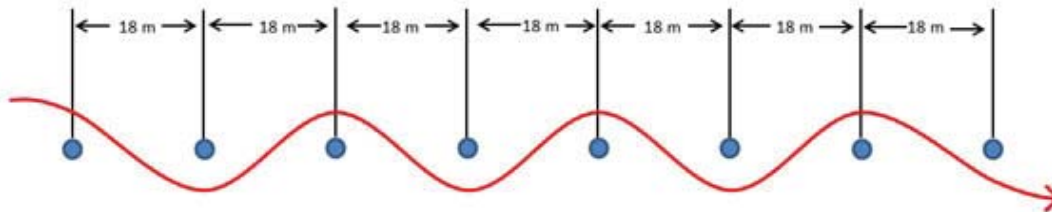
Figure 5.2: Slalom driving set up

Test description

For the slalom driving tests, eight cones were arranged with a distance of 18 m (see Fig. 5.2). After a straight line acceleration to the desired speed, the driver tried to hold the vehicle speed during the movement through the cones. As it was a non-professional driver, this goal could not be achieved for all speeds since it is very hard to hold the velocity at high dynamic cornering. The tests were carried out with increasing speed until the handling limit of the vehicle was reached. The process of the steering angle is displayed in Fig. 5.3.

Signal comparison

In Fig. 5.4 to Figure 5.6 the longitudinal and lateral acceleration and the yaw rate of the sensor and the vehicle observer are displayed for a slalom drive at 50 kph. During standstill and during low speed, from measurement beginning until 6 s, the signals are identical because the vehicle observer algorithm is not activated and the sensor signals are bypassed. When the algorithm is executed, the smoothing and correction of the sensor signals become obvious. The noise level of the longitudinal and lateral acceleration could be lowered significantly and signal peaks could be erased but the general progression of the signals remains, whereas the noise level of the yaw rate sensor signal seems very low for this driving manoeuvre and, thereby, the sensor and observer outputs are mainly the same. The high yaw rate at the end of the measurement gives an indication that the vehicle got unstable for this speed and the test was not successful. These results
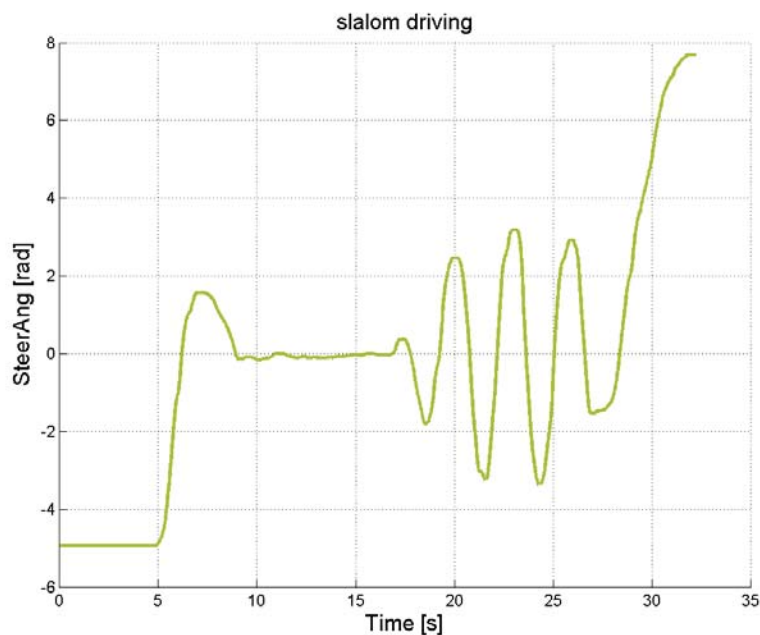
Figure 5.3: Steering angle during slalom driving

were selected to show that the observer is capable to observe the vehicle states even in uncontrolled vehicle movements.

In Figure 5.7 to Figure 5.9 the longitudinal and lateral speed and the side slip angle of the reference sensor and the vehicle observer are shown. Moreover, the corresponding longitudinal speed computed with the front wheel speeds are plotted in Figure 5.7. Where the longitudinal velocities match for the reference and observer outputs, except for the end of the measurement where the vehicle got unstable, the lateral velocity and the side slip angle have a different amplitude and a delay between the sensor and observer output of about 100 ms could be detected. The deviation of the amplitudes is caused by the correction of the observer algorithm or the not well calibrated reference sensor. The delay between both signals is a time stamp problem of the measurements. Here, the synchronisation of reference sensor and vehicle CAN did not work correctly.

Signal analysis

The progression of the RMSE for the three vehicle states that have reference data are shown in Figure 5.10 to Figure 5.12. The limits for the RMSE, that were defined at the beginning of the project, are not exceeded for most of the time but, as outlined above, the vehicle instability caused an overshoot of the longitudinal velocity RMSE at the end of the measurements. Considering the unstable vehicle state and since this overshoot is close to the limit, this deviation is not critical. Thereby, the vehicle observer performs
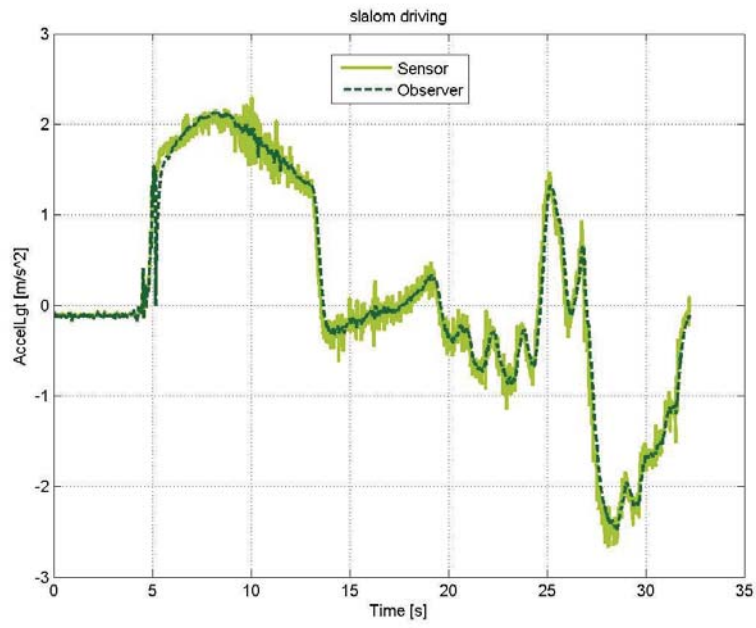
Figure 5.4: Longitudinal acceleration
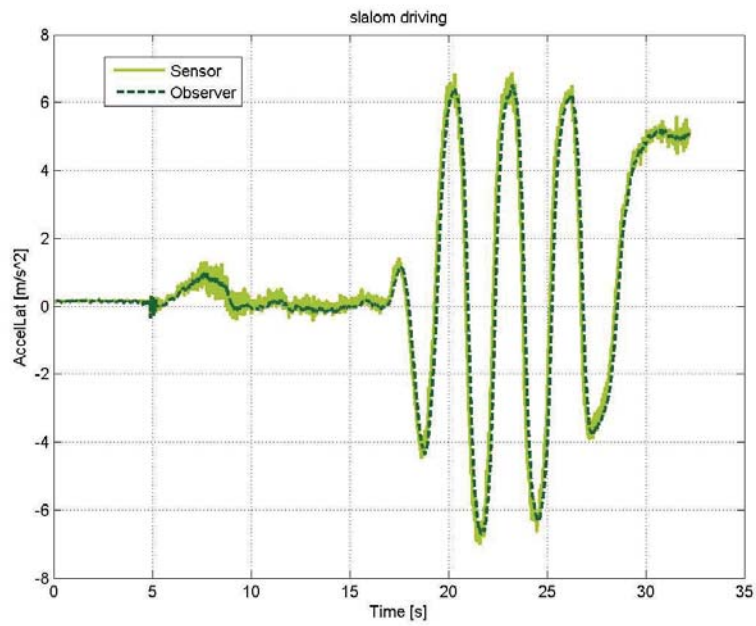
Figure 5.5: Lateral acceleration
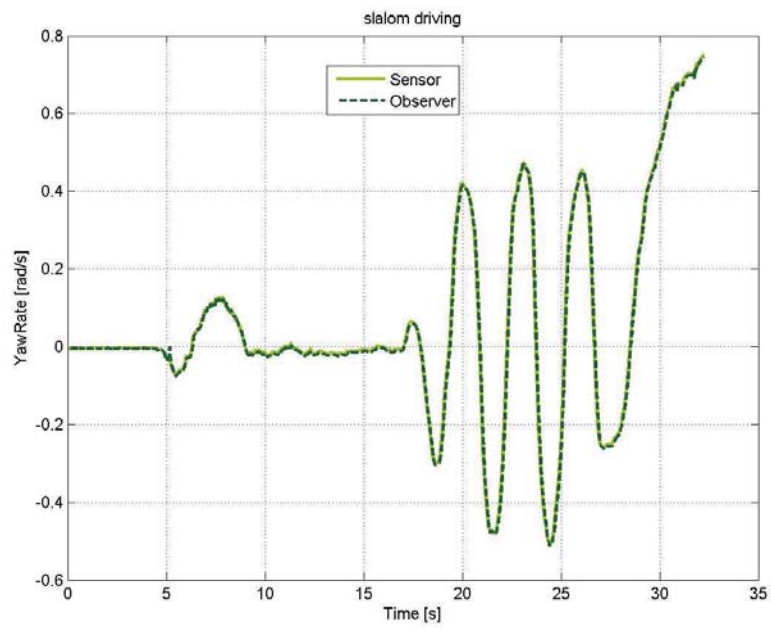
Figure 5.6: Yaw rate
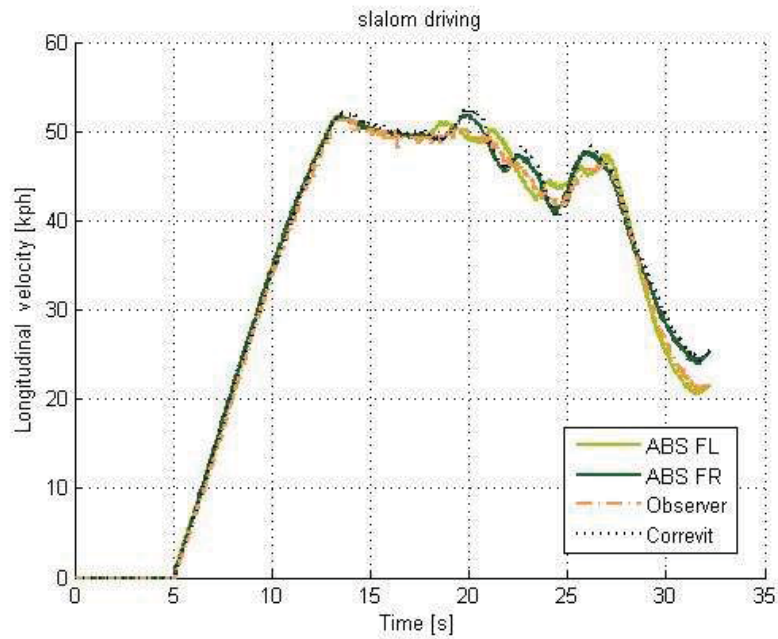
Figure 5.7: Longitudinal velocity
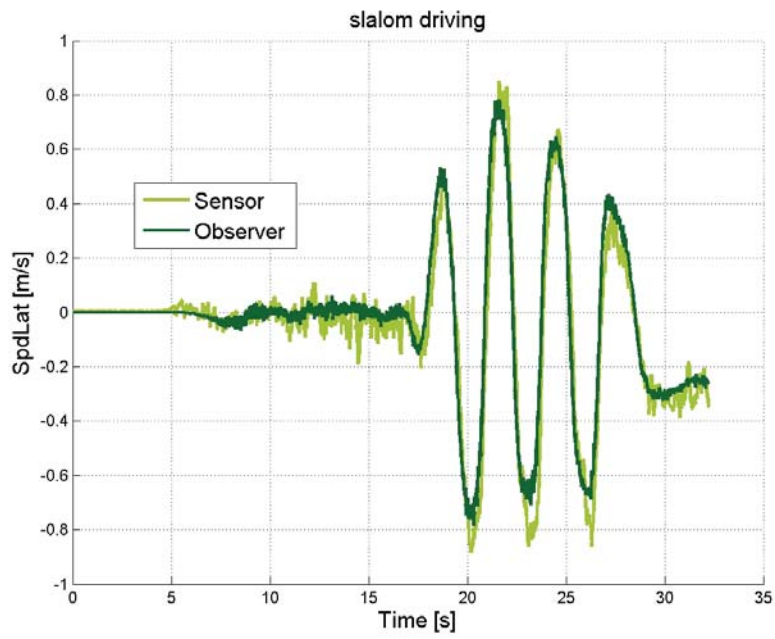
Figure 5.8: Lateral velocity
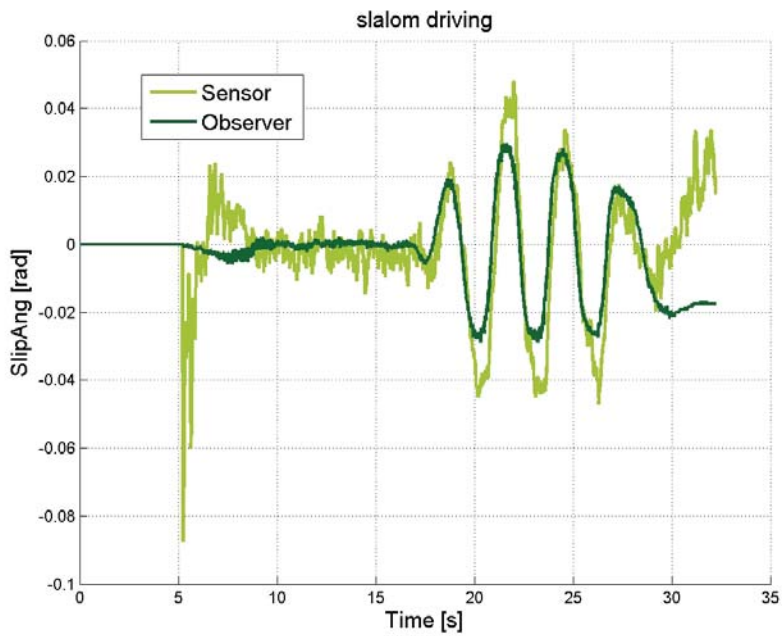
Figure 5.9: Side slip angle
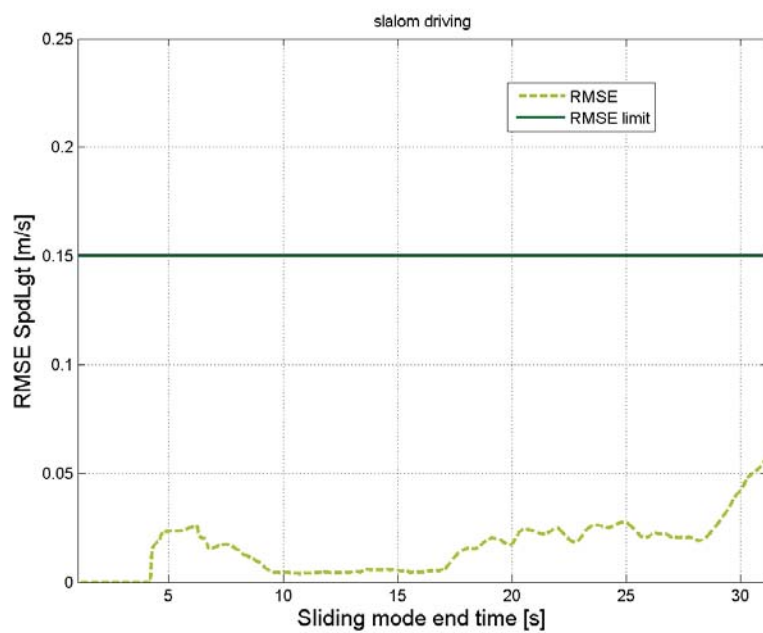
Figure 5.10: RMSE of the longitudinal velocity
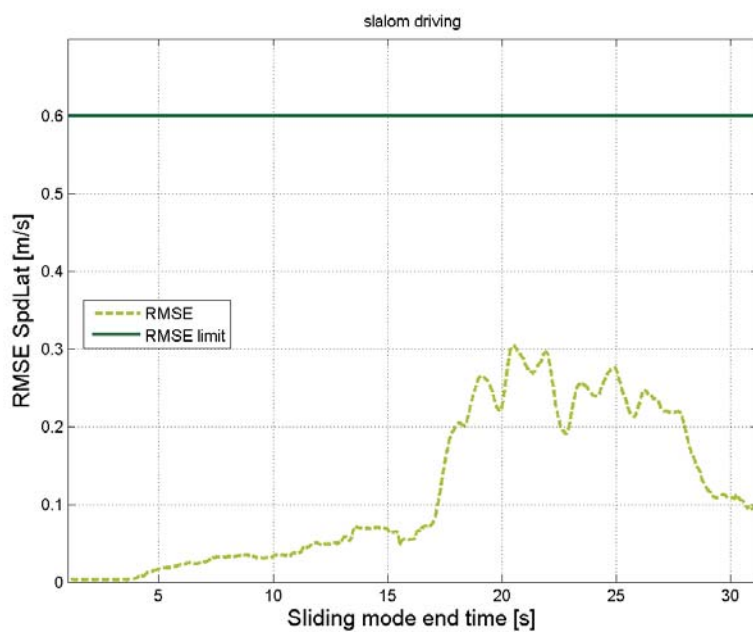
Figure 5.11: RMSE of the lateral velocity
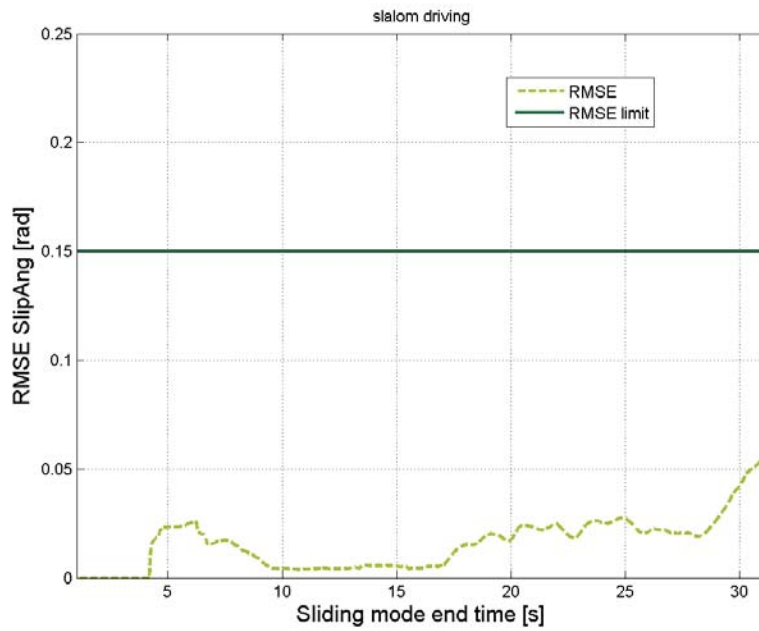
Figure 5.12: RMSE of the side slip angle

with the aimed accuracy during the slalom driving scenario.

5.1.2 Double lane change
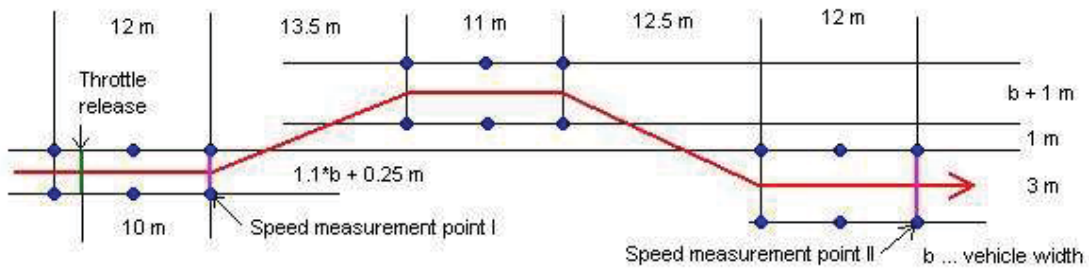
Figure 5.13: Double lane change set up

Test description

The DLC (also known as elk-test) manoeuvre is appropriate to test lateral dynamics with fast changing steering inputs. It gives a good indication of the stability and control of a vehicle. It is carried out by driving through a tight lane of cones, swerving hard into another lane of cones, before swerving hard back into the original lane. It is also

designed to simulate the sudden DLC that can cause vehicle instability. The test was set up according to the standardized ISO 3888-2 norm [6] for a manually measured vehicle width of $b = 1.4\ m$ (see Figure 5.13). In order to remove longitudinal influences, the driver shifted to neutral gear before the steering test began. At the end of the test, the driver used the hydraulic brake to stop the vehicle. Starting with an initial speed of 30 kph, the speed was increased in steps of 5 kph until the vehicle trajectory could not hold the defined path any more. As the test was done by a non-professional driver, the results have an optimisation potential. Subsequently, the results for a DLC with an initial speed of 50 kph are shown. The process of the steering angle is displayed in Fig. 5.14.
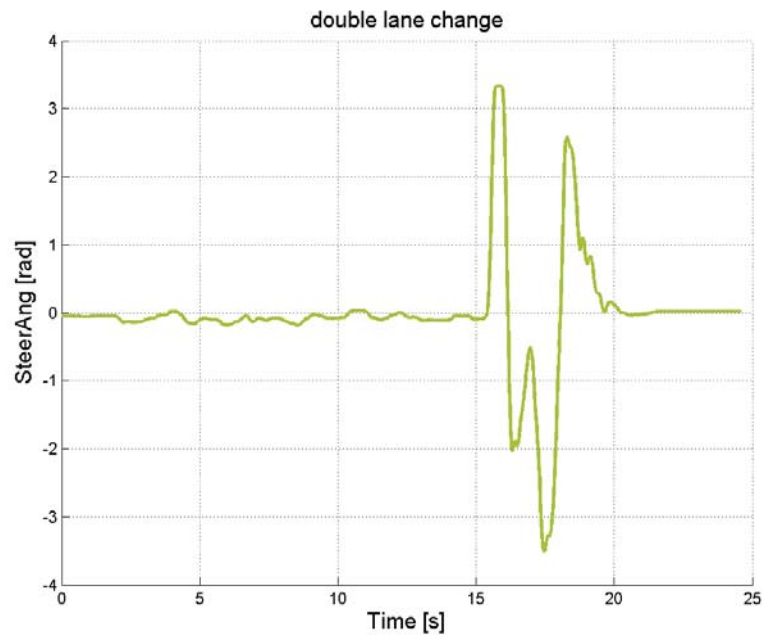
Figure 5.14: Steering angle during double lane change

Signal comparison

In Figure 5.15 to Figure 5.17 the longitudinal and lateral acceleration and the yaw rate of the sensor and the vehicle observer are presented. When the observer algorithm is executed from simulation time 2 s on the lowering of the noise level, the correction of amplitudes and cancellation of signal peaks is obvious. In comparison to the yaw rate results from the slalom driving, which were equal for most of the time, here, a correction of the measured yaw rate can be identified. The yaw rate before and after the DLC manoeuvre has static characteristics which is reasonable for the straight acceleration and braking. Thus, the performance of the observer for these three signals is satisfying.
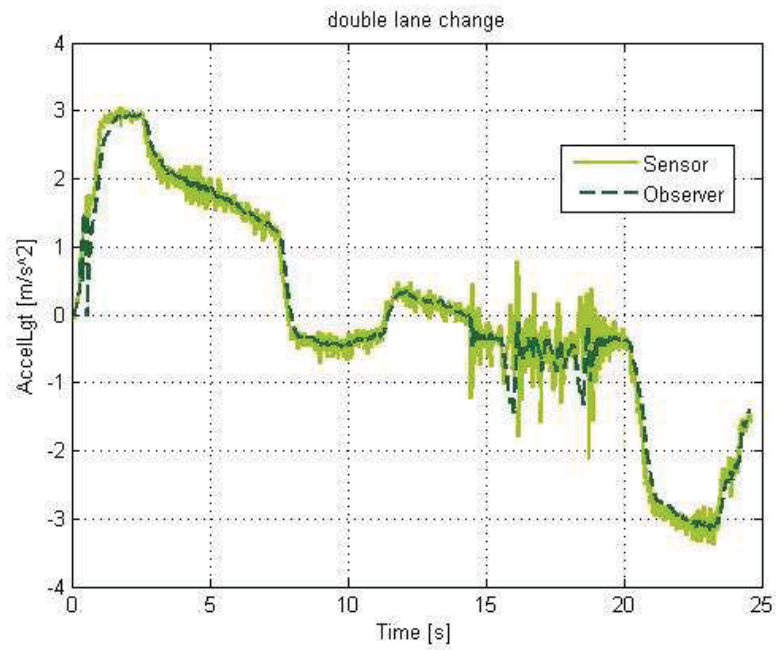
Figure 5.15: Longitudinal acceleration
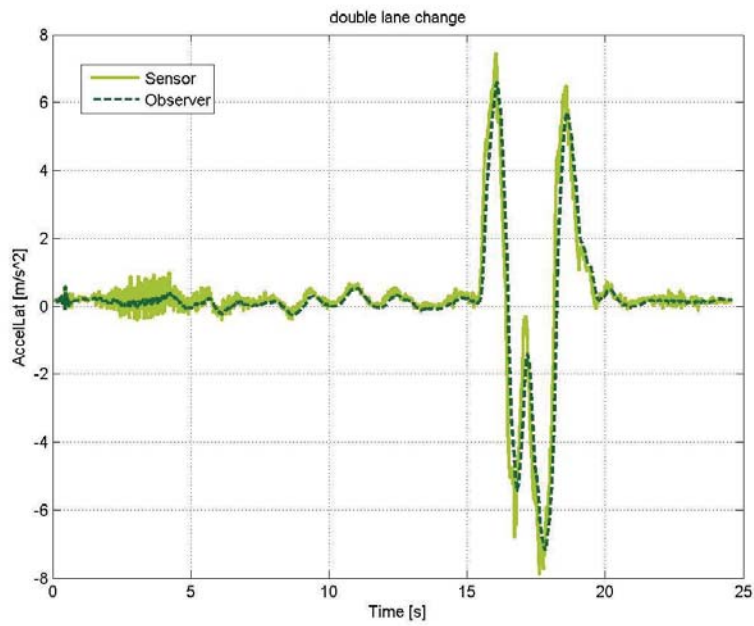
Figure 5.16: Lateral acceleration
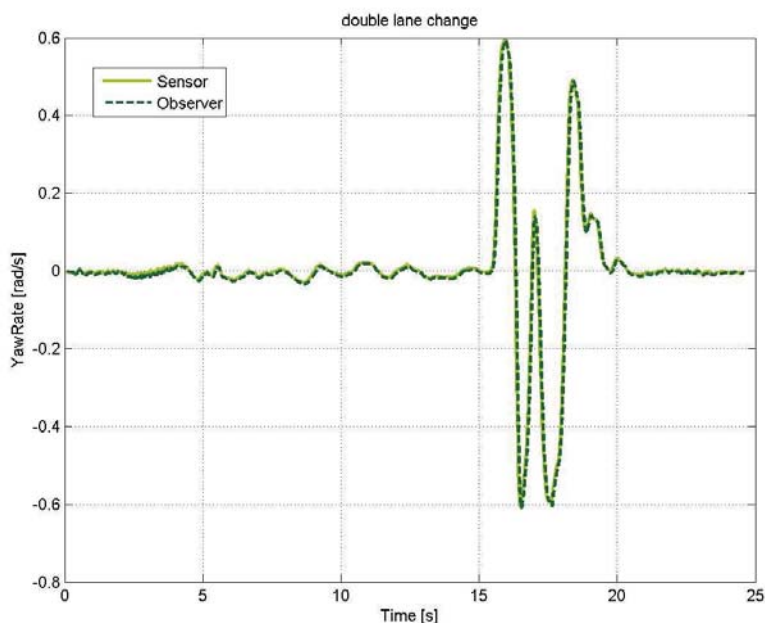
Figure 5.17: Yaw rate

In Fig. 5.18 to Fig. 5.20 the longitudinal and lateral speed and the side slip angle of the reference sensor and the vehicle observer are shown. Where the longitudinal velocities match exactly with the acceleration and braking period of reference and observer outputs, there is a slight deviation during the steering manoeuvre. The oscillating speed of the Correvit sensor from $15.5\,s$ to $19\,s$ is based on the outer right position of the sensor. In detail, the sensor detects a higher velocity when the vehicle steers to the left side and vice versa. At the beginning, the observer signal noise level of the lateral velocity and the side slip angle is greater than that of the reference sensor. This is based on the calibration period of the observer algorithm where the covariance between model and sensor state is tuned. When this process is completed ($\sim 6s$) the noise level of the observer outputs are lower than those of the reference sensor. The deviation of the amplitudes results from roll movement of the vehicle and the outside position of the reference sensor. Moreover, the correction of the algorithm influences the amplitudes as well.

Signal analysis

The progression of the RMSE for the three vehicle states that have reference data are shown in Figure 5.21 to Figure 5.23. The limits for the RMSE that were defined are not passed. By that, the vehicle observer performs with the aimed accuracy during the double lane change scenario. In all three figures the RMSE value is rising during
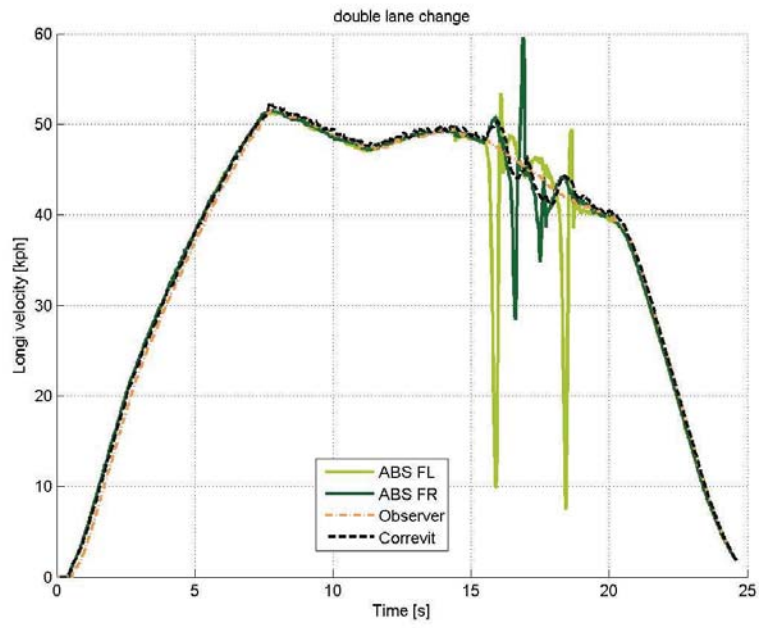
Figure 5.18: Longitudinal velocity
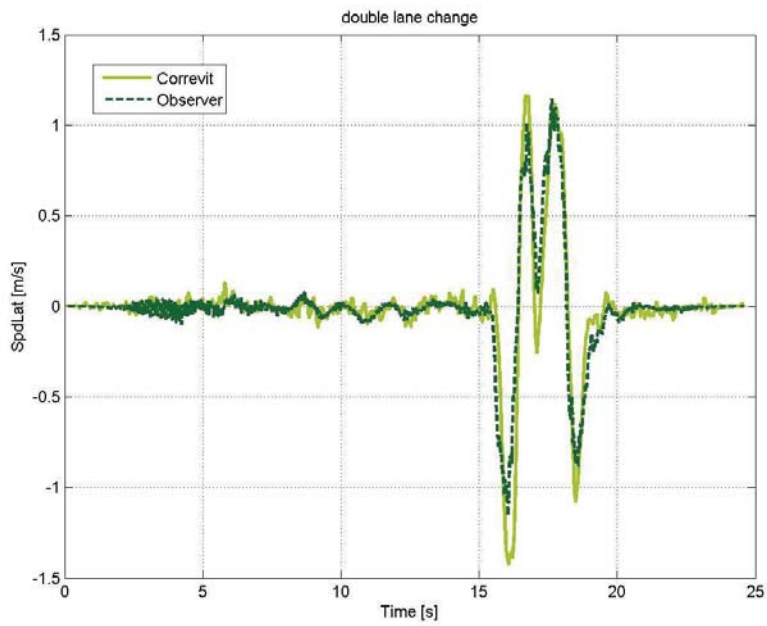
Figure 5.19: Lateral velocity
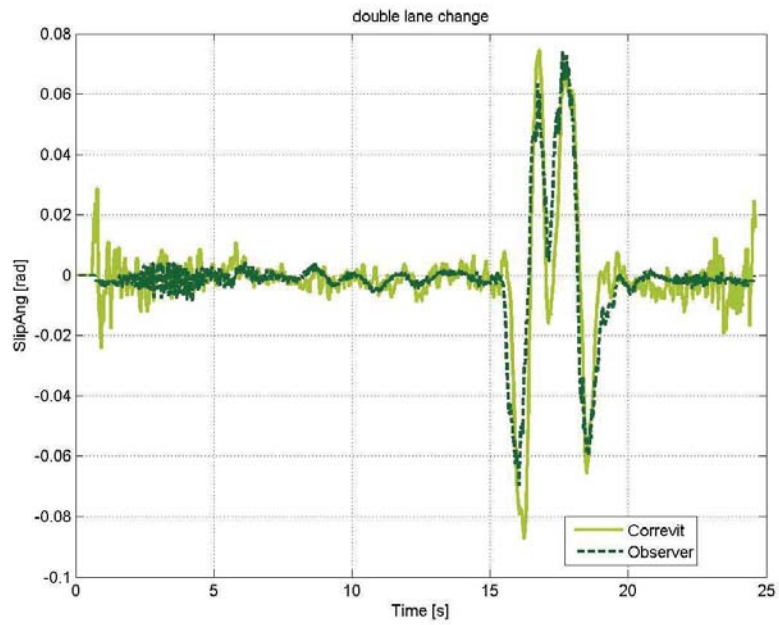
Figure 5.20: Side slip angle
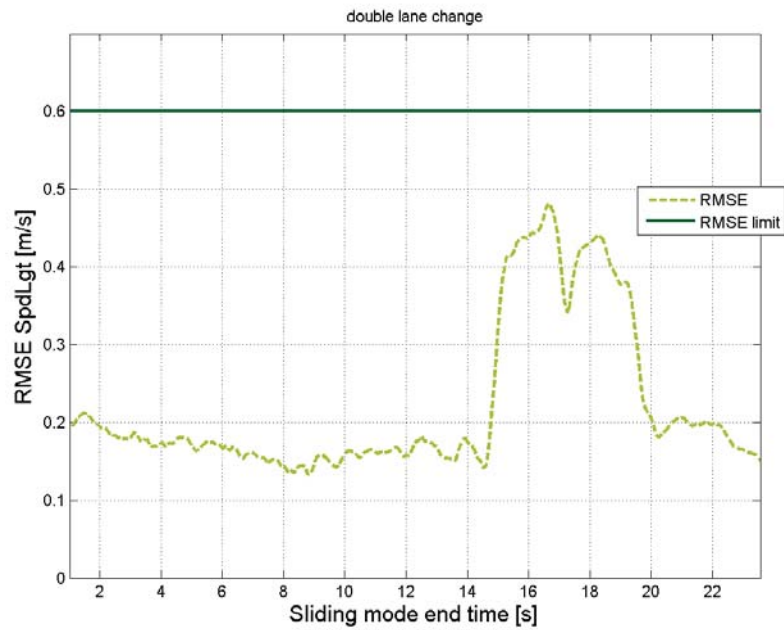
Figure 5.21: RMSE of the longitudinal velocity
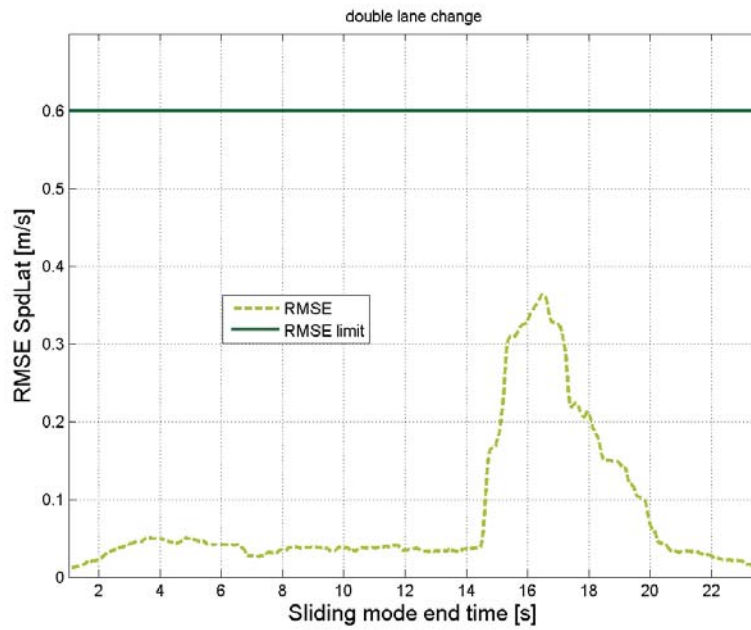
Figure 5.22: RMSE of the lateral velocity
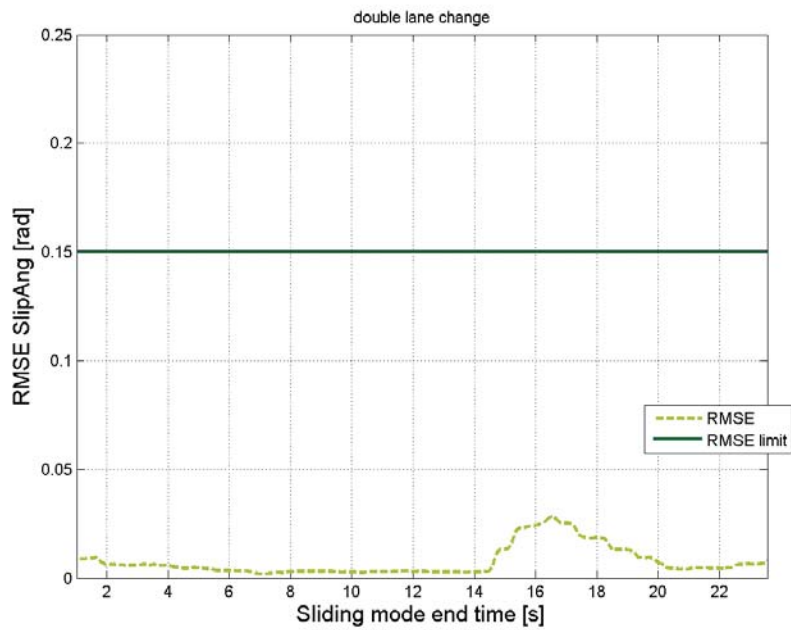
Figure 5.23: RMSE of the side slip angle

steering but, as written before, the dynamic influences on the reference sensor could not be eliminated.

5.1.3 Road friction estimation

The road friction estimation has great impact on the vehicle dynamics since it limits the maximum motor torque with respect to the stability limits of the vehicle. Because the road friction is hard to measure some tests on dry surface and slightly wet surface were carried out to validate the estimation. Unfortunately, there were no real wet weather conditions during the testing phase but the results indicate the correctness of the road friction estimation.

As the presented concept bases on the longitudinal tyre slip λ, the estimated value for both test conditions are shown in Fig. 5.24. Whereas the longitudinal slip is estimated as very high, when the vehicle observer algorithm is activated at $5s$, the values decrease rapidly when the observer estimates the real vehicle velocity. After this initializing phase, in which the slip for both conditions is almost the same, the slip for the wet conditions is higher than the slip for the dry conditions.
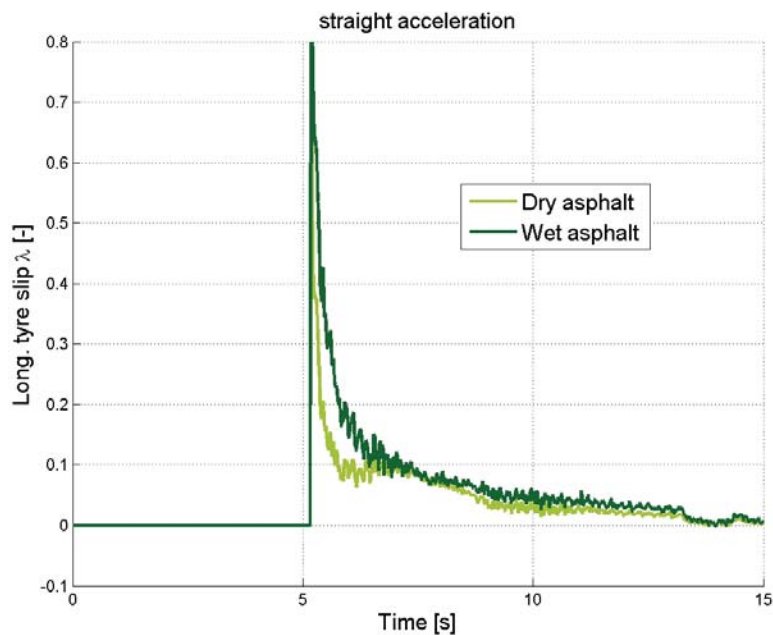
Figure 5.24: Longitudinal tyre slip estimation

In Figure 5.25 a comparison of the estimated maximum road friction coefficient μ_{max} for DLC on dry and light wet road surface in a straight line acceleration scenario is given. Here, both measurements were synchronized, that it is possible to plot them in one single figure.
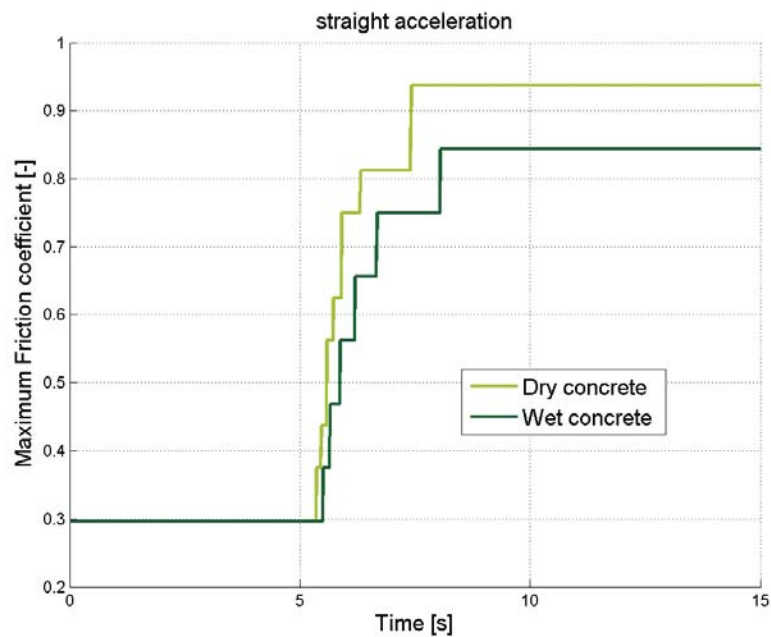
Figure 5.25: Friction estimation for different road conditions

As the method of estimating the road friction with recursive least squares is based on the wheel slip, the value increases quickly for both methods when the vehicle is accelerated from standstill at time $5s$. After a calibration period of about $0.5\ s$, where the estimated values are increasing very quick, the friction coefficient for the dry condition is at 0.75 and the one for wet conditions is at 0.65. Then the estimation concept is improving these values which takes more time, about $3s$, than the rough estimation in the first phase. The final estimated maximum friction coefficient μ_{max} of the light wet concrete is 0.85 and the one for dry concrete is at 0.94. This is conform with the information that can be found in literature [67] and 3.10.
In order to validate this estimation further, some tests on snow or icy road would be needed.

5.2 Hardware in the loop results

As stated before, the Markov Chain algorithm for the sensor signal replacement was validated by HiL tests. Technical limitations on the one hand and safety concerns on the other are the reason that the software was not tested for the prototype.
For the implementation of the software into the prototype, from a technical point of view, there was a lack of hardware to feed defective sensor signals on the CAN to all components. It would have been possible to influence the input to the vehicle observer
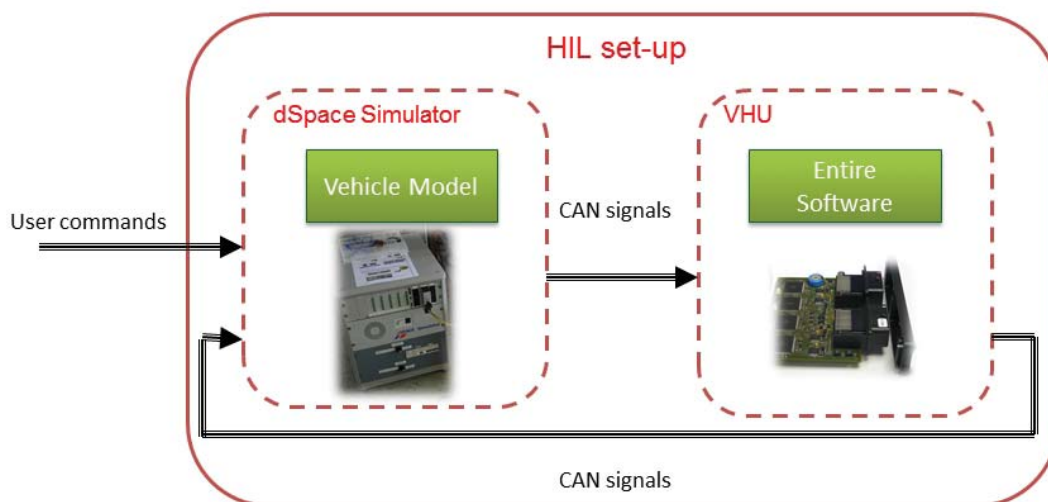
Figure 5.26: HiL set-up for validation

but as the sensor signal is transmitted to other software blocks as well this may cause an undefined vehicle control. In the worst case, that could have lead to a hardware defect or an unstable vehicle.

The safety concerns arose from these technical limitations. In order to prevent mechanical damage of the prototype, the limited test area and due to budget constraints, the project management decided not to integrate the software into the vehicle. Moreover, this concept of signal replacement for delayed or missing sensor signals was not part of the project. Nevertheless, the Markov Chains were implemented on the VHU and tested by a HiL process. The set-up and configuration will be given in the next section.

5.2.1 HiL set-up

The validation of the Markov Chain algorithm took place in the test-bench laboratory at Intedis. Here, the required hardware was provided and necessary engineering safeguards are installed to realise HiL tests. Before the validation on the target hardware, the software had to be converted to use Fixed-Point data types and a machine code had to be build again.

To validate the signal replacement by HiL, the signal routing of recorded sensor signals with a random deactivation of the specific signal to the extended vehicle observer was built in a model. By the use of the dSpace Real-Time Interface (RTI) library that enables the CAN communication between the VHU and the applied hardware, which will be described later on, a code is generated for the use in the software ControlDesk® (see Fig. 5.26). ControlDesk® itself is an universal experiment software for Electronic Control Unit (ECU) development which was designed, among others, for HiL validation and testing [19]. Here, the signal routing takes place and important signals can be

monitored easily during validation by an user friendly Graphical User Interface (GUI). The real-time system consists of a DS 1006 processor board, a E/S DS 2211 and DS814 card to connect the real-time system to the host PC (see Fig. 5.27 left). On the front, there are three ECU connectors, an adapter for On-board diagnostics (OBD) connector and jacks for the battery voltage and ground. An optical cable is used for the connection itself.
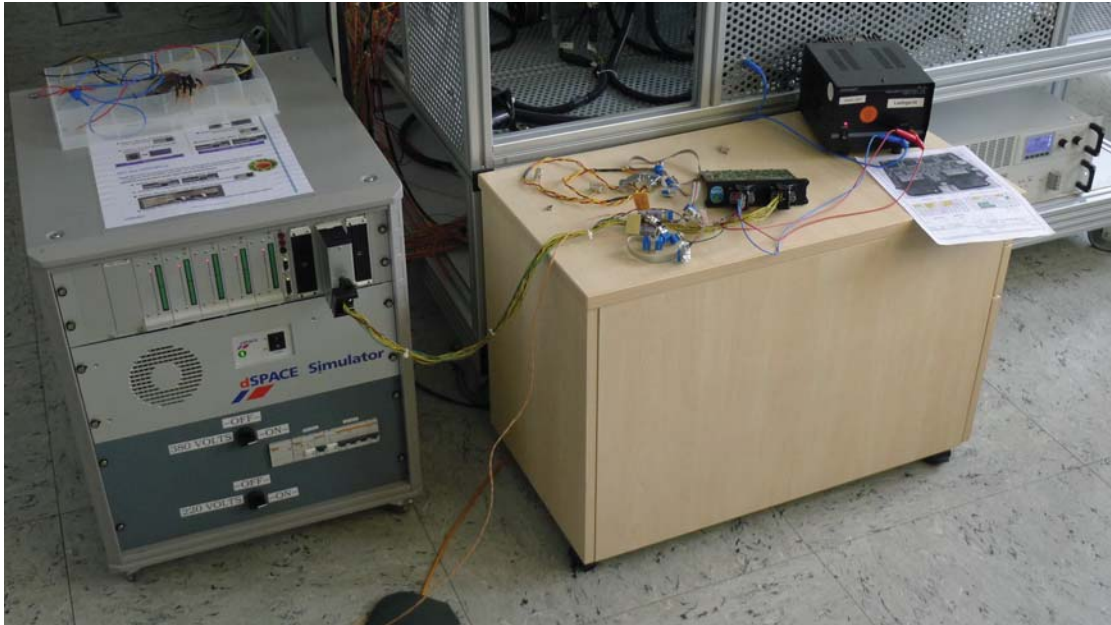
Figure 5.27: HiL for validation

The VHU is connected to an external 12V power supply and the CAN port of the hardware (see Fig. 5.26 right). As the hardware is limited to drive two CAN channels only, but the VHU has four channels, some modifications in the software were needed in order to guarantee the validation was working. By this, vehicle and motor CAN were sufficient to perform the tests. Additional connectors in the wiring between the real-time system and the VHU enabled the access to one specific CAN signal for monitoring.

5.2.2 Validation process

In this section the process of the HiL tests are introduced. As mentioned before, these tests were performed with recorded sensor signals from the prototype during test runs as inputs to the VHU. Here, random sensor failures were implemented where only one sensor at once is affected and the absence time varies between 0.5 and 3 seconds for every sensor malfunction. During this sensor malfunction, the recorded sensor signal is replaced by a signal that is constant zero.

The results are presented for the pure signal replacement by using the Markov Chain algorithm and for the complete observer performance. Ongoing, the results are shown for

three different malfunction scenarios and were tested with sensor signals whose absence is seen as critical for the ADAS vehicle control. In detail, the defective performance of the steering angle sensor, one wheel speed sensor and the yaw rate sensor is given.

To proof the enhanced accuracy of the signal replacement with the Markov Chain concept, the RMSE is computed again. In contrast to the observer states, where a sliding window was used, in HiL tests the values for the RMSE during signal loss are calculated sequentially by:

$$RMSE(k) = \sqrt{|x(k) - \hat{x}(k)|^2} \tag{5.2}$$

The presented scenario was a normal anti-clockwise driving on the test area where the speed varied between 9 and $16m/s$.

5.2.3 Steering angle sensor malfunction
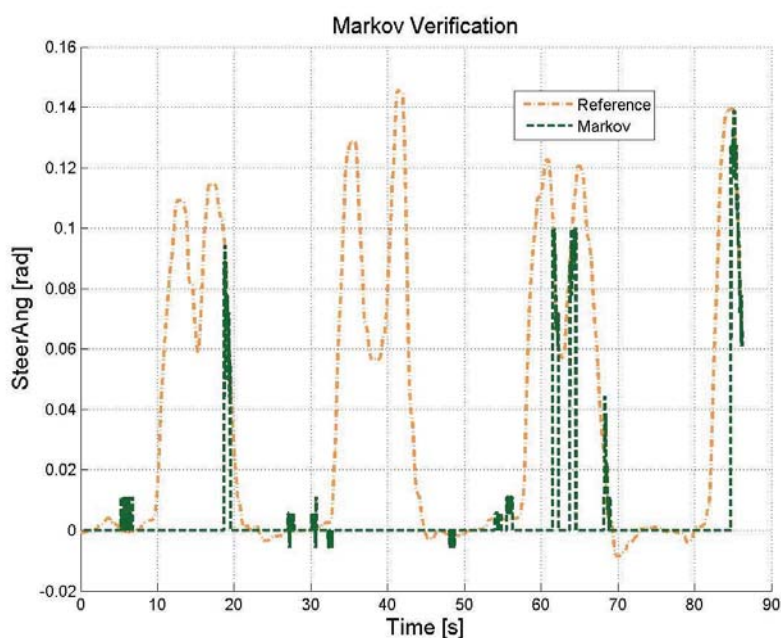
Figure 5.28: Signal replacement of missing steering angle sensor

The first presented scenario of sensor malfunction is the steering angle. This signal is one of the most important signals for the lateral dynamics of the vehicle. Here, a high accuracy is needed for a correct ADAS performance. For instance, the desired vehicle states for the TorVec function are computed by the use of the steering angle.

In Fig. 5.28 the reference sensor signal is plotted with a solid line and the estimated signal by the Markov Chain concept is plotted by a dashed line. During the time the sensor signal is detected as correct, the Markov Chains algorithm is deactivated and the signal is thus set to zero. Whenever the signal is missing, the concept is able to
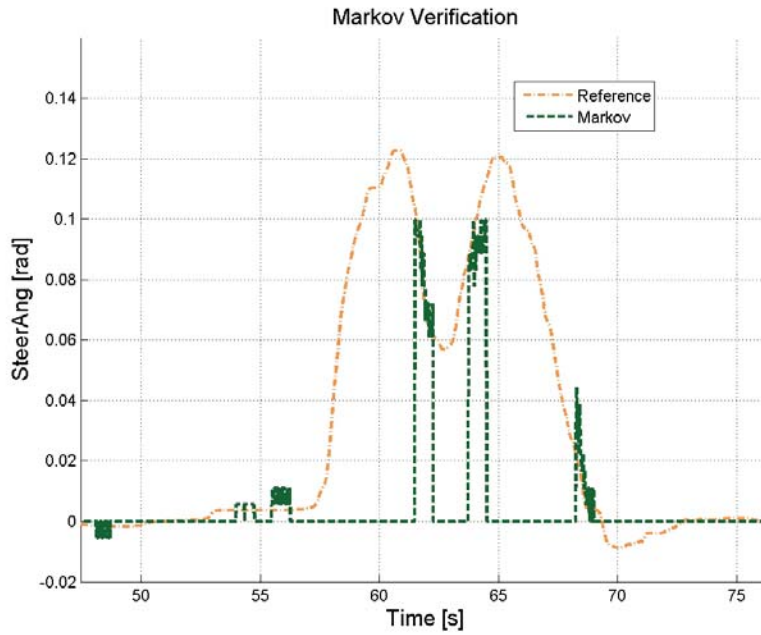
Figure 5.29: Zoomed view of signal replacement for missing steering angle sensor

replace the steering angle. Minor changes can be seen if the steering angle is around zero. Here, small oscillations are the result of the online calculated initial distribution but the amplitude of that deviation is very low. Moreover, it can be seen, that the output values are more precise than the discrete state space that was defined in Tab. 4.3. As the exact performance of the signal replacement is non-optimal displayed over the complete measurement time in Fig. 5.29 a zoomed view is given, where more details are displayed. It can be seen, that the reference values are not met exactly at each step but the deviation is very low.

In Fig. 5.30 the process of the RMSE for the Markov concept is plotted by a solid line and the missing sensor signal is plotted by a dashed line. Only when the reference steering angle was around zero, the Markov concept showed a worse performance since the sensor signal was set to zero during this time. Whenever the sensor signal was missing during cornering, the RMSE of the Markov concept shows a much lower value than the one measured by the sensor .
As the validation was proven for the signal replacement of the steering angle, now, the improved performance of the complete vehicle observer shall be shown as well. Since the steering angle is not an observed state of the observer, the yaw rate was selected to analyse the overall observer performance.
In Fig. 5.31 the observed yaw rate with Markov input is plotted solid, the one with sensor input is plotted dashed and the reference sensor signal is plotted dashed-dotted. Only during cornering between $62 - 65\,s$ and $84 - 87\,s$ a difference between the signals
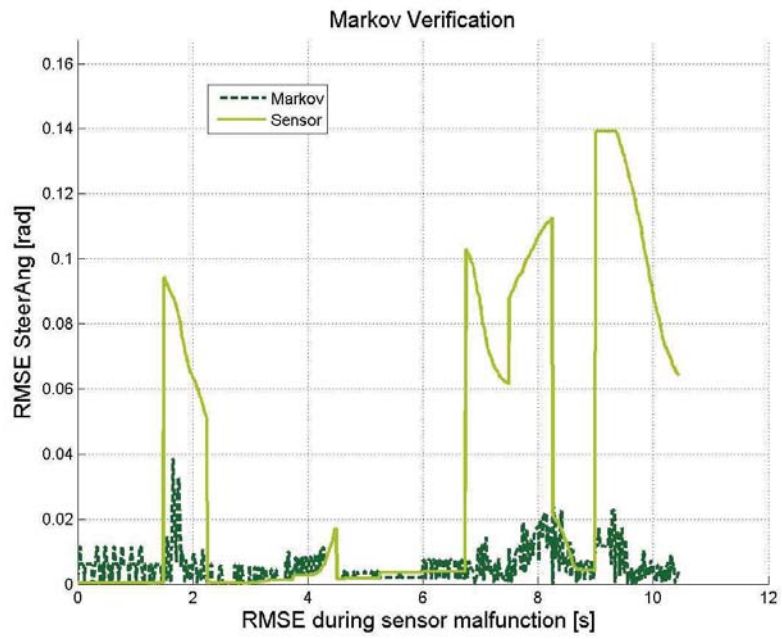
Figure 5.30: RMSE of sensor and signal replacement
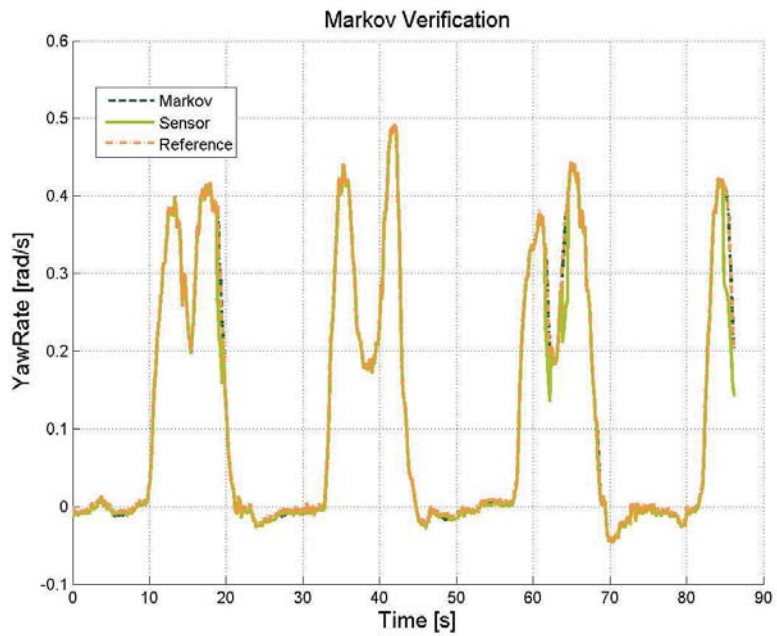
Figure 5.31: Observed yaw rate for sensor and Markov input

can be detected. This means that the vehicle observer algorithm is capable of estimating the yaw rate quite accurately even without knowing the steering angle. As well changes with high frequency of the steering angle have almost no influence on the yaw rate, since the vehicle does not react on these rapidly. In consequence, the sensor signals of four different wheel speeds and the yaw rate itself provide enough information for an accurate vehicle observer performance.
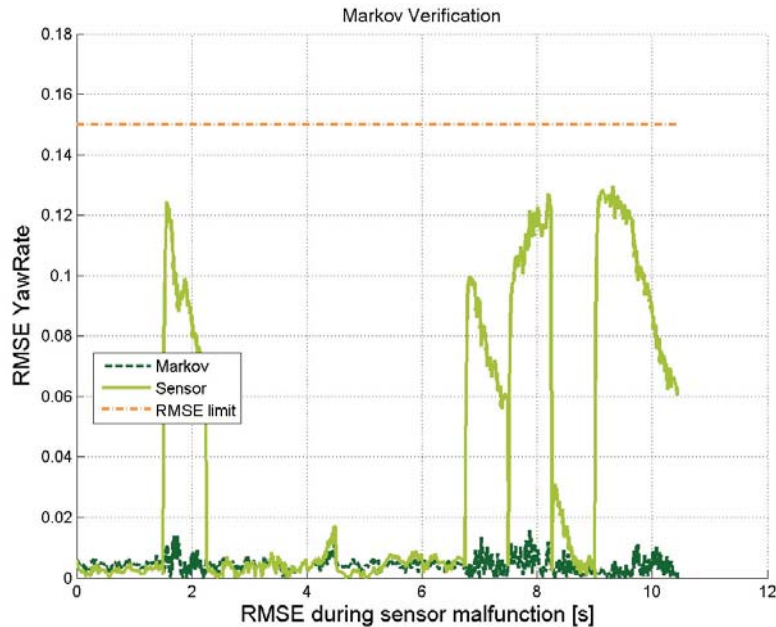
Figure 5.32: Observer RMSE with sensor and Markov input

The analysis of the RMSE for sensor and Markov performance is shown in Fig. 5.32. Except for the beginning, where the yaw rate is close to zero, the value of the RMSE with Markov concept for the yaw rate estimation is always lower than the one with sensor input. Overall, it has to be pointed out that the limit for the yaw rate estimation neither by the sensor nor by the Markov concept is exceeded. The improved robustness is validated in the first malfunction scenario.

5.2.4 Wheel speed sensor malfunction

The second scenario that was tested by HiL was the malfunction of one wheel speed sensor. It is of great importance for the complete functional architecture since it has a big influence on the vehicle speed which is used in many vehicle functions and, of course, in the vehicle observer to estimate the tyre slip and tyre forces. The implemented ADAS especially take the speed into account for activation decision and for the correct computation of the actuator requests in the control algorithms. For instance, a velocity

based gain scheduling control needs the exact vehicle velocity to compute the appropriate controller output.
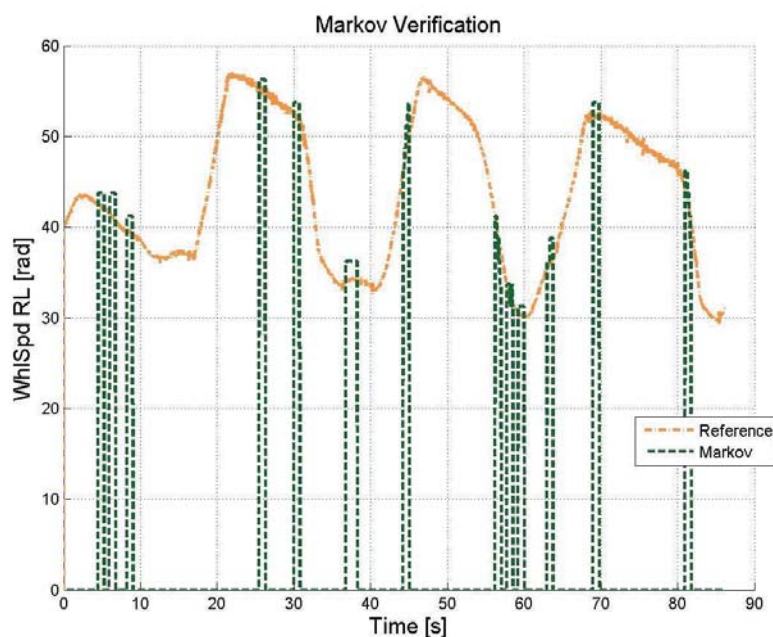
Figure 5.33: Signal replacement of missing wheel speed information

Although the wheel speed sensor in general can be seen as the one with the highest redundancy, since the vehicle is equipped with four for each wheel, the observer algorithm needs all four inputs to compute an accurate velocity. Here, the wheel speed sensor of the left rear wheel was simulated as being defective, due to the fact that the front angular velocities could be easily replaced by the respective electric machine angular velocity. Moreover, the angular velocities of the non-driven axle are preferred for the computation of the vehicle speed in serial cars because longitudinal positive tyre slip can be excluded. In Fig. 5.33 the reference signal of the rear left wheel speed is plotted by a solid line and the estimated Markov signal is plotted by a dashed line. Here, the random failure occurrence was activated very often. As soon as the signal is detected as missing, the Markov algorithm is able to estimate the current wheel angular velocity with satisfying accuracy. Minor deviations, especially from 37 to $39\,s$ of simulation time, appear.
As the exact performance of the signal replacement is non-optimal displayed over the complete measurement time in Fig. 5.34 a zoomed view is given, where more details are displayed. It can be seen, that the reference values are not met exactly at each step but the deviation is very low.

To analyse the performance, the comparison of the RMSE was carried out in Fig. 5.35. Here, the value of the Markov concept is up to 10 times smaller than the sensor
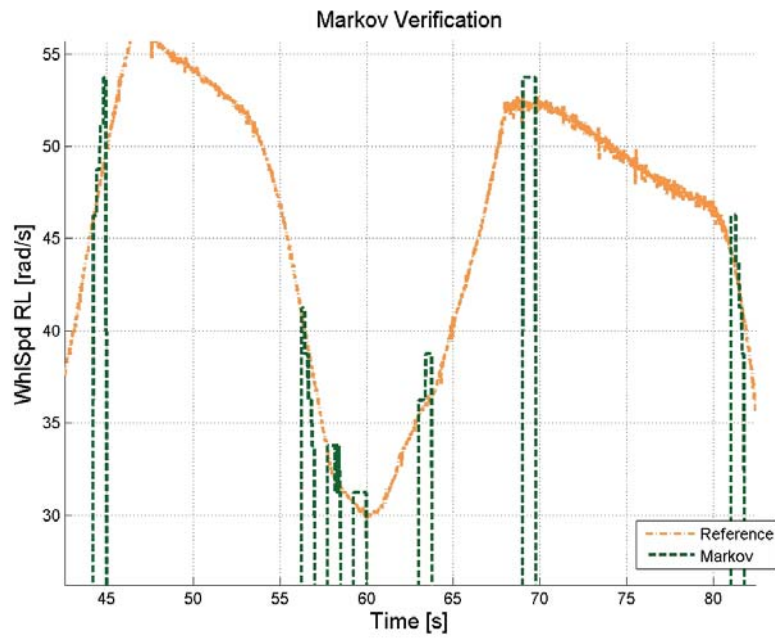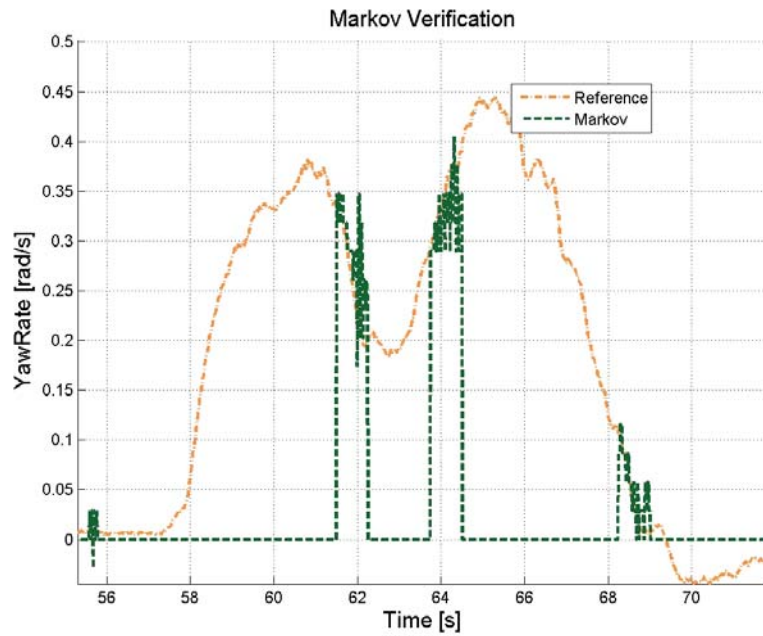
Figure 5.34: Zoomed view of signal replacement for missing wheel speed information
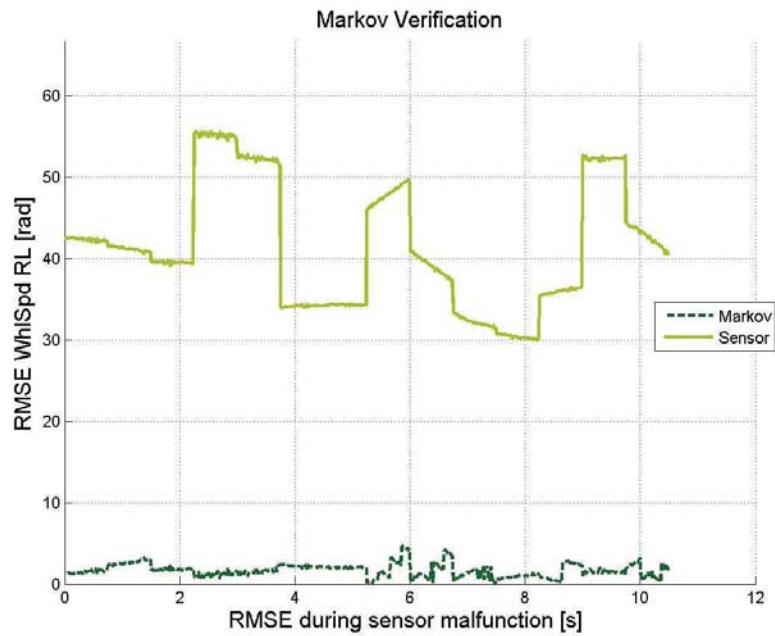

Figure 5.35: RMSE of sensor and signal replacement
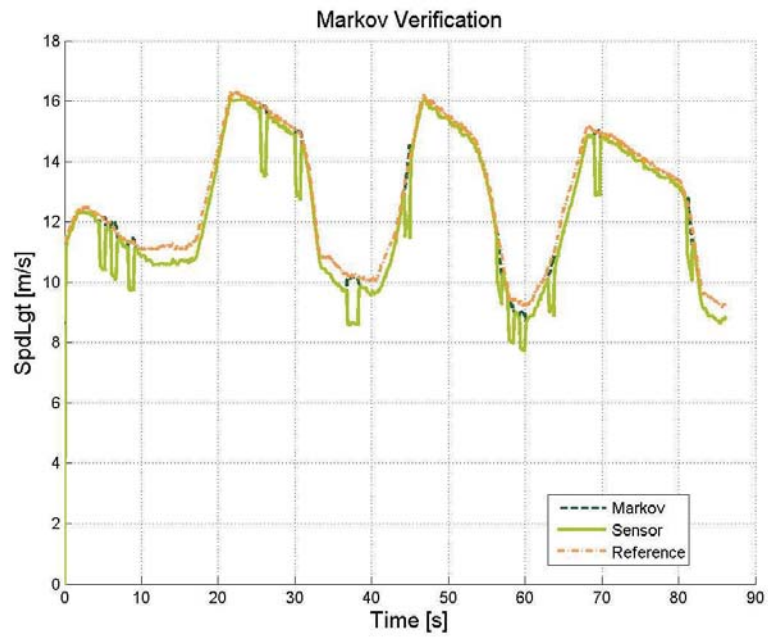
Figure 5.36: Observed longitudinal speed for sensor and Markov input
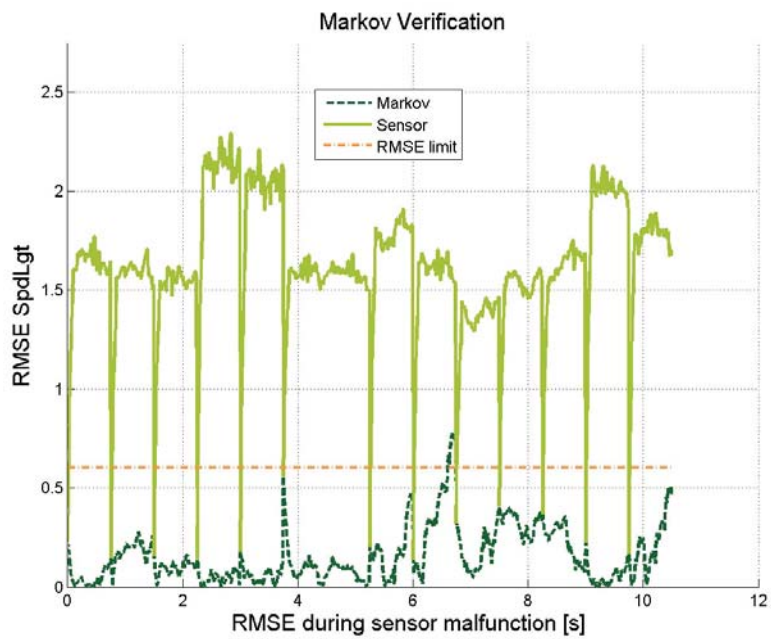
Figure 5.37: Observer RMSE with sensor and Markov input

performance. This is because the setting to zero of the faulty sensor signal has a much bigger impact on the RMSE than for the missing steering angle before. Hence, the Markov Chain method improves the observer input very much.

In a second step, the influence of a wheel speed sensor malfunction on the observed vehicle speed shall be analysed. In Fig. 5.36 the observed vehicle speed with Markov is plotted by a solid line, the one with sensor by dashed and the reference by dashed-dotted. Where the observed vehicle velocity with replaced sensor signals tracks the reference signal quite well during signal loss, the deviation of the pure sensor performance to the reference is bigger than expected. But when considering the influenced wheel slip calculations in case of zero wheel speed $\lambda = -1$, this deviation can be explained. In addition, the falsely observed velocity has an impact on the parameter estimation as well. Here, the slip based road friction value and the effective tyre radius show different values and, thereby, the updated vehicle model within the observer lowers the accuracy.

The RMSE are shown in Fig. 5.37. The Markov value is plotted by a solid line, the one of the sensor by a dashed and the defined limit by a dashed-dotted one. It is no surprise that the sensor RMSE is much higher than the Markov one. As the Markov concept remains below the limit almost throughout the complete sensor loss time, the performance is considered to be very good and the functionality is thus proven.

5.2.5 Yaw rate sensor malfunction

The last presented scenario is a malfunction of the yaw rate sensor. In general, if the yaw rate sensor would have a malfunction, e.g. loss of power supply, it would cause the absence of all three measured signals (yaw rate, long. & lat. acceleration). But since the concept for signal replacement, up to now, is designed to replace one sensor signal failure at once, only the yaw rate signal was affected by a malfunction here.

The yaw rate sensor signal was chosen because it represents an important state for the lateral dynamics of the vehicle and is used in every implemented function that influences them. Furthermore, the function TorVec, for which the observer is optimised, needs an accurate yaw rate to compute the desired reference states for the control.

In Fig. 5.38 the performance of the Markov Chain concept for a missing yaw rate sensor is shown. Similar to the two malfunction scenarios presented previously, the reference signal is estimated as very good except when the yaw rate signal is close to zero. But as the situations, where the yaw rate is very low are not critical and do not indicate an unstable vehicle situation, small differences will not lead to fatal actuator requests from the ADAS.

The RMSE values for the Markov and sensor signal are displayed in Fig. 5.40. Here, the value of the Markov concept is up to four times lower than the pure sensor performance. Moreover, it can be seen that the influence of the deviation from the signal replacement on the RMSE, when the absolute value is very low, is very poor. Again a zoomed view is displayed in Fig. 5.39, where more details are shown. It can be seen, that the reference values are not met exactly at each step but the deviation is very low. Moreover the estimated signal state switches with a high frequency so that this is like a noisy signal
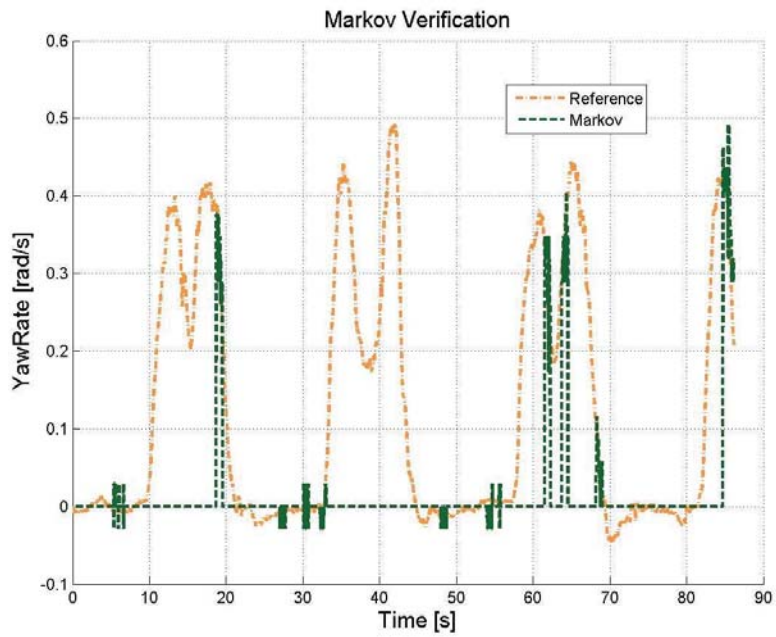
Figure 5.38: Signal replacement of yaw rate information

Figure 5.39: Zoomed view of signal replacement for missing yaw rate information
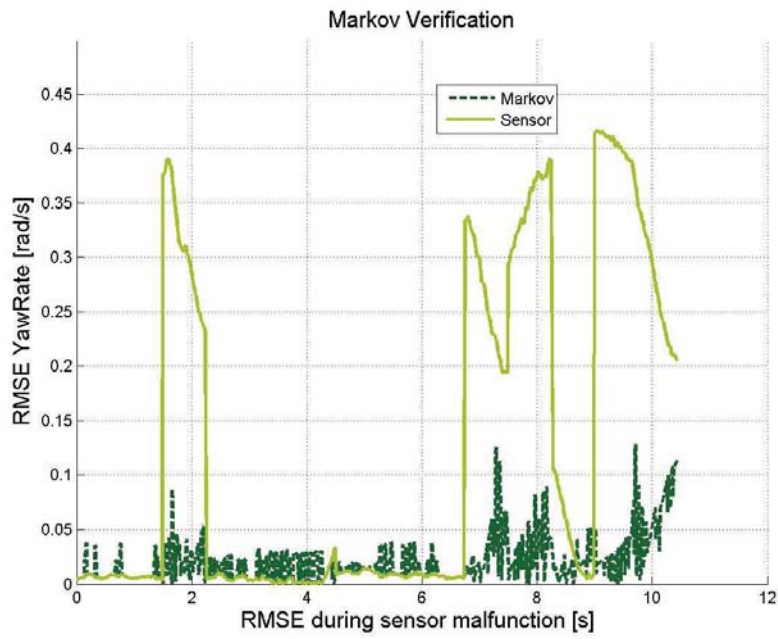
Figure 5.40: RMSE of sensor and signal replacement
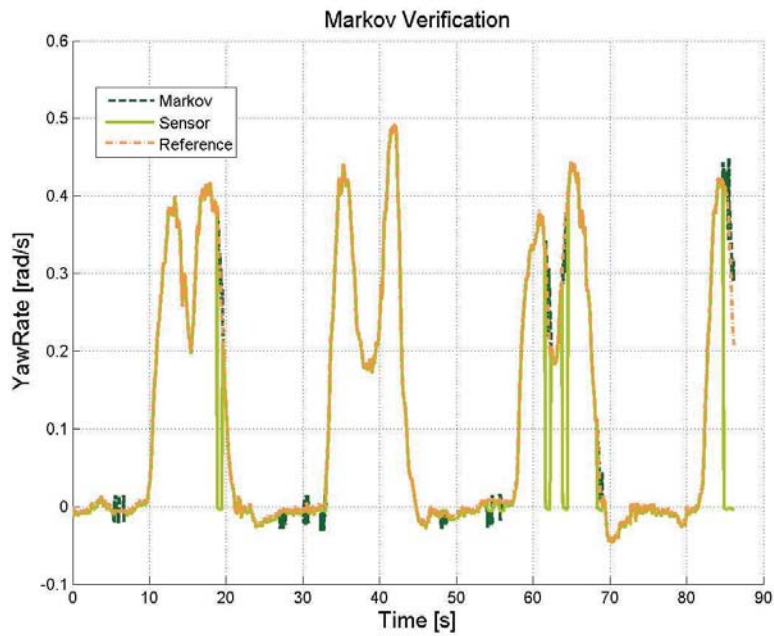
Figure 5.41: Observed yaw rate for sensor and Markov input

for the observer input.

In Fig. 5.41 the estimated yaw rate of the observer for Markov and sensor signal input is shown. As the yaw rate itself is considered important for a correct ADAS execution, the influences on the same signal are analysed. Moreover, the yaw rate has only small impacts on the lateral acceleration and the side slip angle. The results for the observer output look quite similar to the ones from the pure signal replacement. Thereby, the noise level of the Markov signal could be filtered by the observer algorithm. As a consequence, the vehicle observer algorithm is not able to compensate the signal loss of the yaw rate sensor. Thus, the presented observer is highly dependent on the yaw rate input for the output itself.
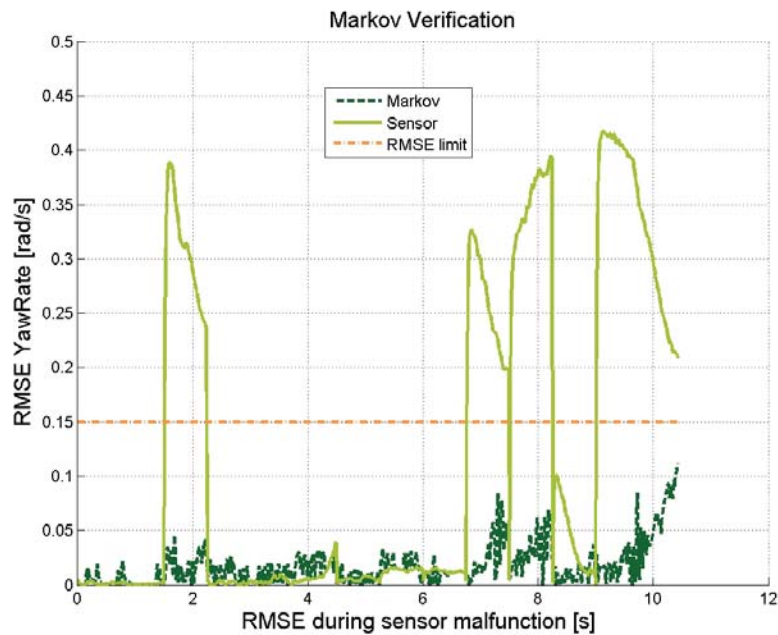
Figure 5.42: Observer RMSE with sensor and Markov input

Finally, the RMSE for the observed yaw rate with both different inputs is presented in Fig. 5.42. Where the Markov concept holds the defined limit, the sensor performance crosses these limits clearly for four times.

Therefore, the performance of the yaw rate replacement by the use of Markov Chains leads to an improved accuracy of the observed yaw rate as well.

6 Conclusion and future work

In this chapter a conclusion about the thesis and an outlook for interesting fields of further research, which arose during this work and will be solved in the future, are given.

6.1 Conclusion

The dynamics of an automotive vehicle are explained in chapter 2. The basic equations of motion are introduced and a three dimensional vehicle model is generated. This model has 14 degrees of freedom. The vehicle model can move into all three axis in space, rotate about all three axis and each wheel has 2 more degree of freedom. This model was extended with several VDC in order to validate the interaction between the designed functions and the standard integrated ones. This model was calibrated to match with the real prototype and is used for the model-based design of different vehicle functions during the eFuture project. In the end, driver models are presented which enable the automated testing with the defined driving scenarios.

An overview of filtering and estimation concepts that are applied in the automotive industry is given at the beginning of chapter 3. Here, the EKF concept turned out to be the best solution in terms of accuracy and computational load. After the structure of the Vehicle Observer was introduced a detailed explanation of the different subsystems is given. In the plausibility check the received sensor signals are handled by detection and correction mechanisms according to ISO 26262. The observation of the defined vehicle states with the EKF method by the use of non-linear vehicle model equations and a Dugoff tyre model is shown in the Extended Kalman Filter Algorithm. By applying the Lie-Derivative the observability of this concept is proven. Through implementation of variable system covariance matrices the observer became robust even in situations with high tyre slip where the model equations are not valid any more. In order to give information about varying parameters that have big influence on the vehicle dynamics, a parameter estimation is presented afterwards. In general, this estimation has event-seeking characteristics to minimise the computational load. With the feedback of these parameters to the model equations of the non-linear vehicle model, the observer has adaptive characteristics and the accuracy is improved. To prevent actuator requests that might bring the vehicle in an unstable state, an assessment of the stability limits is integrated as well. At last a computation of the driven distance of the vehicle is presented that is displayed in the instrument cluster.

The algorithm to replace delayed, missing or faulty sensor signals with the Markov Chain concept is introduced in chapter 4. After the problem of delayed or missing sensor signals is pointed out, the theory of Markov Chains, in general, is given. Here, the most

important attributes are that they are nearly memoryless, only the last state is required, and are applicable in discrete systems. When the buildup and functionality was shown, the computation of the initial distribution vector of the Markov Chains for every kind of sensor signal is described. This is followed by the design of the transition matrices which includes the probability for state changes. The computation of the final Markov Chain state is given at the end of this chapter.

In chapter 5 the necessary steps for the implementation of the algorithms into an automotive micro-controller are described. The software is implemented onto the micro-controller and tested within the prototype and by hardware in the loop tests. Various tests have been performed and three relevant tests for the Vehicle Observer are described. During slalom driving and a double lane change the performance of the Vehicle Observer is shown in high dynamic driving situations. The improved signal quality and accuracy for the vehicle states is proven by reference sensors and computation of the recursive mean-square error. Due to the lack of reference sensors for the estimated parameters, only the verification of the estimation of the road friction coefficient for different road conditions is given. Here, the estimation of a lower road friction coefficient on slightly wet road conditions compared to the performance on dry road conditions indicates the correctness of the estimation. The validation of the signal replacement was carried out by HiL tests. Three scenarios of different sensor failures, which are seen as critical, are presented additionally. By this signal replacement, the performance and, thereby, the robustness of the Vehicle Observer is enhanced even during driving scenarios with high dynamics.

6.2 Future Work

The here presented Vehicle Observer algorithm assumes some parameters as constant although they are not. The most important ones are the road inclination and the tyre stiffness since their influence on the model equations, so on the priori estimation results, is very big. For this concept the road was assumed to be ideally flat, so the inclination was set to zero. Hence, no weight distribution during hill driving or acceleration and braking is considered. A first step would be to test the robustness of the observer to ascents. If the accuracy would not hold the defined limits, an additional concept for the road inclination should be developed and implemented. The tyre stiffness, in general, depends on the vehicle speed, the road friction and the side slip angle of the vehicle. Here, the values can vary widely. An estimation concept for the tyre stiffness of each wheel would increase the precision of the tyre force calculation and the observer performance. Moreover, TorVec would benefit since the maximum applicable motor torque for each wheel could be computed depending on the current driving situation.

Another topic that should be elaborated on in the future is additional testing with the prototype. Here, tests with additional reference sensors and on icy road would enable the validation of the Vehicle Observer algorithm. With these reference sensors and a scale, the results for the estimation of the vehicle weight and the effective tyre radius which were not presented in this thesis could be validated.

The Markov Chain concept could be improved by extending the algorithm in order to deal with more than one sensor failure at a time. Here, only the computation of the initial distributions has to be modified. Moreover, the used state space for each sensor signal could be re-designed with a non-equal distribution of the states. In detail, the focus should be laid on the values around an extended normal driving zone wherein the vehicle states remain for over 97% of the time. Thus, the accuracy of the concept can be improved. Finally, a feasibility analysis could be made if this concept has the potential to replace external sensors, like radar, camera or lidar, as well.

Bibliography

[1] *Passenger cars - Stopping distance at straight line braking with ABS - Open loop test method.* ISO 21994:2007.

[2] Passenger cars - Steady-state circular driving behaviour - Open loop test methods, ISO 4138:2004.

[3] Passenger cars - Braking in a turn - Open-loop test method, ISO 7975:2006.

[4] Road vehicles - Lateral transient response test methods - Open-loop test methods, ISO 7401:2011.

[5] Passenger cars - Power-off reaction of a vehicle in a turn - Open-loop test method, ISO 9816:2006.

[6] *Passenger cars - Test track for a severe lane-change manoeuvre - Part 2:Obstacle avoidance.* ISO 3888-2:2002.

[7] J. Ackermann, A. Bartlett, D. Kaesbauer, and W. Sienel. *Robust control.* Springer, Darmstadt, 1993.

[8] H.S. Bae, J. Ryu, and J.C. Gerdes. Road grade and vehicle parameter estimation for longitudinal control using GPS. In IEEE, editor, *Conference on Intelligent Transportation Systems*, 2001.

[9] Yaakow Bar-Shalom and Xiao-Rong Li. *Estimation and Tracking, Principles, Techniques, and Software.* Artech House, 1 edition, 1993.

[10] J.F. Bellantoni and K.W. Dodge. A square root formulation of the Kalman-Schmidt filter. *AIAA Journal*, Vol. 5:1309–1314, 1976.

[11] Johan Bengtsson. *Adaptive Cruise Control and Driver Modeling.* Lund Institute of Technology, Lund, Sweden, 1 edition, 2001.

[12] M.C. Best and T.J. Gordon. Combined State and Parameter Estimation of Vehicle Handling-Dynamics. In Avec, editor, *5th Int'l Symposium on Advanced Vehicle Control*, page 6, Michigan, 2000. Avec.

[13] Marcus Boerner, Luc Andreavi, Pedro Albertos, and Rolf Isermann. Detection of lateral vehicle driving conditions based on the characteristic velocity. In *15th IFAC World Congress*, volume 35, pages 209–214, Barcelona, 2002. IFAC.

[14] Michael T. Breen. System and method for determining relative vehicle mass. In OHIO EATON CORPORATION, editor, *US Patent*, January 1996.

[15] Eli Brookner. Kalman Filter. In *Tracking and Kalman Filtering made easy*, pages 64–104. John Wiley & Sons, Inc., New York, USA, 1998.

[16] Manfred Burckhardt. *Fahrwerktechnik: Radschlupfregelsysteme*. Vogel-Verlag, Germany, 1993.

[17] Benoit Chretien, Frederic Holzmann, Sebastien Glaser, and Said Mammar. State of the art of the ADAS. In *10th International Symposium on Advanced Vehicle Control*, page 6, Loughborough, UK, 2010. AVEC.

[18] C. C. De Wit, H. Olsson, K.J. Aström, and P. Lischinsky. A new model for control of systems with friction. In *Automatic Control, IEEE Transactions*, volume 40, pages 419–425. IEEE, March 1995.

[19] dSpace. *ControlDesk nect generation - Available: https://www.dspace.com/en/inc/home/products/sw... /experimentandvisualization/controldesk.cfm.* dSpace GmbH, July 2014...

[20] H. Dugoff, P.S. Fancher, and L. Segal. Tyre performance characteristics affecting vehicle response to steering and braking control inputs. In US National Bureau of Standard, editor, *Office of Vehicle Systems Research*, 01.05.1969 1969.

[21] Mümin Tolga Emirler, Kerim Kahraman, Mutlu Sentürk, Bilin Aksun Güvenç, Levent Güvenç, and Baris Efendioglu. Vehicle Yaw Rate Estimation Using a Virtual Sensor. In *International Journal of Vehicular Technology*, volume 2013, page 13, March 2013.

[22] Garrick J. Forkenbrock. An Overview of NHTSA's ESC Research Program. In National Highway Traffic Safety Administration, editor, *Proceedings: International Technical Conference on the Enhanced Safety of Vehicles*, volume 2005, 2005.

[23] Rainer Fremd. Apparatus for measuring the mass of a motor vehicle. In Daimler-Benz Aktiengesellschaft, editor, *US Patent*, April 1987.

[24] Robert Bosch GmbH. *Steering-angle sensor - Measurement of angles from -780° to +780°*. Robert Bosch GmbH, 2000.

[25] Robert Bosch GmbH. *Yaw sensor with CAN interface - with micromechanical acceleration sensor*. Robert Bosch GmbH, 2000.

[26] Robert Bosch GmbH. *Technical Customer Documentation for DF11*. Robert Bosch GmbH, 2005.

[27] Mohinder S. Grewal and Angus P. Andrews. *Application of Kalman Filtering to GPS, INS & Navigation*. Kalman Filtering Consulting Associates, Anaheim, CA, 2000.

[28] Mohinder S.. Grewal and Angus P.. Andrews. *Kalman filtering - theory and practice using MATLAB.* Wiley-Interscience, New York, NY [u.a.], 2. ed edition, 2001.

[29] Charles Miller Grinstead and James Laurie Snell. *Introduction to probability.* American Mathematical Society, October 2012.

[30] V. Gupta, D. Spanos, and B. Hassibi. Optimal LQG control across a packet-dropping link. *System Control Letter*, 56(6):439–446, 2007.

[31] Fredrik Gustafsson. Slip-based tire-road friction estimation. In *Automatica*, volume 33, pages 1087–1099, 1997.

[32] Linn Hackenberg, Lennart Bendewald, Ina Othersen, and Sara Bongartz. Licht oder Sound? - Evaluation von diffusen Modalitäten zur Fahrerunterstützung während des teilautomatisierten Fahrens. In *Elektronik im Fahrzeug*, Baden-Baden, October 2013. Verband Deutscher Ingenieure.

[33] C. Hadjicostics and R. Touri. Feedback control utilizing packet dropping network links. *IEEE Conf. Decision Control*, 41(2):1205–1210, 2002.

[34] Dan Hu, Chang Zong, and Xiaoxiang Na. Combined Estimation of Vehicle States and Road Friction Coefficients Using Dual Kalman Filter. In AVEC, editor, *10th Int'l Symposium on Advanced Vehicle Control*, page 7, Loughborough, 2010. AVEC.

[35] ISO. ISO 26262:2011 - Road vehicles - Functional safety - Part 6 Product development at the software level. Technical report, 2011.

[36] Reza N. and Jazar. Vehicle Dynamics - Theory and Application. In *Vehicle Dynamics*. Springer US, 1 edition, 2008.

[37] S.J. Julier. The scaled unscented transformation. In *American Control Conference*, pages 4555 – 4559, Alaska, USA, 2002.

[38] S.J. Julier and J.K. Uhlmann. A New Extension of the Kalman Filter to Nonlinear Systems. In The 11th Int. Symp. on Aerospace/Defence Sensing, editor, *Proceedings of AeroSens*, 1997.

[39] S.J. Julier and J.K. Uhlmann. Reduced sigma point filters for the propagation of means and covariances through nonlinear transformations. In American Control Conference, editor, *Proceedings of the 2002*, pages 887–892, Alaska, USA, 2002.

[40] G. Kaiser, Q. Liu, C. Hoffmann, M. Korte, and H. Werner. Torque Vectoring for an Elec-tric Vehicle Using an LPV Drive Controller and a Torque and Slip Limiter. In IEEE, editor, *Conference on Decision and Control*, page 8, Hawaii, 2012. IEEE.

[41] Soummya Kar, Bruno Sinoploi, and José Moura. Kalman Filtering with Intermittent Observations - Weak Convergence to a Stationary Distribution. In *IEEE Transactions on Automatic Control*, volume 57, pages 405–420. IEEE, July 2011.

Bibliography

[42] Uwe Kiencke and Lars Nielsen. *Automotive Control Systems - For Engine, Driveline, and Vehicle.* Springer eBook Collection, Engineering [Dig. Serial], Springer-11647 [Dig. Serial]. Springer-Verlag Berlin Heidelberg, Berlin, Heidelberg, second edition edition, 2005.

[43] Sebastian Kluge, Konrad Reif, and Martin Brokate. Stochastic Stability of the Extended Kalman Filter With Intermittent Observations. In *IEEE Transactions on Automatic Control*, volume 55, pages 514–518. IEEE, January 2010.

[44] C. Letellier, L.A. Aguirre, and J. Maquet. Relation between observability and differential embeddings for nonlinear dynamics. In *Phys. Rev. E*, volume 71, pages 066–213. American Physical Society, June 2005.

[45] Meiqin Liu, Meikang Qiu, Senlin Zhang, and Zhiyun Lin. Robust H_∞ Fusion Filtering for Discrete-Time Nonlinear Delayed Systems with Missing Measurements. In ACC, editor, *American Control Conference*, page 6, Baltimore, 2010.

[46] C. Lundquist and T.B. Schoen. Road Geometry Estimation and Vehicle Tracking using a Single Track Model. In IEEE, editor, *IEEE Intelligent Vehicles Symposium*, Eindhoven, NL, 05.06.2008 2008.

[47] Charles C. Macadam. Understanding and Modeling the Human Driver. *Vehicle System Dynamics*, 40(1-3):101–134, 2003.

[48] J. Nilsson. *Real-Time Control Systems With Delays.* PhD thesis, Lund Inst. Technol., Lund, Sweden, 1998.

[49] James R. Norris. *Markov Chains.* Cambridge University Press, 1998.

[50] Henrik Olsson. Control Systems with Friction. *Department of Automatic Control, Lund Institute of Technology*, 1045:172, 1996.

[51] Hans B. Pacejka. *Tyre and Vehicle Dynamics.* Elsevier, Oxford, 2 edition, 2006.

[52] K. Plarre and F. Bullo. On Kalman Filtering for Detectable Systems with Intermittent Observations. *IEEE Trans. Automat. Control*, 54(2):386–390, 2009.

[53] R. Rajamani and J.K. Hedrick. Adaptive observers for active automotive suspensions: theory and experiment. In IEEE Transactions, editor, *Control Systems Technology*, volume 3, pages 86–93, 01.03.1995 1995.

[54] Rajesh Rajamani. *Vehicle Dynamics and Control.* Springer eBook Collection, Engineering [Dig. Serial], Springer-11647 [Dig. Serial]. Rajesh Rajamani, Boston, MA, 2006.

[55] L.R. Ray. Nonlinear State and Tire Force Estimation for Advanced Vehicle Control. *IEEE Transaction on Control Systems*, 3(1):7, 1995.

[56] P. Riekert and E. Schunck T. Zur Fahrmechanik des gummibereiften Kraftfahrzeugs. *Ingenieur-Archiv*, 11(3):pp 210–224, 01.06.1940 1940.

[57] M. R. Risch. Der Kamm'sche Kreis - Wie stark kann man beim Kurvenfahren Bremsen. In *Fahrphysik und Verkehr*. PdB-Ph., 12.07.2002 2002.

[58] Thomas Schauer. Systemidentifikation und Regelung in der Medizin. In TU Berlin, editor, *Regelungssysteme*. TU Berlin, 2006.

[59] Correvit sensor. *Available: http:// www.corrsys-datron.com / Support / Manuals / Bedienungsanleitungen / a_Sensoren / cds-m_L-400_d.pdf.* Kistler Holding AG, 04.12.2012 ...

[60] Zvi Shiller. Optimization Tools for Automated Vehicle Systems. In *Working Papers*, pages 8–9. California Partners for Advanced Transit and Highways (PATH), July 1995.

[61] D. Simon. *Optimal state estimation-kalman, H_∞ and nonlinear approaches.* Hoboken, New Jersey, USA, 1 edition, 1995.

[62] H. Sun, R. Liu, and C. Wen. Design and performance analysis of robust fusion filters for a class of continuous uncertain dynamic systems. In CCC, editor, *26th Chinese Control Conference*, page 8, Hunan, 2007. CCC.

[63] Tata. *Coventry and Birmingham Low Emission Demonstrators Coventry and Birmingham Low Emission Demonstrators (CABLED) - Vehicle Data.* Tata Motors, 2009.

[64] VDE. *Elektrofahrzeuge - Bedeutung, Stand der Technik,Handlungsbedarf.* Verlag Deutscher Ingenieure, 2010.

[65] H: Versmold and M. Saeger. Plausibility Checking of Sensor Signals for Vehicle Dynamics Control Systems. In *8th International Symposium on Advanced Vehicle Control AVEC*, volume 6. AVEC, July 2006.

[66] M. Wada, K. Yoon, and H. Hashimoto. Nonlinear filter road vehicle model development. In Intelligent Transportation Systems, editor, *Proceedings. 2001 IEEE*, pages 734–739, Oakland, CA, 2001.

[67] Carl-Gustaf Wallman and Henrik Äström. Friction measurement methods and the correlation between road friction and traffic safety - A literature review. In *VTI meddelande 911A · 2001*, 2001.

[68] Z. Wang, F. Yang, D. W. C. Ho, and X. Liu. Robust H_∞ control for networked system with random packet losses. *IEEE Trans. Syst. Man*, 37(4):916–924, 2007.

[69] J. Wheals, R. Barnbrook, R. Parkinson, M. Dean, and R. Donin. Torque Vectoring. *ATZ*, 2007(109):11 ff., 2007.

[70] J. Xoing and J. Lam. Stabilization of linear systems over networks with bounded package loss. *Automatica*, 43(1):80–87, 2007.

[71] F. Yang, Z. Wang, Y.S. Hung, and M. Gani. H_∞ control for networked systems with random communication delyas. In *IEEE Transactions on Automatic Control*, volume 51, pages 511–518. IEEE, 2006.

[72] D. Yue, E. Tian, Z. Wang, and J. Lam. Stabilization of systems with probabilistic interval input delay and its applications to networked control systems. In *IEEE Transactions on Systems, Man, and Cybernetics - Part A: Systems and Humans*, volume 39, pages 939–945. IEEE, June 2009.

List of Figures

List of Tables